UNIVERSITÀ
DEGLI STUDI
DI PADOVA

Sede Amministrativa: Università degli Studi di Padova
Dipartimento di Scienze Chimiche

SCUOLA DI DOTTORATO DI RICERCA IN SCIENZA E INGEGNERIA DEI MATERIALI
CICLO XXII

NONLINEAR OPTICAL PROCESSES IN MOLECULAR SYSTEMS AT THE INTERFACE WITH METAL NANOSTRUCTURES

Direttore della Scuola : Ch.mo Prof. Gaetano Granozzi
Supervisore : Ch.mo Prof. Renato Bozio

Dottoranda : Ida Ros

MEMENTO AUDERE SEMPER

G. D’Annunzio

ABSTRACT

L'eccitazione dei plasmoni di superficie, cioè dell'oscillazione collettiva degli elettroni di conduzione, influenza fortemente le proprietà ottiche delle nanostrutture metalliche. Inoltre, in condizioni di risonanza, si sviluppa, sulla superficie della nanostruttura, un fortissimo campo elettrico localizzato. Controllando le dimensioni e la forma delle nanostrutture, è possibile controllare la frequenza di risonanza del plasmone superficiale e, di conseguenza, la frequenza alla quale il campo elettrico locale verrà amplificato. Se una molecola è posizionata all'interfaccia con la nanostruttura metallica, le sue proprietà ottiche risentiranno del campo locale e potranno essere amplificate o ridotte dal metallo.

In questo lavoro di tesi, sono stati studiati, con diverse tecniche, gli effetti, sulle proprietà ottiche di molecole, dell'interazione con nanostrutture metalliche. In particolare, ci si è concentrati sulla sintesi e sullo studio delle proprietà non lineari di nanoshell (NSs) nude e funzionalizzate.

Sono state sintetizzate nanoparticelle di oro di forma diversa: particelle sferiche in acqua e toluene, a forma di rod in acqua (successivamente trasferite in solventi organici), core-shell in acqua. Le nanostrutture d'oro sono state funzionalizzate con spiropirani, PEP-C3-SH e PEP-C12-SH (due molecole eterocicliche), Rodamina B.

I tempi di decadimento di fluorescenza per PEP-C3-SH e PEP-C12-SH liberi e legati alle nanorods (NRs) sono stati misurati per studiare l'interazione tra il colorante e la nanostruttura e per valutare gli effetti della diversa lunghezza della catena alchilica. Il colorante, indipendentemente dalla lunghezza della catena, presenta un decadimento biesponenziale con un tempo breve di 6.2 ± 0.5 ns e uno lungo di 61 ± 2 ns. In seguito alla funzionalizzazione, l'interazione tra la molecola e le NRs provoca un cambiamento nella

dinamica di decadimento del PEP. Sia il PEP-C3 che il PEP-C12 legati alle NRs, decadono più rapidamente, indicando un'attenuazione della fluorescenza.

Le nanoshell funzionalizzate con la Rodamina B sono state caratterizzate con la tecnica Pump and Probe. Il colorante modifica la dinamica delle NSs e riduce il tempo di decadimento dell'accoppiamente elettrone-fonone da 4.9 ps (NS nude) a 3.7 ps (RhB-NSs), introducendo un canale addizionale attraverso cui gli elettroni caldi possono decadere.

Sono state effettuate delle misure SERS su benzentiolo attaccato a nanoshell, depositate su substrati di vetro. Shell incompleti caratterizzati da punte acuminate possono risultare molto interessanti per la Spettroscopia SERS per i forti campi locali che si sviluppano sulle punte. Un aumento del segnale Raman è stato chiaramente osservato, dato che la concentrazione di benzentiolo era troppo bassa per dare segnale Raman eccetto in caso di effetti di campo locale.

Sono state effettuare misure Z-scan con impulsi di durata di centinaia di femtosecondi, a frequenza di ripetizione di 20 e 200 Hz e a diverse energie, per studiare la risposta non lineare di NRs e NSs non funzionalizzate. Entrambe le nanostrutture si comportano come assorbitori saturabili e subiscono delle modifiche morfologiche per effetto dell'illuminazione con impulsi laser.

I dati z-scan per le nanoshell, fittati con il modello Sheik-Bahae, producono un valore effettivo del coefficiente di assorbimento non lineare $\beta = (-1.1 \div -9.6) \times 10^{-11}$ cmW^{-1} che dipende sia dall'energia dell'impulso che dalla frequenza di ripetizione. Il valore assoluto del coefficiente di assorbimento non lineare aumenta sia con l'energia che con la frequenza di ripetizione. L'aumento con la frequenza di ripetizione è dovuto a effetti termici, confermati anche da un aumento del raggio del beam waist usato per fittare i dati z-scan. Invece, la dipendenza dall'energia indica che il processo non è un fenomeno al terzo ordine ma si deve tenere conto di contributi di ordine superiore.

Insieme agli effetti plasmonici, le nanoshell depositate su elettrodi trasparenti, come l'ITO (Indium Tin Oxide), potrebbero potenzialmente migliorare l'efficienza sia dell'assorbimento della luce che della separazione di carica. Per questa ragione, è stata misurata la funzione lavoro di nanoshell depositate su substrati di ITO con la tecnica Kelvin probe. Scegliendo opportunamente lo spessore dello shell, se pre-funzionalizzare l'ITO e il livello di ricoprimento di particelle, è possibile variare la funzione lavoro dell'elettrodo nell'intervallo 3.9 – 4.4 eV.

ABSTRACT

Surface plasmon excitations, i.e. collective oscillations of the conduction electrons, strongly influence the optical properties of metal nanostructures. Furthermore, under resonance conditions, a giant local electromagnetic field develops on the nanostructure surface. By controlling the size and shape of the nanostructures, it is possible to control the surface plasmon resonance frequency and so the frequency at which the local field will be amplified. If a molecule is located at the interface with metal nanostructures, its optical properties will be affected by the local field and can be enhanced or suppressed by the metal.

Here, the effect on the optical properties of molecules due to the interaction with metal nanostructures is investigated by different techniques. Emphasis is placed on the synthesis and the study of the nonlinear properties of nude and functionalized gold nanoshells (NSs).

Different shape gold nanoparticles are synthesized: spherical particles in water and in toluene, rod like particles in water subsequently transferred in organic solvents, core-shells in water. Gold nanostructures have been functionalized with spiropyran, PEP-C3-SH and PEP-C12-SH (two heterocyclic dyes), Rhodamine B.

Fluorescence decay times for PEP-C3-SH and PEP-C12-SH free and bound to nanorods (NRs) have been measured to study the interaction between the dye and the nanostructure and to evaluate the effects of the chain length. The PEP moieties present a two exponential decay times: a short one of 6.2 ± 0.5 ns and a long one of 61 ± 2 ns. When the dye is bound to NRs, the interaction between the molecules and the nanoparticles

provoked a change in the PEP dynamics. Both PEP-C3 and PEP-C12 bound to NRs, decay faster, indicating quenching of fluorescence.

Nanoshells functionalized with Rhodamine B have been characterized with Pump and Probe technique. The dye clearly modified the dynamics of naked NSs and shortened the electron-phonon time decay from 4.9 ps (naked NSs) to 3.7 ps (RhB-NSs) introducing an additional channel by which hot electrons can decay.

SERS measurements of NSs, deposited on glass substrates, covered by benzenethiol were performed. Incomplete shells with sharp tips may turn out to be quite interesting for SERS analysis due to the strong local field that take place at tip apexes. Enhancement of the Raman signal has been clearly observed because the concentration of benzenethiol is too low to give Raman signal except in case of strong enhancement field effects.

Z-scan measurements, with fs laser pulses, were performed at 20 and 200 Hz and at different energy to study the nonlinear response of naked NRs and NSs. Both nanostructures behaved like saturable absorber and reshaped during laser pulse illumination. NSs z-scan data, fitted with Sheik-Bahae model, yielded an effective value of the non linear absorption coefficient $\beta = (-1.1 \div -9.6) \times 10^{-11}$ cmW^{-1} dependent on the pulse energy and repetition rate. The absolute value of the nonlinear absorption coefficient increased both with energy and pulse repetition rate. The effect of increasing the repetition rate is likely related to thermal effects, also confirmed by an increase of the beam waist radius used for fitting the z-scan data. The dependence on the energy, instead, indicated that the process is not a third order phenomenon, but higher order contributions should be taken into account.

Together with the plasmonic effects, the NSs deposition onto a transparent electrode potentially allows for improved efficiency both for light collection and charge collection. With this motivation, work function measurements on NSs deposited ITO substrates have been performed by the Kelvin probe method. They showed that by selectively choosing the shell thickness, ITO pre-functionalization and nanoparticle coverage, it is possible to fine-tune the WF of the transparent electrode within the range of 3.9 – 4.4 eV.

CONTENTS

CHAPTER 1

Introduction

1.1 Nanotechnology

Nanotechnology is one of the most popular research field of the last decades. A variety of interdisciplinary research fields working with objects of dimensions less than 100 nm are usually referred to as nanotechnology. The basic idea of the nanotechnology dates back to the 1959, when the physicist Richard Feynman presented his famous talk entitled "There's Plenty of Room at the Bottom" at the annual conference of the American Physical Society. Feynman described a process by which the ability to manipulate individual atoms and molecules might be developed, using one set of precise tools to build and operate another proportionally smaller set, and so on down to the needed scale.

However, the very birth of nanotechnology as an applied discipline is represented by the invention and development of the Scanning Probe Microscopy, with the Scanning Tunneling Microscope (STM) first in the 1981,[1] with which it is possible to observe materials down to single atoms.

Today nanotechnologies apply to several fields like photovoltaics,[2-6] biotechnologies,[7-9] sensors,[10-13] design and control of innovative nanostructured materials and many more. But the advantage of nanosystems is not only the improvement of already known technologies. Nanoscale materials have revealed peculiar new properties associated with size and spatial

organization, as for example Coulomb blockade, melting point,[14] optical properties,[15] and many more.

1.2 Metal nanostructures

Metal nanostructures possess remarkable properties compared with the corresponding bulk material.[14] These properties depend mainly on the size and shape of particles,[15] the distance between them[16] and the environment.[17] Consequently, the ability to control their properties through a careful planning of the size and shape features should be very important for device applications.[6, 18, 19]

For example, noble metal nanoparticles (NPs) have received special attention because of their optical properties. Differing from the broad structureless absorption spectra of the corresponding bulk metals, they show an absorption band in the visible and near infrared region of the electromagnetic spectrum that depends precisely on the shape, the size, the embedding medium and, obviously, on the metal making up the nanostructures.[17, 20-22]

The well defined absorption band is due to a surface plasmon resonance (SPR) and corresponds to the coherent motion of the conduction-band electrons caused by the interaction with the electromagnetic field.[21] Typically the SPR for gold and silver nanoparticles falls in the visible range between 400 and 550 nm. However, aggregates of metal nanoparticles display a very large and broad SPR that covers the whole visible region and part of the near infrared spectral range.

Spherical nanoparticles present a plasmon resonance which is not widely tunable. More tunable SPR are obtained using rod like and core-shell shaped gold particles. In the first case, as described in the following chapters, SPR red shifts increasing nanorod length.[23] Instead, nanoshells, composed of a dielectric core coated with a nanometer thick gold shell, possess an SPR which depends on the relative size of the core and the thickness of the overlayer.[24] In both these nanostructures, the SPR can be tuned in visible and near infrared spectral range by properly designing their shape and size.[20] The possibility to tune the resonance wavelength in the near infrared region (NIR), where penetration of light through biological tissues is maximal, is very appealing for applications in biomedicine, including photothermal cancer therapy,[7] immunoassays, and imaging contrast agents[25].

The ability to control the SPR position is strongly interesting because, under resonance conditions, a giant local electromagnetic field develops on the nanostructures surface. Amplification of the electric field near the particle surfaces can produce 100-10000 times greater intensity than the incident field.[22] The field extends over a spatial range on the order of 10-50 nm away from the metal surface. Controlling the size and shape of the nanostructures, it is possible to control the SPR frequency and so the frequency at which the local field will be amplified.

If a molecule is located at the interface with metal nanostructures, its optical properties will be affected by the local field and can be enhanced or suppressed by the metal. For example, Tam et al[26] reported that enhancement of the fluorescence of indocyanine green dye molecules adjacent to gold nanoshells is stronger when the plasmon resonance frequency corresponds to the emission frequency of the molecule.

Several other examples of amplified phenomena have been reported in the literature such as fluorescence,[26-30] Surface Enhanced Infrared Absorption (SEIRA),[11] second harmonic generation (SHG),[31, 32] multiphoton absorption[33, 34] and Surface Enhanced Raman Scattering (SERS).[12, 13, 35-37] In particular, two photon absorption (TPA) experiments showed that isolated nanoparticles substituted with up to more than 2000 units of a quadrupolar dye have an extremely high TPA cross section, thanks to the huge number of dyes assembled on it, but there is no enhancement of the TPA cross section per single dye.[33] For aggregates of nanoparticles substituted with TPA chromophores, instead, a strong enhancement of the TPA cross section of the single dye has been observed due to the fact that the SPR covers also the NIR region where the TPA excitation wavelength is tuned.

1.3 Thesis overview

The thesis is organized as follows.

In Chapter 2 a brief description of the theory concerning plasmon resonance in metal surfaces (both in bulk and in nanostructures) is reported. Mie theory and its extension to spheroidal and core-shell nanoparticles are introduced. Finally, some examples of the exploitation of the strong electromagnetic field developed on nanoparticles surface to enhance optical response of molecules are described.

Chapter 3 describes the different methods used to synthesize and functionalize gold nanostructures. Spherical nanoparticles are prepared in water and in toluene, nanorods are synthesized in water and subsequently transferred in toluene and nanoshells are prepared in water. Gold nanostructures are functionalized with benzenethiol, spiropyran, PEP-C3 and PEP-12. All these molecules present a terminated thiol group that binds to gold surface. Also Rhodamine B is attached to gold nanoshells through electrostatic interaction.

Morphological properties of nanorods and nanoshells are described in Chapter 4. AFM (Atomic Force Microscopy) and TEM (Transmission Electron Microscopy) are both employed to characterized nanoshells size and surface morphology.
The TEM characterization of naked and functionalized nanorods (NRs) is also performed.

Chapter 5 describes the linear optical properties of nude and functionalized gold nanostructures. We compare surface plasmon band position for different shape nanoparticles using UV-visible spectroscopy and we focus on the effect on the emission properties of molecules functionalizing nanoparticles. Time-correlated single-photon counting (TCSPC) method is used to measure the fluorescence decay time of PEP-C3-SH and PEP-C12-SH bound and unbound to nanorods.

In Chapter 6, the nonlinear optical properties of nude and functionalized gold nanostructures are described. Z-scan technique is used to characterize nonlinear absorption of nude nanorods and nanoshells. Pump and Probe method and Surface Enhanced Raman Spectroscopy (SERS) are used to study the interaction of nanoshells with Rhodamine B and benzenethiol respectively.

In Chapter 7, work function (WF) measurements of nanoshells deposited on ITO (Indium Tin Oxide) substrates are described. This section may appear a little far from the main interest in studying interaction between molecules and metallic nanostructure but it is not. Recent efforts have been concentrated on the exploitation of surface plasmon resonances of metal nanoparticles to improve photovoltaic devices due to the giant local field effect. Furthermore, metal nanostructures not only interact with molecules and polymer to enhance absorption and emission properties, but they also modify the work function of ITO glass substrate, the hole injecting electrode on common organic semiconductors device.[38-41] WF measurements on NSs have been performed with Kelvin Probe Microscopy (KPM) method. Finally, some studies on the sub-microscopic distribution of work functions and potentials, using Scanning Kelvin Probe Microscopy (SKPM) method are described.

In Chapter 8, a brief summary of the results and of their meaning is reported.

References

(1) Mironov, V. L. In *Fundamentals of Scanning Probe Microscopy;* Nizhniy Novgorod: 2004; .

(2) Stenzel, O.; Wilbrandt, S.; Stendal, A.; Beckers, U.; Voigtsberger, K.; Von Borczyskowski, C. *J. Phys. D: Appl. Phys.* **1995***, 28*, 2154-2162.

(3) Westphalen, M.; Kreibig, U.; Rostalski, J.; Lüth, H.; Meissner, D. *Sol. Energy Mater. Sol. Cells* **2000***, 61*, 97-105.

(4) Schaadt, D. M.; Feng, B.; Yu, E. T. *Appl. Phys. Lett.* **2005***, 86*, 063106.

(5) Cole, J. R.; Halas, N. J. *Appl. Phys. Lett.* **2006***, 89*, 153120.

(6) Hägglund, C.; Zäch, M.; Kasemo, B. *APPLIED PHYSICS LETTERS* **2008***, 92*, 013113.

(7) Gobin, A. M.; Lee, M. H.; Halas, N. J.; James, W. D.; Drezek, R. A.; West, J. L. *Nano Lett.* **2007***, 7*, 1929-1934.

(8) Stuart, D. A.; Haes, A. J.; Yonzon, C. R.; Hicks, E. M.; Van Duyne, R. P. *IEE Proc. - Nanobiotechnol.* **2005***, 152*, 13-32.

(9) Tom, R. T.; Suryanarayanan, V.; Reddy, P. G.; Baskaran, S.; Pradeep, T. *Langmuir* **2004***, 20*, 1909-1914.

(10) Jackson, J. B.; Halas, N. J. *PNAS* **2004***, 101*, 17930-17935.

(11) Kundu, J.; Le, F.; Nordlander, P.; Halas, N. J. *Chemical Physics Letters* **2008***, 452*, 115-119.

(12) Kneipp, K.; Kneipp, H.; Itzkan, I.; Dasari, R. R.; Feld, M. S. *Chem. Rev.* **1999***, 99*, 2957-2975.

(13) Kneipp, K.; Kneipp, H.; Kneipp, J. *Acc. Chem. Res.* **2006***, 39*, 443-450.

(14) Burda, C.; Chen, X.; Narayanan, R.; El-Sayed, M. A. *Chem. Rev.* **2005***, 105*, 1025-1102.

(15) Link, S.; El-Sayed, M. A. *Int. Revews in Physical Chemistry* **2000***, 19*, 409-453.

(16) Jain, P. K.; Huang, W.; El-Sayed, M. A. *Nano Lett.* **2007***, 7*, 2080-2088.

(17) Noguez, C. *J. Phys. Chem. C* **2007***, 111*, 3806-3819.

(18) Hutter, E.; Fendler, J. H. *Adv. Mater.* **2004***, 16*, 1685-1706.

(19) Stewart, M. E.; Anderton, C. R.; Thompson, L. B.; Maria, J.; Gray, S. K.; Rogers, J. A.; Nuzzo, R. G. *Chem. Rev.* **2008***, 108*, 494-521.

(20) Wang, H.; Brandl, D. W.; Nordlander, P.; Halas, N. J. *Acc. Chem. Res.* **2007***, 40*, 53-62.

(21) Link, S.; El-Sayed, M. A. *J. Phys. Chem. B* **1999***, 103*, 8410-8426.

(22) Kelly, K. L.; Coronado, E.; Zhao, L. L.; Schatz, G. C. *J. Phys. Chem. B* **2003***, 107*, 668-677.

(23) Jana, N. R.; Gearheart, L.; Murphy, C. J. *Adv. Mater.* **2001***, 13*, 1389-1393.

(24) Oldenburg, S. J.; Averitt, R. D.; Westcott, S.; Halas, N. J. *Chemical Physics Letters* **1998***, 288*, 243-247.

(25) Hirsch, L. R.; Gobin, A. M.; Lowery, A. R.; Tam, F. R.; Drezek, R. A.; Halas, N. J.; West, J. L. *Annals of Biomedical Engineering* **2006***, 34*, 15-22.

(26) Tam, F.; Goodrich, G. P.; Johnson, B. R.; Halas, N. J. *Nano Lett.* **2007***, 7*, 496-501.

(27) Liebermann, T.; Knoll, W. *Colloids and Surfaces A: Physicochem. Eng. Aspects* **2000***, 171*, 115-130.

(28) Ray, K.; Badugu, R.; Lakowicz, G. R. *J. Phys. Chem. C* **2007***, 111*, 7091-7097.

(29) JZhu, J.; Zhu, K.; Huang, L. *Physics Letters A* **2008***, 372*, 3283-3288.

(30) Bardhan, R.; Grady, N. K.; Cole, G. R.; Joshi, A.; Halas, N. J. *ACS Nano* **2009***, 3*, 744-752.

(31) Boyd, R. W.; Rasing, T.; Leite, J. R. R.; Shen, Y. R. *Physical Review B* **1984***, 30*, 519-526.

(32) Hayakawa, T.; Usui, Y.; Bharathi, S.; Nogami, M. *Adv. Mater.* **2004***, 16*, 1408-1412.

(33) Wenseleers, W.; Stellacci, F.; Meyer-Friedrichsen, T.; Mangel, T.; Bauer, C. A.; Pond, S. J. K.; Marder, S. R.; Perry, J. W. *J. Phys. Chem. B* **2002***, 106*, 6853-6863.

(34) Lv, J.; Jiang, L.; Li, C.; Liu, X.; Yuan, M.; Xu, J.; Zhou, W.; Song, Y.; Liu, H.; Li, Y.; Zhu, D. *Langmuir* **2008***, 24*, 8297-8302.

(35) Kneipp, K.; Kneipp, H.; Manoharan, R.; Itzkan, I.; Dasari, R. R.; Feld, M. S. *Bioimaging* **1998***, 6*, 104-110.

(36) Le Ru, E. C.; Blackie, E.; Meyer, M.; Etchegoin, P. G. *J. Phys. Chem. C* **2007***, 111*, 13794-13803.

(37) Kneipp, K. *Physics Today* **2007**, 40-46.

(38) Brown, T. M.; Cacialli, F. *J. Polymer Science: Part B* **2003***, 41*, 2649-2664.

(39) Kim, J. S.; Cacialli, F.; Friend, R. H. *Thin Solid Films* **2003***, 445*, 358-366.

(40) Hopper, H.; Sariciftci, N. S. *J. Mater. Chem.* **2006***, 16*, 45-61.

(41) O'Regan, B.; Grätzel, M. *Nature* **1991***, 353*, 737-740.

CHAPTER 2

Surface plasmon in metal nanostructures and local field enhancement

In this chapter, we describe the physical origin of the surface plasmon absorption in metallic nanostructures and of the local field enhancement developed on the nanosystem surface in resonance condition.

The surface plasmon resonance is the coherent excitation of all the free electrons within the conduction band, leading to an in-phase oscillation.[1] This phenomenon takes place when the electromagnetic field associated with the surface charge oscillations (described by Maxwell's equations) satisfies some boundary conditions that depend on the nanostructure features (material, metal-dielectric planar interface, corrugated surface, metal particles). When the exciting field is resonant with the electron oscillation frequency, a strong electromagnetic field develops near the nanostructure surface. This field can be exploited to enhance some linear and nonlinear properties of molecules adsorbed or bound to a metallic surface.

2.1 Surface plasmon modes in bulk metals

In an ideal bulk material, the surface plasmon frequency is described by a dispersion relation $\omega(k)$, which has no points of intersection with the dispersion law of the

electromagnetic radiation in air (Figure 2.1).[2] This means that the surface plasmons have a wave vector k greater than that of light at the same energy, and they cannot be excited radiatively. The coupling of electromagnetic radiation with the electron oscillations (surface plasmon-polariton) is obtained both by placing a dielectric medium with a refractive index higher than that of the air or by using roughened surface.[3] In either cases, changes in the boundary conditions for the resolution of Maxwell's equations determine the matching between the dispersion relation of the plasma frequency and the electromagnetic radiation.

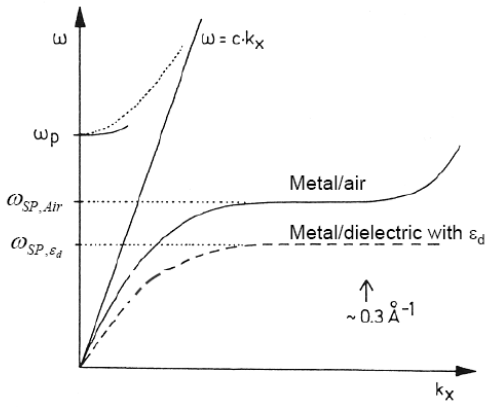

Figure 2.1: comparison between light dispersion relation and surface plasmon dispersion relation in bulk metal at the interface with air or dielectric. (Ref. 2)

For example, by covering a prism of glass with a thin metal film (Figure 2.2a), it is possible to excite surface plasmons at the metal-air interface by an evanescent electromagnetic field developed at the dielectric-metal interface. In this way, the radiation that excites the plasmon is described by a dispersion curve with a slope ω/k smaller than that of the light in air and the intersection occurs with the dispersion relation of the plasma frequency (Figure 2.2b).

However, if the metal surface is rough we can model it in the simplest way by considering a periodic modulation with reciprocal lattice vector G. The condition of coupling between light and surface plasmons is obtained when the wave vectors satisfy the relation $k_{\parallel} = k_{SP} \pm mG$. Consequently, the intersection between the dispersion curve of light and that of plasmons occurs because of the system periodicity (Figure 2.3).

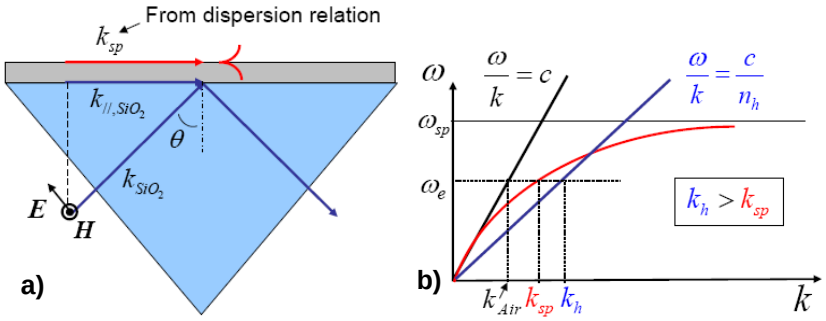

Figure 2.2: a) Kretchmann configuration to excite surface plasmon at the metal-air interface; b) comparison between the dispersion relation for surface plasmon at the metal-air interafce with the dispersion relation of light in air and at the metal-dielectric interface.

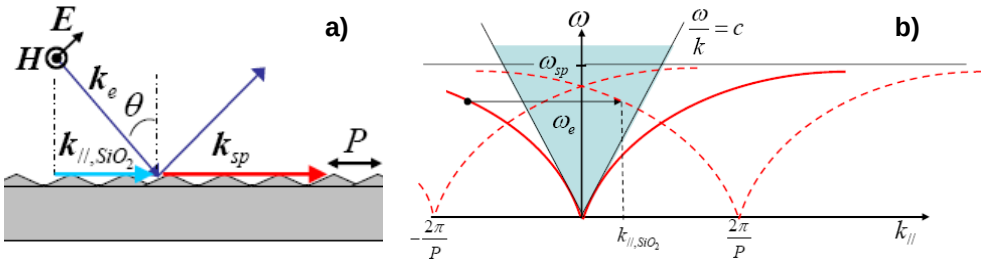

Figure 2.3: a) Surface plasmon excitation in periodic structures; b) comparison between the dispersion relation for surface plasmon in periodic structures with the dispersion relation of ligh.

2.2 Surface plasmon modes in metal nanoparticles: Mie theory

Unlike the excitation of surface plasmons in bulk metals, the boundary conditions that apply to the Maxwell's equations for nanoparticles of 5-50 nm in size allow the direct coupling with electromagnetic radiation without the need to introduce constraints in the structure of the system. Since the diameter of nanoparticles is of the order of the penetration length of the electromagnetic field, the light radiation enters in the particle. The field inside the particle moves the conduction electrons collectively with respect to the fixed positive charges of the lattice ions (Figure 2.4). The Coulomb attraction forces between electrons and nuclei generates a restoring force that causes the oscillation of the electron cloud relative to the ionic framework.[4] If the frequency of the electromagnetic field is resonant with the mode of collective oscillations, a small exciting field is enough to get a strong oscillation.

The bright color shown by metallic nanoparticles such as gold and silver, is due to excitation of the collective oscillation mode by electromagnetic radiation in the visible. The interaction between the plasmons and the visible light is much more effective than

any other organic or inorganic chromophore and has a cross section of absorption for each particle that can exceed by orders of magnitude that of the best dyes.[5]

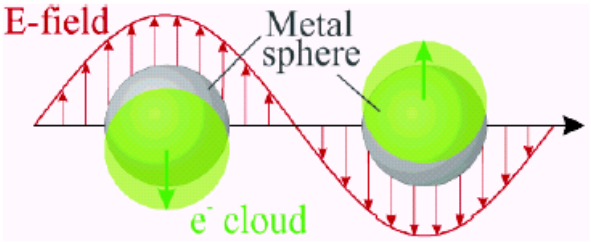

Figure 2.4: Plasmon oscillation for a sphere, showing the displacement of the conduction electron charge cloud relative to the nuclei. (ref. 4)

The first theory that explains this interaction was developed by Mie in 1908.[6] He solved exactly the Maxwell's equations for the extinction and scattering of electromagnetic radiation by a spherical particle. The solution of the electrodynamic calculation, with the use of appropriate boundary conditions, leads to a series of multipole oscillations of the extinction cross section.[1] Expanding the electromagnetic fields in spherical harmonics, we obtain the following expression for the extinction σ_{ext} and scattering σ_{sca} cross section :

$$\sigma_{ext} = \frac{2\pi}{|k^2|}\sum_{L=1}^{\infty}(2L+1)Re(a_L + b_L) \quad (2.1)$$

$$\sigma_{sca} = \frac{2\pi}{|k^2|}\sum_{L=1}^{\infty}(2L+1)(|a_L|^2 + |b_L|^2) \quad (2.2)$$

$$\sigma_{abs} = \sigma_{ext} - \sigma_{sca} \quad (2.3)$$

$$a_L = \frac{m\psi_L(mx)\psi'_L(x) - \psi'_L(mx)\psi_L(x)}{m\psi_L(mx)\eta'_L(x) - \psi'_L(mx)\eta_L(x)} \quad (2.4)$$

$$b_L = \frac{\psi_L(mx)\psi'_L(x) - m\psi'_L(mx)\psi_L(x)}{\psi_L(mx)\eta'_L(x) - m\psi'_L(mx)\eta_L(x)} \quad (2.5)$$

where $m=n/n_m$ (n complex refractive index of the particles, n_m real refractive index of the medium), k is the wave vector and $x = |k|r$ (with r particle radius); ψ_L and η_L are Ricatti-Bessel functions with L index of summation over spherical harmonics.

We introduce the dipole approximation or quasi-static regime (a condition that occurs when the particle size is much smaller than the wavelength of the incident radiation, $2r<<\lambda$) that allows to consider only the dipole term in the expansion series and simplify the problem. The Mie theory reduces to the following expression:

$$\sigma_{ext}(\omega) = 9\frac{\omega}{c}\varepsilon_m^{3/2}V\frac{\varepsilon_2(\omega)}{[\varepsilon_1(\omega)+2\varepsilon_m]^2+\varepsilon_2(\omega)^2} \quad (2.6)$$

where V is the volume of the particle, ω is the angular frequency of exciting radiation, c is the speed of light and ε_m and $\varepsilon(\omega) = \varepsilon_1(\omega) + i\varepsilon_2(\omega)$ are, respectively, the dielectric function of the medium and of the bulk metal. While the former is considered independent on frequency if the medium is not absorbing, the latter is complex and it is a function of energy. The resonance condition is satisfied when $\varepsilon(\omega) = -2\varepsilon_m$, if ε_2 is small or weakly dependent on frequency.

For particle sizes comparable to the wavelength of the incident radiation, higher-order terms (quadrupole, octupole, etc..) have to be considered in Eq. (2.1) and (2.2) because electromagnetic radiation is no longer able to polarize the nanoparticles homogeneously (dynamic regime). Higher order modes appear, in the absorption spectrum, as additional peaks at lower energies, the plasmon band shifts to the red with increasing particle size (delay effect or Extrinsic size effect).[7]

As seen in Eq. (2.6), which is valid in the quasi-static regime, the extinction coefficient does not depend on the particle size. Experimentally, however, it is observed that, for particles of radius less than 10 nm, the plasmon band broadens and weakens.[5, 8] This phenomenon, called intrinsic size effect, is explained considering that the electron mean free path (which for gold is of the order of 40-50 nm) becomes larger than the particle size. The dielectric function of the metal that appears in Eq. (2.6), can be rewritten as the contribution of an interband term $\varepsilon_{IB}(\omega)$, which takes into account the response of the d electrons, and an intraband one $\varepsilon_D(\omega)$, which takes into account only the free electrons in the conduction band $\left(\varepsilon(\omega) = \varepsilon_{IB}(\omega) + \varepsilon_D(\omega)\right)$.[5] $\varepsilon_D(\omega)$ contribution is calculated using the Drude model:

$$\varepsilon_D(\omega) = 1 - \frac{\omega_p^2}{\omega^2 + i\omega\gamma} \tag{2.7}$$

where $\omega_p^2 = ne^2/\varepsilon_0 m_{eff}$ is the volume plasma frequency which depends on the density of free electrons n and on the effective mass of the electron m_{eff}; e is the electronic charge, ε_0 the permittivity in vacuum and γ_0 is a phenomenological damping constant and it is related to the lifetimes of all the electronic processes (electron-electron scattering, electron-phonon and electron-lattice defects):

$$\gamma_0 = \sum_i \tau_i^{-1} = \tau_{e-e}^{-1} + \tau_{e-ph}^{-1} + \tau_{e-d}^{-1} \tag{2.8}$$

For particles smaller than the electron mean free path, electron scattering with the surface becomes dominant and therefore the dependence of the damping factor on the particle radius *r* is introduced:

$$\gamma(r) = \gamma_0 + \frac{Av_F}{r} \tag{2.9}$$

where γ_0 is the damping constant for the bulk material, *A* is a parameter that depends on the scattering process and v_F is the electron speed at the Fermi energy. This size effect is called "intrinsic" because the dielectric function is itself dependent on the radius *r* of the particle.

In resonance conditions, the Mie theory in the dipole approximation also predicts an increase of the electric field on the surface of the particle. Locally, the electromagnetic field is given by the sum of the incident field E_0 and of the polarization induced by the surface plasmons excitation. For spherical particles, the local field inside the cluster is:[9]

$$E = -2\left(\frac{\varepsilon_m - \varepsilon}{\varepsilon + 2\varepsilon_m}\right) E_0 \tag{2.10}$$

The electric field on the surface of the sphere is:[3]

$$E_{loc} = E_0 - 2\left(\frac{\varepsilon_m - \varepsilon}{\varepsilon + 2\varepsilon_m}\right) E_0 = \frac{3\varepsilon}{\varepsilon + 2\varepsilon_m} E_0 \tag{2.11}$$

where the local field factor $3\varepsilon/(\varepsilon + 2\varepsilon_m)$ becomes very large in resonance condition.
Mie theory allows to treat problems with spherical symmetry and it can be extended to core-shell systems and spheroidal particles (Gans theory), but it presents some limits for asymmetrical shape clusters or interacting nanoparticles.

2.2.1 Extension to spherical core shell particles

For structures made of *r* several concentric layers, the problem of scattering and absorption of radiation can be treated in the same way as for compact spheres. In this case, however, the boundary conditions are formulated to take into account that the fields inside the sphere suffer any discontinuity of refractive index between each layer.
We consider a spherical particle composed of *r* different layers (Figure 2.5), the expression for the extinction cross section is identical to Eq. (2.1).

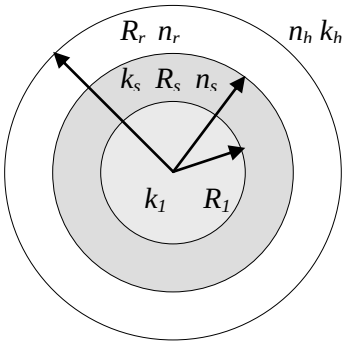

Figure 2.5: Example of a multilayer structure for a spherical particle.

The expansion coefficients a_L and b_L are different because they arise from different boundary conditions:

$$a_L = \frac{m_r\psi_L(m_r x_r)[\psi'_L(x_r)+T_L^r\chi'_L(x_r)]-\psi'_L(m_r x_r)[\psi_L(x_r)+T_L^r\chi_L(x_r)]}{m_r\eta_L(m_r x_r)[\psi'_L(x_r)+T_L^r\chi'_L(x_r)]-\eta'_L(m_r x_r)[\psi_L(x_r)+T_L^r\chi_L(x_r)]} \tag{2.12}$$

$$b_L = \frac{\psi_L(m_r x_r)[\psi'_L(x_r)+S_L^r\chi'_L(x_r)]-m_r\psi'_L(m_r x_r)[\psi_L(x_r)+S_L^r\chi_L(x_r)]}{\eta_L(m_r x_r)[\psi'_L(x_r)+S_L^r\chi'_L(x_r)]-m_r\eta'_L(m_r x_r)[\psi_L(x_r)+S_L^r\chi_L(x_r)]} \tag{2.13}$$

where

$$T_L^s = -\frac{m_s\psi_L(m_s x_s)[\psi'_L(x_s)+T_L^{s-1}\chi'_L(x_s)]-\psi'_L(m_s x_s)[\psi_L(x_s)+T_L^{s-1}\chi_L(x_s)]}{m_s\chi_L(m_s x_s)[\psi'_L(x_s)+T_L^{s-1}\chi'_L(x_s)]-\chi'_L(m_s x_s)[\psi_L(x_s)+T_L^{s-1}\chi_L(x_s)]} \tag{2.14a}$$

$$T_L^1 = -\frac{m_1\psi_L(m_1 x_1)\psi'_L(x_1)-\psi'_L(m_1 x_1)\psi_L(x_1)}{m_1\chi_L(m_1 x_1)\psi'_L(x_1)-\chi'_L(m_1 x_1)\psi_L(x_1)} \tag{2.14b}$$

$$S_L^s = -\frac{\psi_L(m_s x_s)[\psi'_L(x_s)+S_L^{s-1}\chi'_L(x_s)]-m_s\psi'_L(m_s x_s)[\psi_L(x_s)+S_L^{s-1}\chi_L(x_s)]}{\chi_L(m_s x_s)[\psi'_L(x_s)+S_L^{s-1}\chi'_L(x_s)]-m_s\chi'_L(m_s x_s)[\psi_L(x_s)+S_L^{s-1}\chi_L(x_s)]} \tag{2.15a}$$

$$S_L^1 = -\frac{\psi_L(m_1 x_1)\psi'_L(x_1)-m_1\psi'_L(m_1 x_1)\psi_L(x_1)}{\chi_L(m_1 x_1)\psi'_L(x_1)-m_1\chi'_L(m_1 x_1)\psi_L(x_1)} \tag{2.15b}$$

$$m_s = \frac{n_{s+1}}{n_s} \tag{2.16a}$$

$$x_s = \left|\bar{k}_s\right| R_s \tag{2.16b}$$

The superscript and subscript s indicate the s-th layer, R_s is the distance between the center of the sphere and the outer s-th layer, n_s complex refractive index. In the coefficients a_L and b_L, the $\chi(x)$ is a Riccati-Bessel spherical function.

In the dipole approximation and for a core-shell structure consisting of only two layers, the equation simplifies:

$$\sigma_{ext} = 4\pi\frac{\omega}{c}\varepsilon_m^{1/2} Im(\alpha) \tag{2.17}$$

$$\alpha(\omega) = \frac{4\pi}{3}(R+d)^3\varepsilon_0\frac{(\varepsilon_s-\varepsilon_m)(\varepsilon+2\varepsilon_m)+\left(\frac{R}{R+d}\right)^3(\varepsilon-\varepsilon_s)(\varepsilon_m+2\varepsilon_s)}{(\varepsilon_s+2\varepsilon_m)(\varepsilon+2\varepsilon_s)+\left(\frac{R}{R+d}\right)^3(\varepsilon-\varepsilon_s)(2\varepsilon_s-\varepsilon_m)} \tag{2.18}$$

where R is the core radius, d the shell thickness, ε, ε_s e ε_m the dielectric constant of core, shell and matrix. If the shell is very thick, from these equations, we get the same results as compact homogeneous sphere. Otherwise, for thin shell, the absorption spectrum varies significantly according to the thickness and it contains the contribution of both materials.

Recently, core shell structures consisting of a dielectric medium (for example silica) coated with a thin metal film have arisen a great interest. These nanoparticles have a plasmon resonance that varies considerably by varying the thickness of the core and shell. For example, increasing the ratio between the silica core radius and the gold shell from 3 to 12, a plasmon resonance shift of 300 nm is obtained.[10] Clearly, the ability to move the plasmon resonance anywhere across the visible or infrared regions of the spectrum, simply by adjusting the relative size of the dielectric core and the thickness of the gold overlayer, is very interesting in developing new plasmon devices.[11]

A second model to describe plasmon absorption in metal core shell is the *Plasmon Hybridization Model*.[12] The geometry-dependent nanoshell plasmon resonances result from the interaction between the essentially fixed frequency plasmon response of a sphere and that of a cavity (Figure 2.6).

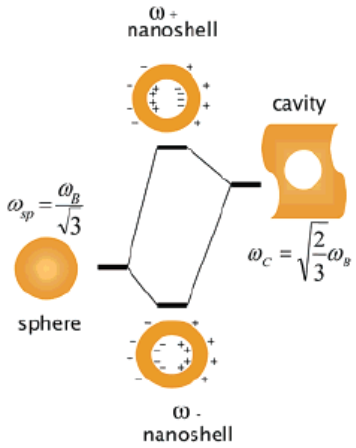

Figure 2.6: Energy level diagrams depicting plasmon hybridization in metal nanoshells.[12]

The sphere and cavity plasmons are electromagnetic excitations at the outer and inner interfaces of the metal shell, respectively. Because of the finite thickness of the shell layer, the sphere and cavity plasmons interact with each other and hybridize in a way analogous to the hybridization between atomic orbitals. This interaction results in the splitting of the plasmon resonances into two new resonances, the lower energy symmetric or “bonding”

plasmon (ω_-) and the higher energy antisymmetric or "antibonding" plasmon (ω_+). The strength of the interaction between the sphere and cavity plasmons is controlled by the thickness of the metal shell layer.

For simplicity, we assume that the conduction electrons form a uniform electron gas of density n_0 with a bulk plasmon frequency $\omega_B = (4\pi e^2 n_0/m_e)^{1/2}$. The cavity plasmon frequency can be expressed as $\omega_{C,l} = \omega_B((l+1)/(2l+1))^{1/2}$ and the sphere plasmon has a vibration frequency $\omega_{S,l} = \omega_B(l/(2l+1))^{1/2}$, where l refers to the multipolar symmetry of the plasmon mode. In a nanoshell, the deformation fields associated with the cavity and sphere plasmons introduce surface charges at both the inner and outer boundaries of the shell. These surface charges couple the sphere and cavity modes, resulting in hybridized plasmons. The hybridization of the cavity and the sphere plasmons depends on the difference in their energies $\omega_{C,l}$ and $\omega_{S,l}$ and on their interaction, which is determined by the thickness of the shell.

To describe the geometry of a nanoshell, we adopt the notation (*a*,*b*) to indicate the inner radius *a* and the outer radius *b* of the shell. The hybridization between the cavity and sphere plasmons gives rise to two hybridized plasmon modes ω_+ and ω_- for each $l > 0$. For a vacuum core, the frequencies of these modes are

$$\omega_{l\pm}{}^2 = \frac{\omega_B^2}{2}\left\{1 \pm \frac{1}{2l+1}\left[1 + 4l(l+1)\left(\frac{a}{b}\right)^{2l+1}\right]^{1/2}\right\} \tag{2.19}$$

The ω_+ mode corresponds to antisymmetric coupling between the sphere and cavity modes, and the ω_- mode corresponds to symmetric coupling between the two modes. The lower energy ω_- plasmon interacts strongly with the incident optical field, while the ω_+ mode interacts weakly and, in the case of Au, is further damped by interband transitions at energies above the d-band to Fermi energy optical transitions at approximately 2.3 eV.

2.2.2 Extension to spheroidal particles: Gans model

When the particle is elongated along one axis, the plasmon resonance absorption band splits into two, the transverse mode and the longitudinal one. The transverse mode, at higher energy, is due to oscillation of the electrons perpendicular to the elongation axis (transverse oscillation), while the longitudinal one, at lower energy, is due to oscillation along that axis. Increasing the ratio between the lengths of the major axis and minor axis (aspect ratio), the longitudinal plasmon band red shifts.

The Gans model[1] describes the plasmon absorption of these nanoparticles. For a set of spheroidal particles with *aspect ratio R*, randomly oriented in space, the cross section of extinction, in the dipole approximation, is given by:

$$\sigma_{ext} = \frac{\omega}{3c} V \varepsilon_m^{3/2} \sum_j \frac{\frac{1}{P_j^2}\varepsilon_2}{\left(\varepsilon_1 + \frac{1-P_j}{P_j}\varepsilon_m\right)^2 + \varepsilon_2^2} \tag{2.20}$$

where P_j are the depolarization factors along the three axes *A*, *B*, *C* of the spheroid with *A*>*B*=*C* defined as:

$$P_A = \frac{1-e^2}{e^2}\left[\frac{1}{2e} ln\left(\frac{1+e}{1-e} - 1\right)\right] \tag{2.21}$$

$$P_B = P_C = \frac{1-P_A}{2} \tag{2.22}$$

The *aspect ratio* appears in the depolarization factors through the dependence on *e*:

$$e = \left[1 - \left(\frac{B}{A}\right)^2\right]^{1/2} \tag{2.23}$$

As for spherical particles, the resonance condition is satisfied when the denominator of each term in the summation in Eq. (2.20) is zero, so in the absorption spectrum several peaks are present, consistent with the symmetry of the nanostructures. Each plasmon is excited only if the direction of polarization of the radiation is favorable.

As mentioned above, the position of the absorption peak of the longitudinal plasmon band shifts to longer wavelengths with increasing *aspect ratio*. This dependence is linear and follows the trend:[5]

$$\lambda_{max} = (C \cdot R - C')\varepsilon_m + C'' \tag{2.24}$$

where C, C' and C'' are experimental parameters, ε_m is the medium dielectric constant and *R* is the aspect ratio.

2.3 Plasmon mode in metal nanoparticles of complex shape: DDA – Discrete Dipole Approximation

We said that Mie theory should be applied only with spheroidal nanoparticles. For particles with a more complex shape, it is not possible to solve analytically Maxwell's or Laplace equation and it is, therefore, necessary to introduce numerical methods such as the Discrete Dipole Approximation (DDA).

The DDA is a numerical method in which the objects of interest are represented as a lattice of N points, each of which is associated with a certain polarizability.[4] The

polarization $\mathbf{P}_i$ induced in each element is the result of interaction with the local electric field E_{loc}:[13]

$$P_i = \alpha_i \cdot E_{loc}(r_i) \tag{2.25}$$

which is the sum of the incident electromagnetic field and the contribution of all other dipoles of neighboring points. The response of the particle to the electromagnetic radiation is obtained from self-consistent solution of coupled equations as Eq. (2.25). Generally, theoretical calculations reproduce the experimental results within an error of 10%, regardless of shape, size and composition of the particle.

2.4 Interaction between nanoparticles: Maxwell-Garnett model

The second limit of the Mie theory is to describe systems in which particles are very dilute, so that we can neglect the mutual interaction. However, if the distance between the particles is smaller than their size, the electric field generated on the particle is affected by other neighbor particles. In this case, the plasmon resonance shifts to red wavelengths and often a new band appears at longer wavelengths.

The Maxwell-Garnett theory, an effective medium model, explains this phenomenon. This model describes a composite metal-dielectric and it corrects the dielectric constant of the matrix considering concentration, shape and dielectric constant of nanoparticles inside it.

The complex effective dielectric constant ε_c one gets is:[1, 14]

$$\frac{\varepsilon_c - \varepsilon_m}{\varepsilon_c + k\varepsilon_m} = f_m \frac{\varepsilon - \varepsilon_m}{\varepsilon + k\varepsilon_m} \tag{2.26}$$

where f_m is the volume fraction of nanoparticles, k is a screen parameter depending on the particle shape, ε_m is the dielectric constant of the matrix, and ε is the complex dielectric constant of the metal. If f_m is less than 10%, as in normal colloidal solutions, the effects of concentration are negligible and the effective dielectric constant is equal to that of the matrix.

2.5 Electronic dynamics in nanoparticles

The transient optical response of electrons in a spherical nanoparticle, after excitation with femtosecond laser pulses, can be measured with the pump-probe technique.[5] Using these pulses (which are shorter than the relaxation times for electron-phonon energy transfer), it is possible to excite the electrons of the metal and monitor, in real time, the coupling

between electrons and phonons.[1] The excitation causes an instantaneous change in the distribution of the conduction electrons of the metal (figure 2.7-b).

The non-thermal distribution is rapidly relaxed by scattering between electrons (on 500fs time scale), giving rise to a new equilibrium distribution around the Fermi level at a higher temperature, that of "hot" electrons (figure 2.7-c). During the thermalization process, electrons lose energy and interact with the lattice through electron-phonon scattering, which occurs in few picoseconds. Once the lattice is heated, a further dissipation of energy involves the solvent in a time frame of the order of hundreds picoseconds.

The redistribution of electrons changes the dielectric function of the metal. Since the intensity and location of the plasmon band depend on the dielectric constant, the change of absorption in the region of the plasmon band reflects the dynamics of balance and cooling of electrons. Consistent with the TTM (Two Temperature Model), the electrons and the lattice can be treated as two coupled systems because the electronic heat capacity is two orders of magnitude smaller than that of the lattice.

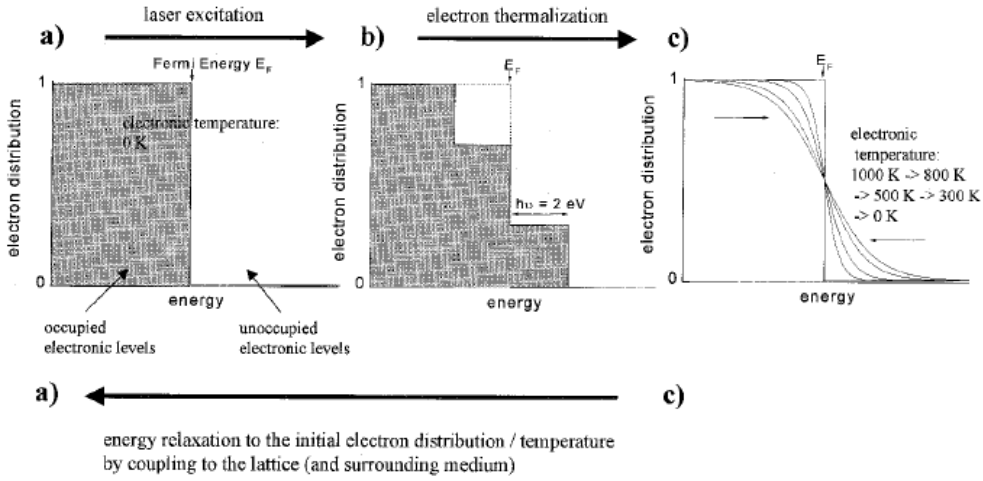

Figure 2.7: Schematic illustration of the distribution of electrons in the conduction band of metal particles. a) Before laser excitation, all states below the Fermi level are occupied. b) The laser excitation promotes some electrons above the Fermi level. This electronic distribution is not in thermal equilibrium and does not respect the Fermi-Dirac statistic. The distribution reaches thermal equilibrium after relaxation through electron-electron scattering. c) Electrons gas cools after electron-phonon coupling and phonon-phonon interaction with the medium. The system returns to the starting temperature.[1]

The absorption spectrum presents bleaching of the plasmon band (Figure 2.8). By monitoring the decay at the wavelength of the maximum of the bleaching (typically for

gold nanoparticles at around 520 nm), a biexponential trend is observed whose time components are assigned to the electron-phonon relaxation (the shorter one) and phonon-phonon relaxation with the solvent (the longer one).

To measure the electron-electron relaxation time it is necessary to use low-power pump. In fact, the processes of electron-electron scattering and electron-phonon interaction do not occur in sequence (as modeled), but overlap and therefore, electron-phonon scattering starts before the electron distribution reaches the full thermalization. Relaxation times of electron-phonon and phonon-phonon, respectively 3.1 ps e 90 ps,[5] 2.5 ps e > 50 ps,[1] 750 fs e 1 ns[15] (in this case clusters behave like molecule) are reported in the literature for different size gold nanoparticles naked or covered with thiols. Studies on nanoparticles of silver and copper reported relaxation times similar to these.[16]

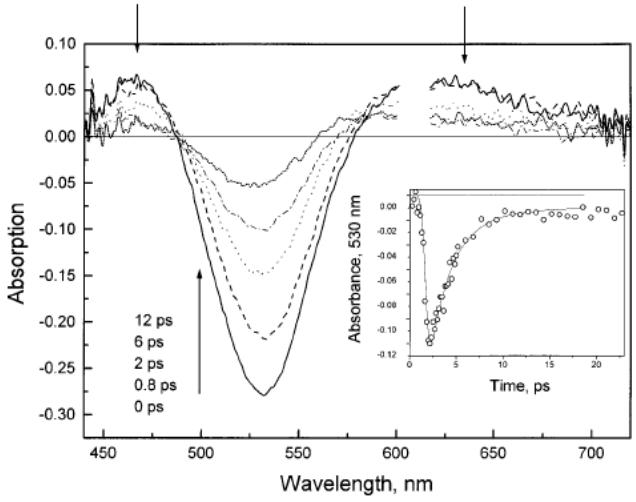

Figure 2.8: Example of transient absorption spectrum of gold nanoparticles measured at delay times of 0, 0.8, 2.0, 6.0, and 12 ps after excitation with a laser pulse of 350 fs at 600 nm. In inset we show the decay at 530 nm. It also reports the fit with lifetimes of 2.5 and > 50 ps.[17]

The electron-phonon relaxation time, for gold, is independent of the size and shape of nanoparticles[1, 16, 17] and this excludes the electron-surface scattering as the main route of dissipation of energy. The electron-phonon relaxation time depends on the intensity of the pump beam. In fact, at high pump energies, electrons gas reaches a higher temperature and so the electron-phonon relaxation process occurs in longer time.[5] The electron-phonon relaxation time depends also on the lattice crystallinity.[18] In polycrystalline nanostructures, inelastic scattering of electrons with defects reduces relaxation time. The hot electrons

collide with grain boundaries several times before they transfer the energy to the lattice through electron-phonon interaction.

In measuring transient absorption spectra, the intensity of the femtosecond laser beam is generally less than 100 nJ (fluence with the order of 1 mJ cm^{-2}) and causes an increase in the lattice temperature of a few tens of degrees. But if the beam intensity is of microjoule, the lattice temperature can reach the melting point and causes changes in nanoparticles size and shape. For example, gold nanorods may change in spherical shape after laser excitation. This transition is easily studied with optical absorption because the longitudinal plasmon band gradually disappears.[1, 5]

2.6 Enhancement of optical properties of molecules at the interface with metal nanostructures

Composite systems based on metal nanoparticles offer possibilities for enhancement of optical responses. As discussed in paragraph 2.2, in resonance condition a strong electromagnetic field is developed on the nanoparticle surface. This giant local field can be exploited to enhance optical responses of molecules in the vicinity of metal surface.

Several examples of enhancement of optical phenomena are reported in literature, here a small roundup is presented. In general, at the basis of the enhancement phenomenon, there is the amplification of the incoming and outgoing field due to the presence of the metal nanostructures. For this reason, specific condition of coupling between the plasmon resonance and the optical response of molecules should be taken into account. Efficiency can be controlled by molecule nanoparticle separation, nanoparticle size, and geometry. The geometry and size of the nanoparticle determine the properties of the localized surface plasmons it supports.

Two of the most common application in which local field enhancement is applied, are Raman and fluorescence spectroscopy. In both cases, metal nanostructures allow one to achieve approximately single molecule detection.

In Surface Enhancement Raman Spectroscopy (SERS), as better explained in Chap. 6, two effects contribute to enhance the Raman signal: the chemical and the electromagnetic effects. The former is due to specific interaction between the molecule and the metal and allows to reach not more than factors of 10-100. The latter is due to the enhancement of the laser and Stokes fields and should reach factors up to 10^8.[19]

In Fluorescence Spectroscopy, metal nanoparticles can influence the fluorescent emission of nearby molecules in several ways: by enhancing the optical intensity incident on the molecule through near field enhancement, by modifying the radiative decay rate of the molecule, and by increasing the coupling efficiency of the fluorescence emission to the far field through nanoparticle scattering. While fluorescence from a molecule directly adsorbed onto the surface of a metallic nanoparticle is strongly quenched,[20, 21] at a distance of a few nanometers from the nanoparticles, its fluorescence can be strongly enhanced.[22-24] Recently, Tam et al[25] have shown that fluorescence enhancement of indocyanine green, a low quantum yield molecular fluorophore, is strongly influenced by the plasmon resonance energy of the nanoshell and its scattering efficiency. Fluorescence enhancement is optimized by increasing particle scattering efficiency while tuning the plasmon resonance to the emission wavelength of the fluorophore.

Also molecular nonlinear optical response should be enhanced in proximity of metal nanostructures. For example, Wenseleers et al[26] have observed strong enhancement of the two-photon absorption of chromophoric polymer and thiol-bound chromophores when they are deposited on silver nanoparticle fractal clusters. Measurements on cluster films coated give spatially-averaged enhancements of 1000 for the polymer and 20000 for the molecule. They also demonstrated, using two-photon fluorescence microscopy, that the enhancement factor is spatially inhomogeneous, confirming the strong localization of collective plasmon modes in fractal metal clusters. Peak-enhancement factors of 10000 and 160000 were observed for the polymer/cluster and the thiol chromophore/cluster systems, respectively.

In all these examples, an increased planning and understanding of the plasmonic properties of nanostructures should make possible to design nanoparticle-molecule complexes that optimally enhance the optical properties of any given molecule.

References

(1) Link, S.; El-Sayed, M. A. *Int. Revews in Physical Chemistry* **2000**, *19*, 409-453.

(2) Sönnichsen, C. Plasmons in metal nanostructures, Muenchen University, 2001.

(3) Raether, H. In *Surface Plasmons on Smooth and Rough Surfaces and on Gratings;* Springer-Verlag: 1986; .

(4) Kelly, K. L.; Coronado, E.; Zhao, L. L.; Schatz, G. C. *J. Phys. Chem. B* **2003**, *107*, 668-677.

(5) Link, S.; El-Sayed, M. A. *J. Phys. Chem. B* **1999**, *103*, 8410-8426.

(6) Mie, M. *Ann. Phys.* **1908**, *330*, 377-445.

(7) Evanoff, D. D.; Chumanov, G. *J. Phys. Chem. B* **2004**, *108*, 13957-13962.

(8) Berciaud, S.; Cognet, L.; Tamarat, P.; Lounis, B. *Nano Lett.* **2005**, *5*, 515-518.

(9) Lawandy, N. M. *Appl. Phys. Lett.* **2004**, *85*, 5040-5042.

(10) Oldenburg, S. J.; Averitt, R. D.; Westcott, S.; Halas, N. J. *Chemical Physics Letters* **1998**, *288*, 243-247.

(11) Hirsch, L. R.; Gobin, A. M.; Lowery, A. R.; Tam, F. R.; Drezek, R. A.; Halas, N. J.; West, J. L. *Annals of Biomedical Engineering* **2006**, *34*, 15-22.

(12) Wang, H.; Brandl, D. W.; Nordlander, P.; Halas, N. J. *Acc. Chem. Res.* **2007**, *40*, 53-62.

(13) Miller, M. M.; Lazarides, A. A. *J. Phys. Chem. B* **2005**, *109*, 21556-21565.

(14) Palpant, B.; Prével, B.; Lermé, J.; Cottancin, E.; Pellarin, M.; Treilleux, M.; Perez, A. *Physical Review B* **1998**, *57*, 1963-1970.

(15) Link, S.; El-Sayed, M. A.; Schaaff, T. G.; Whetten, R. L. *Chemical Physics Letters* **2002**, *356*, 240-246.

(16) Hodak, J. H.; Martini, I.; Hartland, G. V. *J. Phys. Chem. B* **1998**, *102*, 6958-6967.

(17) Logunov, S. L.; Ahmadi, T. S.; El-Sayed, M. A.; Khoury, J. T.; Whetten, R. L. *J. Phys. Chem. B* **1997**, *101*, 3713-3719.

(18) Huang, W.; Qian, W.; El-Sayed, M. A.; Ding, Y.; Lin Wang, Z. *J. Phys. Chem. C* **2007**, *111*, 10751-10757.

(19) Kneipp, K.; Kneipp, H.; Manoharan, R.; Itzkan, I.; Dasari, R. R.; Feld, M. S. *Bioimaging* **1998**, *6*, 104-110.

(20) Jebb, M.; Sudeep, P. K.; Pramod, P.; Thomas, K. G.; Kamat, P. V. *J. Phys. Chem. B* **2007**, *111*, 6839-6844.

(21) Dulkeith, E.; Ringler, M.; Klar, T. A.; Feldmann, J.; Javier, A. M.; Parak, W. J. *Nano Lett.* **2005**, *5*, 585-589.

(22) JZhu, J.; Zhu, K.; Huang, L. *Physics Letters A* **2008**, *372*, 3283-3288.

(23) Li, C.; Liu, X.; Yuan, M.; Li, J.; Guo, Y.; Xu, J.; Zhu, M.; Lv, J.; Liu, H.; Li, Y. *Langmuir* **2007**, *23*, 6754-6760.

(24) Liebermann, T.; Knoll, W. *Colloids and Surfaces A: Physicochem. Eng. Aspects* **2000**, *171*, 115-130.

(25) Tam, F.; Goodrich, G. P.; Johnson, B. R.; Halas, N. J. *Nano Lett.* **2007**, *7*, 496-501.

(26) Wenseleers, W.; Stellacci, F.; Meyer-Friedrichsen, T.; Mangel, T.; Bauer, C. A.; Pond, S. J. K.; Marder, S. R.; Perry, J. W. *J. Phys. Chem. B* **2002**, *106*, 6853-6863.

CHAPTER 3

Synthesis and functionalization of gold nanostructures

In this chapter, we describe the different methods used to synthesize and functionalize gold nanostructures. The interest is mainly directed to the preparation of nanoparticles with a tunable plasmon band in the visible and near infrared regions, such as nanorods (NRs) and nanoshells (NSs), capable to enhance linear and nonlinear optical properties of molecules through the strong electromagnetic field developed on the particle surface, in resonance conditions.

Although gold spherical nanoparticles (NPs) present a plasmon resonance which is not widely tunable, we decided to start with their synthesis in order to use them as a model for the functionalization. Gold NPs synthesis, both in water[1] and in organic solvents[2], is well know and quite simple. This allowed us to start quickly with their functionalization and, at the same time, to study the more complicated synthesis of NRs and NSs at the same time.

We functionalized gold nanostructures with various molecules, differing for their linear and nonlinear optical properties.

3.1. Nanostructures

We synthesized the following gold nanostructures: nanoparticles in water and toluene, nanorods, nanoshells.

All reagents were used as purchased without further purification: tetraethyl orthosilicate (TEOS), tetrakis(hydroxymethyl)phosphonium chloride (THPC, 80% solution in H_2O), hydrogen tetrachloroaurate-(III) hydrate ($HAuCl_4$), sodium citrate ($Na_3C_6H_5O_7 \cdot 2H_2O$), potassium carbonate, sodium borohydride, dodecanethiol, cetyltrimethylammonium bromide (CTAB), silver nitrate ($AgNO_3$) were from Sigma-Aldrich; polyvinylpyrrolidone (PVP, MW 40000), 3-aminopropyltrimethoxysilane (APTMS), tetraoctylammonium bromide (TOAB), ammonium hydroxide and formaldehyde were from Fluka; sodium hydroxide was from Carlo Erba. Similarly, all solvents were used as received: toluene (Aldrich) and absolute ethanol (J.T. Baker); deionized water (18 MΩ) was provided by a Milli-Q system.

3.1.1. Growth and stabilization mechanisms

Nanostructures can be synthesized with various methods which can be grouped into two categories: thermodynamic equilibrium approach and kinetic approach.[3] In the thermodynamic approach, the synthesis consists in nucleation of small nanoparticles and subsequent growth. In the kinetic approach, formation of nanoparticles is achieved by either limiting the amount of precursor available for the growth or confining the process in a limited space such as in micelle synthesis. We are not interested in discussing in details the kinetic approach that is described in the literature.[3]

Colloidal chemistry belongs to the thermodynamic approach. In this case, the mechanism of nuclei formation in dilute solutions is usually described according to the nucleation theory of fluctuation. This requires the formation of a supersaturated solutions of metallic gold atoms, some of which coalesce into a nucleus when the statistical fluctuation of their concentration reaches values sufficiently large to allow the formation of a stable particle.

Assuming that the laws of thermodynamics are still valid for systems whose dimensions are subnanometric, then the theory of nucleation predicts that early nuclei can form only when the change in Gibbs free energy is less than zero. The expression of the change in Gibbs free energy contains two terms, one negative proportional to the cluster volume (or

the number of atoms that compose it) and a positive one resulting from the energy spent for the formation of solid-solvent interface:

$$\Delta G_N(R) = \Delta G_V(R) + \Delta G_S(R) \tag{3.1}$$

The surface term is proportional to the energy of solid-liquid interface γ_{SL} and the square of the radius of the cluster:

$$\Delta G_S(R) \propto 4\pi R^2 \gamma_{SL}$$

The volume contribution, however, is proportional to the cube of the radius and the difference in chemical potential between the liquid phase and solid phase:

$$\Delta G_V(R) \propto -\frac{4}{3}\pi R^3 k_B T ln\left(\frac{C}{C_0}\right)$$

where C is the concentration of species in solution before the nucleation, C_0 is the equilibrium concentration and the ratio C/C_0 is known as supersaturation and is the driving force for nucleation. For $C/C_0=1$, the volume contribution to the change in Gibbs free energy vanishes, the driving force for nucleation fails and the formation of clusters is thermodynamically disadvantaged. Differentiating eq. 3.1 with respect to the radius, and minimizing, we obtain the minimum size (critical radius) and the critical energy which must have a nucleus to grow and to reduce the overall free energy:

$$R_C \propto \frac{\gamma_{SL}}{k_B T ln\left(\frac{C}{C_0}\right)} \quad \text{and} \quad \Delta G_C \propto \frac{\gamma_{SL}^3}{\left[k_B T ln\left(\frac{C}{C_0}\right)\right]^2} \tag{3.2}$$

Eq. 3.2 shows that the critical radius R_C and the barrier energy ΔG_C are inversely proportional to the supersaturation. Consequently, the higher the supersaturation, the lower the energy barrier to overcome in order to form clusters.

The growth, however, occurs through generation of species that diffuse to the surface of the nuclei and, subsequently, are adsorbed. The growth process can then be controlled by diffusion or by surface processes (layer by layer growth or polynuclear growth). If the process is under diffusion control, the slow stage of reaction is in reaching the surface of the particle by the species and this allows obtaining monodisperse nanoparticles. Otherwise if the growth mechanism is controlled by surface processes, the slow stage of reaction is in absorbing species and this may lead either to a growth layer by layer or to a polynuclear growth. In the first case, growing species are embedded in a layer. Once the layer is completed, then a further layer starts to grow up. In the second case, the surface processes are so fast that the growth of the second layer occurs before the first one is completed.

Another consideration has to be taken into account about the surface energy. Liquid and amorphous solids have isotropic microstructures and thus isotropic surface energy. However, for a crystalline solid like gold, different crystal facets possess different surface energy and nanostructures with not exactly spherical shape are synthesized. For example, nanorod synthesis exploits the selective attachment of CTAB to some gold crystalline facets to orient the growth along one single axis.[4, 5] In some other cases, as it will be shown for nanoshells, complicated shapes have been prepared due to a polynuclear growth mechanism and to the effect of crystal facets energy.

Gold nanostructures synthesized with colloidal method, like spherical particles or nanoshells, present a negative surface charge that stabilizes them. Because of this charge density, electrostatic forces develop between the surface of the solid and the charged species in solution near the surface. Due to a combination of electrostatic forces, forces of entropic origin and Brownian motion, the concentration of counter-ions is higher near the surface of NPs and decreases with increasing distance from the surface. This non homogeneous distribution of ions near the surface can be described with the Electrical Double Layer theory.[6] Around the charged particle, a first layer of counter-ions, called Stern layer, is formed where ions are tightly bound to the surface and the potential decreases linearly with increasing distance. Instead in the second layer, called Gouy layer, ions diffuse and the potential decreases exponentially. Electrostatic repulsion between two particles derives from the surface charge which is attenuated by the presence of the double layer (Figure 3.1).

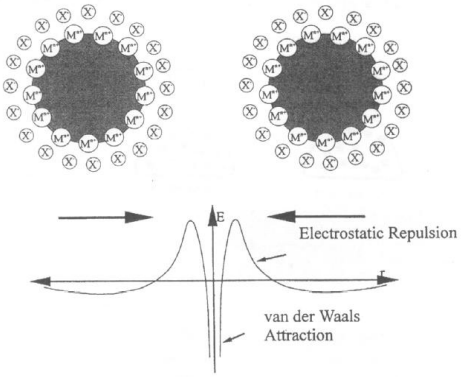

Figure 3.1: electrostatical stabilization of colloidal nanoparticles.

When two particles are far apart, there is no overlap between the two double layers and the electrostatic repulsion between the two particles is zero. Otherwise, when the two particles

approach, they start to repel each other because of double layers overlap. The double layer thickness decreases with increasing concentration and valence of the counter-ion, and increases with increasing dielectric constant of the solvent.

3.1.2. Gold nanoparticles

In the literature, there is a huge number of recipes for the synthesis of gold nanoparticles, both in water and in organic solvent, but the most popular ones are the synthesis developed by Turkevitch in 1951,[1] in water, and the Brust-Schiffrin method, in organic solvent, published in 1994.[2] We used both these methods to prepare gold nanoparticles in toluene and water. These systems were used as a model for the functionalization of gold nanoshells and nanorods.

3.1.2.1. Gold nanoparticles in water

In the well known Turkevitch[1] synthesis, $HAuCl_4$ is reduced by sodium citrate in water. Sodium citrate works both as reducing and stabilizing agent. By varying the ratio between $HAuCl_4$ and citrate and the reduction temperature, it is possible to prepare particles of different size and monodispersity and to red shift the plasmon band starting from approximately 520 nm. Briefly, in our standard synthesis, 10 ml of 10^{-3} M water solution of $HAuCl_4$ is boiled. To this solution, we add 1 ml of 0.04 M solution of sodium citrate in water.

3.1.2.2. Gold nanoparticles in toluene

The Brust-Schiffrin method[2] produces, in toluene, gold NPs of 1-3 nm in diameters in large amount and stable. The synthesis is quite simple, $HAuCl_4$ in water is transferred by TOAB into toluene. After the addition of the desired amount of dodecanethiol, $HAuCl_4$ is reduced by $NaBH_4$.

These NPs are, in general, stabilized by dodecanethiol but it is possible to functionalize them with other thiols either through place exchange reaction[7, 8] between different molecules or synthesizing them directly with the desired thiol group.[9]

In my opinion, the important limit of this synthetic route, besides the polydispersity, lies in the dimensions of the produced NPs, which are too small to present the surface plasmon resonance band. We are not interested in a precise NP size, but the particle should be large enough to show the plasmon band. The proportion thiol:$HAuCl_4$, used in the synthesis

controls the size of the AuNPs and a 1:6 ratio leads to the maximum average diameter of 5.2 nm[10, 11] To this aim, the Brust-Schiffrin synthesis has been repeated without the addition of thiol and the NPs were stabilized by TOAB. Varying the ratio between $HAuCl_4$ and TOAB it is possible to obtain larger NPs.[12]

We tried to prepare large NPs by this route, but they resulted less stable and so we decide to heat treat NPs. In the literature, there are some works[13-15] in which thermal processing in solid and in solution is described as a mean to increase NPs size and to reduce size dispersion. For example, Maye et al[13], after purifying NPs from thiol excess, heated the NPs dissolved in toluene at 110°C or in molten salt at 150°C. Instead, in Schadt et al work[15], solid NPs, inserted in a reaction tube, were placed in a preheated oven set at 149°C.

Our heat treatments were performed on NPs in solution, previously purified from the excess of dodecanethiol. The first type of annealing process consisted in a 1/10 reduction of solution volume by evaporation of the solvent from NPs' solution using a rotary evaporator with a thermal bath at 90°C. In this way, we obtained NPs with a small peak in the UV-visible spectrum at 505 nm, corresponding to the plasmon band. In the second one, we evaporated part of the solvent with a hot plate at 150°C to obtain NPs with a plasmon band at 518 nm. For both procedures, control of NPs size and reproducibility is quite difficult.

3.1.3. Gold nanorods

Gold NRs have been prepared by the group of Prof. Agostiano, Dept. of Chemistry at the University of Bari. I spent a month there to collaborate on the functionalization of these nanoparticles. The synthesis of gold NRs is a two-step process; first we prepared some seeds in solution and then we let them grow preferentially along one axial direction, thanks to a rod-like micellar environment.

Growth and seed solutions were prepared according to the protocol described by Jana et al.[4] Au seeds, smaller than 3 nm, were prepared by mixing equal portion of an aqueous 0.2 M CTAB solution and a 0.5 mM $HAuCl_4$ solution, followed by the injection of 10 mM $NaBH_4$ solution (0.6 mL) as reductant. Au seeds were then added to the growth solution composed by an aqueous solution of 0.08 M CTAB (3 mL) with 0.01 M $AgNO_3$ (0.03 mL). The growth solution was treated with 0.024 M $HAuCl_4$ (0.25 mL) and 0.08 M

ascorbic acid before the injection of the seed solution. In this way, we obtained 2.7 aspect ratio NRs, with a longitudinal plasmon band at 720 nm.

Before functionalization of NRs with organic solvents soluble dyes, NRs were transferred from water to toluene using the method described by Jebb et al.[16] A mixture of 2:3:4 water:dodecanethiol:acetone was able to transfer the nanorods into the organic layer. It took approximately 5 hours for the nanorods to migrate from water to the dodecanethiol layer.

3.1.4. Synthesis and deposition on glass substrates of gold nanoshells

The synthesis of NSs (SiO_2@Au) is a multi-step process (Figure 3.2) realized in water following the procedure developed by Pham et al.[17]

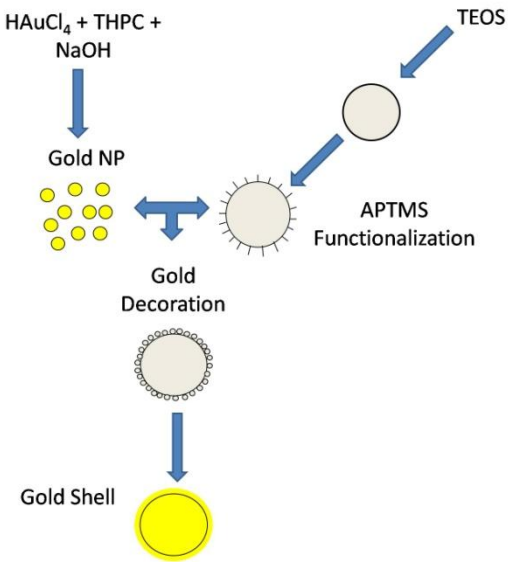

Figure 3.2: simple scheme describing the synthesis of gold nanoshells.

First of all, we synthesized the silica cores via the Stöber method.[18] The synthesis is quite simple, we mixed, in 50 ml of ethanol, different volumes (1.5-6 ml) of ammonium hydroxide 28%, the catalyst, and 1.5 ml of TEOS to obtain silica nanoparticles (NPs) of 20-250 nm in diameter. By increasing the amount of ammonium hydroxide, it is possible to prepare bigger silica nanoparticles. As shown in Figure 3.3, the radius of silica nanoparticles, measured with Dynamic Light Scattering technique, grows linearly with the amount of ammonium hydroxide following the empirical low:

$$y(nm) = -(24 \pm 6) + (24 \pm 3)x(ml) \quad (3.3)$$

Choosing accurately the volume of catalyst employed in the synthesis, we can obtain silica NPs of the desired size.

In the second step, we functionalized silica NPs with 3-aminopropyltrimethoxysilane (APTMS). These molecules, extending their amine groups outward as a new termination of the nanoparticle surface, act as a binding site for small colloidal gold particles (of about 2 nm dia.) prepared separately.[19]

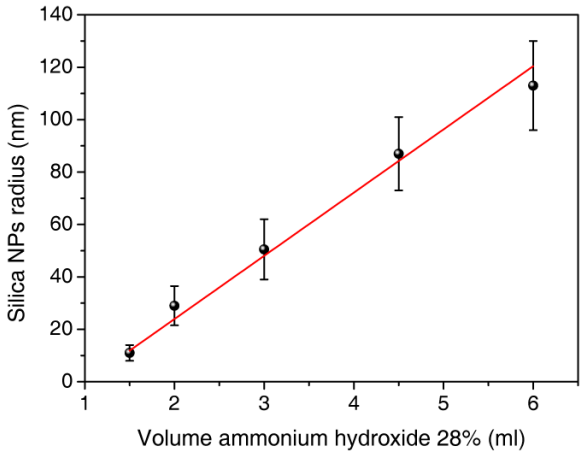

Figure 3.3: empirical trend of silica NPs radius with the volume of ammonium hydroxide 28%

Finally, the gold-decorated silica nanoparticles (50 µl – 1 ml) are used as nucleation sites for the reduction, by an aliquot of formaldehyde (0.6 ml), of an aged growth solution (8 ml) prepared with 25 mg of potassium carbonate in 100 ml of water and 1.5 ml of a 1% chloroauric acid. Nanoshells are stabilized by adding some PVP to the solution. By varying the ratio between the growth solution and the amount of gold-decorated silica particles, we achieved different thickness for the Au shell covering the silica core surface. As the amount of silica nanoparticles decreases, keeping the volume of the growth solution constant, gold is first reduced onto the colloidal adsorbates, subsequently the nucleation sites grow and begin to coalesce and form islands before achieving full coverage of the shell.

At least in theory, by using the above procedure we should be able, to cover cores of any size with a gold film of varying thickness. We limited the synthesis to silica NPs with three core radius (R_1): 50 ± 10 nm; 95 ± 15 nm and 158 ± 30 nm. The gold shell thickness, instead, varied between 10 and 50 nm.

The growth of a continuous, uniform Au layer on the dielectric core is the critical step in the synthesis of nanoshells, giving rise to their unique geometry-dependent plasmon resonant properties.[20] For the electromagnetic response of plasmonic nanoparticles to agree quantitatively with theory, it is critically important that the shell layer formation on the nanoparticle surface has a continuous and uniform morphology. The aqueous phase synthesis of gold nanoshells depends on the reduction of tetrachloroauric acid in the presence of a reducing agent. Several reducing agents have been reported for the synthesis of metallic nanoparticles and typically have a significant influence on the morphology of the final nanoparticle product.[21] Also associated with the use of certain reducing agents, have been variations in shell layer morphology due to specifics of reagent preparation. Both colloidal solutions and reductant solutions are known to change slowly over time, resulting in the growth of nanostructures with morphologies deviating from those achieved with freshly prepared solutions. These slow variations are most likely due to changes in equilibrium concentrations of the various ionic constituents or of dissolved gases and are quite challenging to monitor, as is their precise influence on shell layer growth.

All these elements make nanoshells synthesis a very sensitive process, which requires much care in operating and quite often, also in the literature,[21-25] leads to inhomogeneous and incomplete shell formation.

Gold NSs were deposited onto glass and ITO slides to measure their morphology and to prepare substrates suitable for SERS (Chap. 6) and Kelvin Probe (Chap. 7) measurements. In order to prevent particle movements during the AFM characterizations, glass substrates were functionalized with APTMS.[26]

All substrates were cleaned prior to silanization. The cleaning process involves a sequential sonication in different solvents: 10 minutes in deionised water, 10 minutes in acetone, 10 minutes in isopropyl alcohol, 10 minutes in acetone and finally, 10 minutes in deionised water again. APTMS monolayers were formed by dipping a sodalime glass into a 1 vol% solution in ethanol for 1 hour. Then the substrate was rinsed by sonication in toluene for 40 seconds. This process of dipping and sonication was repeated a second time to ensure full monolayer coverage.

Silanized substrates were characterized by contact angle measurements, that confirmed literature values.[27] The contact angle of a freshly silanized surface was 47° ± 2°, but aging the sample in closed polypropylene vials (in air) caused an increase of the angle value to

64° ± 3°. This might be due to the absorption of hydrophobic impurities from the atmosphere that change the surface wettability.

The substrates were immersed in the NSs solution for ~12 hours, then rinsed with water to remove an excess of the particles and finally dried by N_2 flow. By changing NSs solution concentration, it is possible to obtain slides coverage ranging from 10 to 99%.

3.2. Functionalization

The literature reports a large number of examples of gold nanostructures functionalization and usually the mechanism exploited to attach the dye changes depending on the molecular structure of the latter. Sometimes, the dye is used as stabilizing agent and so it is inserted in the reaction mixture before the nanoparticle is formed.[9, 28, 29] In this case, ad hoc synthesis reaction should be developed depending on the stability and solubility of the molecule. In other cases, the dye is attached after nanoparticle synthesis using an exchange place reaction[30-35].

We followed both cases and we always used excess dye in a ratio of 10000 molecules per particle, then we had to take particular care in the purification step of the final products to be sure to remove all the non bound dye. Depending on the molecule structure, the dye binds on the metal surface strongly with the thiol group or electrostatically with the amino group.

3.2.1. Spiropyran

In the family of photochromic molecules, one of the most studied system is spiropyran (SP) because of the reversible photochemical cleavage of the C-O bond in the spiropyran ring.[36] Upon UV light exposure, the hydrophobic SP isomerizes to the polar merocyanine (MC) form of the dye, which has a deep purple color; irradiation with visible light (white or in the 450-550 nm range) converts the MC open form into the colorless, nonpolar closed SP isomer. In Figure 3.4, the chemical structures of the spiropyran and of its open form merocyanine are shown. The closed and open forms of the dye present different properties (polarity, water affinity, optical properties) that could be used in holography,[36] to modify surface wettability,[37, 38] for sensing.[39]

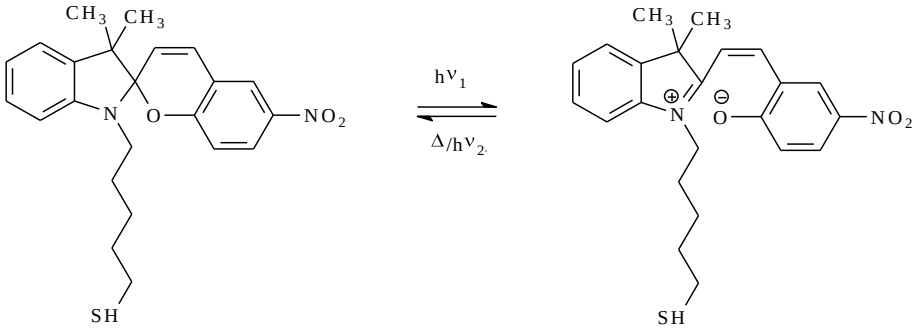

Figure 3.4: thiol terminated spiropyran (left) and merocyanine (right) structures.

Recently, SP and other similar photochromic[40] dyes have been used to functionalize silica and metal nanoparticles, with the aim to control particles aggregation through the different polarity[41] and molecule affinity[9] of the open and closed forms of the dye.

Thiol functionalized spiropyran dye was synthesized by Prof. Maggini group, at the Dept. of Chemical Science, of the University of Padova. We used it to functionalize NPs and NRs in toluene.

3.2.1.1. Spiropyran and gold nanoparticles

We synthesized gold NPs in toluene with the Brust-Shiffrin method[2] and annealed them, as described in paragraph 3.1.1.2, using the rotary evaporator. We obtained a 3×10^{15} NP/ml concentrated solution of small NPs with a plasmon band at approximately 505 nm.

To functionalize the NPs, we used in a place exchange reaction. We mixed a SP solution (0.012 g of SP in 2 ml of toluene) with 1 ml of NPs solution and we let stir all the night. The day after, we precipitated functionalized NPs mixing the organic solution with methanol and keeping it for one day at -15°C. In this way, NPs, which are less stable in cold methanol, precipitate whereas the SP molecules, not bound to NPs, stay in solution. SP-NPs are stable for months.

3.2.1.2. Spiropyran and gold nanorods

We synthesized gold NRs in water and we transferred them in toluene as described in paragraph 3.1.2. NRs were purified by dodecanethiol in excess before functionalization through place exchange reaction. We dissolved in 2 ml of NRs toluene solution, 1 mg of SP and we let stir all the night. The day after, we centrifuged NRs to purify them from the excess SP. Centrifugation reduced NRs stability and provoked their aggregation.

3.2.2. PEP-C3 and PEP-C12

PEP is a push-pull molecule composed by a π-deficient and a π-excessive heterocycle as the acceptor group A and the donor group D, respectively.[42] This kind of system, being dipolar, presents a relevant hyperpolarizability and good nonlinear optical properties, such as high two-photons absorption cross section. Our group, in collaboration with the group of Prof. Abbotto of the Dept. of Material Science at the University of Milano-Bicocca which synthesized the molecules, has thoroughly investigated the linear and nonlinear optical properties[43] of this class of push-pull systems for application on optical limiting and upconverted lasing devices.[44]

To improve the hyperpolarizability and in so doing the nonlinear optical properties, chemists modify the electron withdrawing and donating power of acceptor and donor groups, respectively, choosing more or less polar substituents. A new way proposed to further enhance the nonlinear optical responses is to exploit the local field on the surface of metal nanoparticles. To this end the group of Prof. Abbotto prepared a thiol-acetyl terminated PEP molecule, spaced by two different length alkyl chains, with 3 or 12 carbon atoms. The idea is to modify the effects on the linear and nonlinear optical properties depending on the distance between the dye moiety and the surface of the metal nanostructure.

In Figure 3.5, the chemical structures of the PEP molecules with different alkyl chain length are shown.

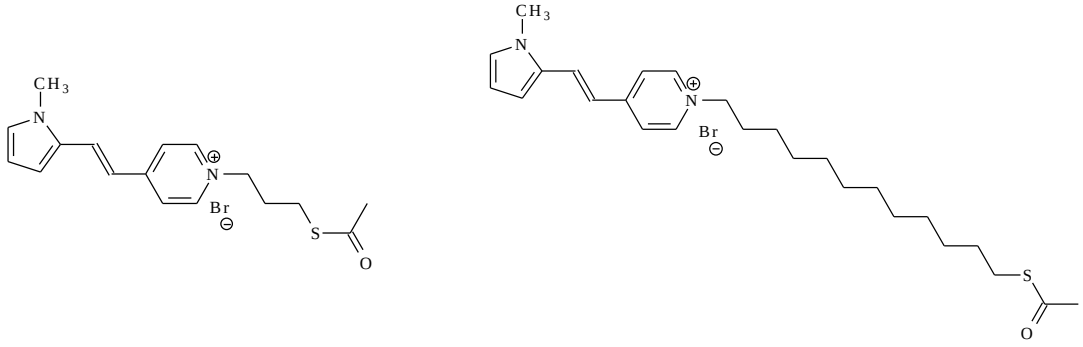

Figure 3.5: thiol-acetyl terminated PEP with 3 (left) and 12 (right) carbon atoms chain length.

We functionalized NPs, NRs and NSs with PEP. PEP is well soluble in ethanol; its solubility is a little lower in water, especially for PEP-C12-SH (the one with the long alkyl chain). The acetyl group prevents oxidation of the thiol group but it is useful to remove it prior to functionalize gold nanostructures. In fact, it is well known from the literature that

thioacetates react slowly with gold surfaces and organize in a less ordered SAM.[45] To deprotect the thiol group, we prepared a 10^{-3} M solution of both PEP in ethanol and we added 10 μl of NH_4OH. [46]

3.2.2.1. PEP and gold nanoparticles

We tried to functionalize NPs with deprotected PEP-C12-SH, without appreciable results, in two different ways. In the first one, we mixed 2 ml of NPs prepared previously with the Turkevitch method with 0.5 ml of a 10^{-4} M water solution of PEP-C12-SH. The problem was that NPs are electrostatically stabilized and PEP is positively charged. The presence of charged molecules provoked NPs aggregations well before thiol binding was accomplished. In the second method, we tried to prepare NPs using PEP-C12-SH as stabilizing agent. We mixed 1 ml of a 10^{-3} M solution of $HAuCl_4$ with 5 ml of a 10^{-4} M solution of PEP both in water prior to add the reducing agent ($NaBH_4$) but in this case, $HAuCl_4$ oxidized the pyridine group of PEP.

3.2.2.2. PEP and gold nanorods

We synthesized gold NRs in water as described in paragraph 3.1.2 and we dissolved 10 mg of deprotected PEP (the same method is used for both the dyes) in 2 ml of NRs solution; we let stir all the night. The day after, we centrifuged NRs to purify them from the excess PEP. Centrifugation reduced NRs stability and provoked their aggregation.

In Figure 3.6, infrared (IR) spectra of PEP-C3-SH (blue), CTAB (green), NRs (red) and PEP-C3-SH functionalized NRs (black) are reported.

In the IR spectrum of naked NRs (red), are clearly visible the vibrational modes characteristic of CTAB. At 2918 and 2850 cm^{-1}, there are the methylene C-H stretching modes and at 1480 cm^{-1} there are the alkyl bending vibrations. When we functionalized NRs with PEP-C3-SH (black line), in the IR spectrum new vibrational modes emerge that we associate to PEP-C3-SH (blu line): at 1604 cm^{-1} C=C aromatic stretching and at 1288 (not visible) and 1182 cm^{-1} C-N stretching.

The same signals are visible in Figure 3.7 in the IR spectra of PEP-C12-SH (green), NRs (red) as for PEP-C3-SH functionalized NRs (black). After functionalization, in the IR spectrum of NRs new vibrational modes emerge, at the same wavenumbers as for PEP-C3. In this case, the IR spectra are more noisy, probably because less dye molecules are bound to NRs.

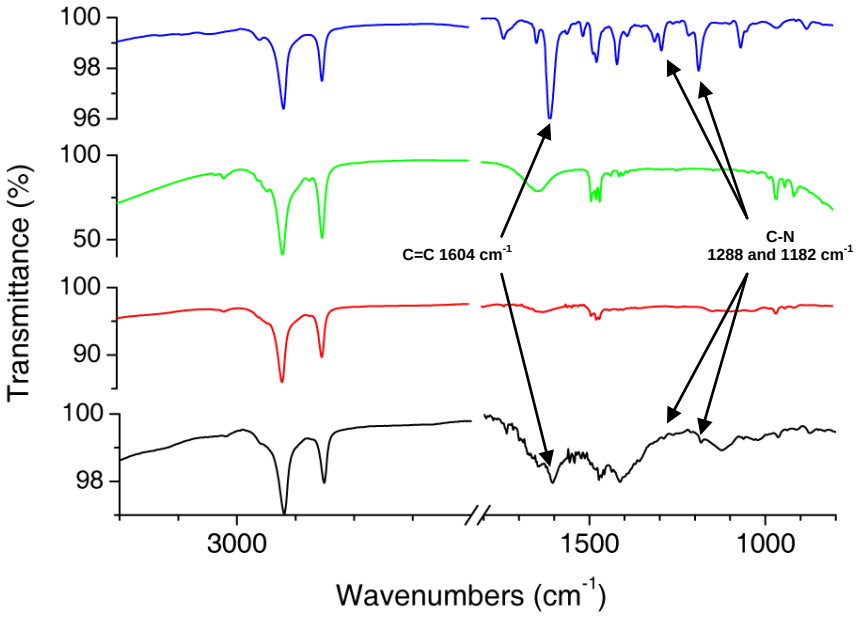

Figure 3.6: IR spectra of PEP-C3-SH (blue trace), CTAB (green trace), naked NRs (red trace) and PEP-C3-SH bound to NRs (black trace).

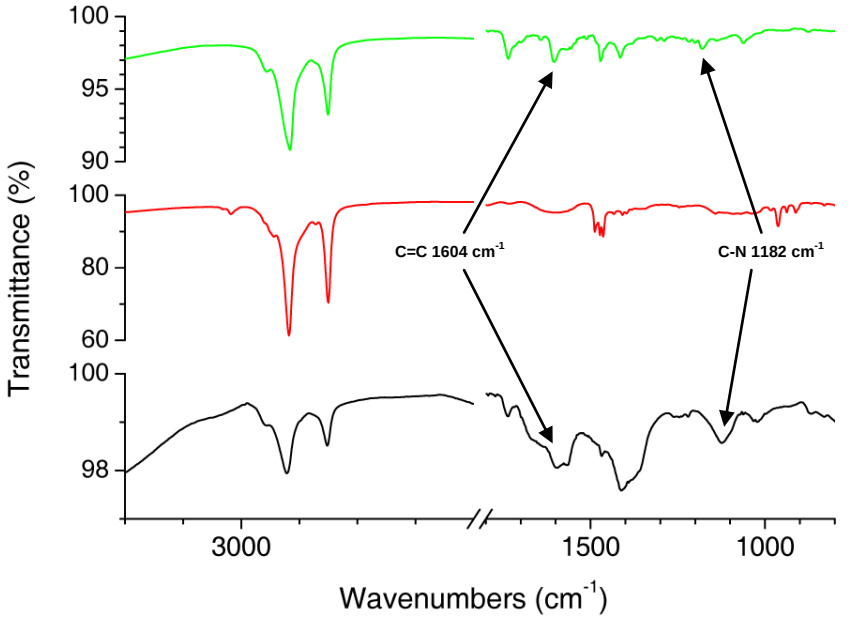

Figure 3.7: IR spectra of PEP-C12-SH (green trace), naked NRs (red trace) and PEP-C12-SH bound to NRs (black trace).

3.2.2.3. PEP and gold nanoshells

We synthesized gold NSs in water as described in paragraph 3.1.3. We mixed 4 ml of PVP stabilized NSs with 200 µl of a ethanol 10^{-3} M solution of deprotected PEP and we let it stir all the night. The day after, we centrifuged NSs to purify from the excess of PEP.

3.2.3. Rhodamine B

Rhodamine B (RhB) is one of the most commonly used dye. It is fluorescent (quantum yield in water 37%) and has good nonlinear optical properties. It is often used in literature to functionalized gold and silver nanostructures to demonstrate quenching or enhancement of fluorescence.[47, 48]

In Figure 3.8, the chemical structures of the RhB molecule is shown. RhB does not possess a thiol group but interacts electrostatically with the metallic surface through the amino and carboxylic groups.

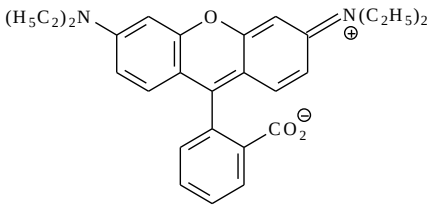

Figure 3.8: Rhodamine B molecular structure.

3.2.3.1. Rhodamine B and gold nanoshells

We synthesized gold NSs in water as described in paragraph 3.1.3. We mixed 4 ml of PVP stabilized NSs with 200 μl of a water 5×10^{-4} M solution of Rhodamine B and we let stir all the night. The day after, we centrifuged NSs to purify from the dye excess.

References

(1) Turkevich, J.; Stevenson, P. C.; Hillier, J. J. *Discuss. Faraday Soc.* **1951**, *11*, 55-75.

(2) Brust, M.; Walker, M.; Bethell, D.; Schiffrin, D. J.; Whyman, R. *J. Chem. Soc. , Chem. Commun.* **1994**, *7*, 801-802.

(3) Cao, G. In *Synthesis, properties and applications;* Imperial College Press: 2004; .

(4) Jana, N. R.; Gearheart, L.; Murphy, C. J. *Adv. Mater.* **2001**, *13*, 1389-1393.

(5) Nikoobakht, B.; El-Sayed, M. A. *Langmuir* **2001**, *17*, 6368-6374.

(6) Guozhong, C. In *Nanostructures and nanomaterials: synthesis, properties and applications;* Imperial College Press: 2004; .

(7) Hostetler, M. J.; Templeton, A. C.; Murray, R. W. *Langmuir* **1999**, *15*, 3782-3789.

(8) Woehrle, G. H.; Brown, L. O.; Hutchison, J. E. *J. Am. Chem. Soc.* **2005**, *127*, 2172-2183.

(9) Ipe, B. I.; Mahima, S.; Thomas, K. G. *J. Am. Chem. Soc.* **2003**, *125*, 7174-7175.

(10) Brust, M.; Fink, J.; Bethella, D.; Schiffrin, D. J.; Kiely, C. *J. Chem. Soc. , Chem. Commun.* **1995**, 1655-1656.

(11) Bethel, D.; Brust, M.; Schiffrin, D. J.; Kiely, C. *Journal of Electroanalytical Chemistry* **1996**, *409*, 137-143.

(12) Thomas, K. G.; K. Zajicek, J.; Kamat, P. V. *Langmuir* **2002**, *18*, 3722-3727.

(13) Maye, M. M.; Zheng, W.; Leibowitz, F. L.; Ly, N. K.; Zhong, C. J. *Langmuir* **2000**, *16*, 490-497.

(14) Shimizu, T.; Teranishi, T.; Hasegawa, S.; Miyake, M. *J. Phys. Chem. B* **2003**, *107*, 2719-2724.

(15) Schadt, M. J.; Cheung, W.; Luo, J.; Zhong, C. J. *Chem. Mater.* **2006**, *18*, 5147-5149.

(16) Jebb, M.; Sudeep, P. K.; Pramod, P.; Thomas, K. G.; Kamat, P. V. *J. Phys. Chem. B* **2007**, *111*, 6839-6844.

(17) Pham, T.; Jackson, J. B.; Halas, N. J.; Randall Lee, T. *Langmuir* **2002**, *18*, 4915-4920.

(18) Stober, W.; Fink, A.; Bohn, E. *J. Colloid Interface Sci.* **1968**, *26*, 62.

(19) Duff, D. G.; Baiker, A.; Edwards, P. P. *Langmuir* **1993**, *9*, 2301-2309.

(20) Brinson, B. E.; Lassiter, J. B.; Levin, C. S.; Bardhan, R.; Mirin, N.; Halas, N. J. *Langmuir* **2008**, *24*, 14166-14171.

(21) Graf, C.; Van Blaaderen, A. *Langmuir* **2002**, *18*, 524-534.

(22) Prasad, V.; Mikhailovsky, A.; Zasadzinski, J. A. *Langmuir* **2005**, *21*, 7528-7532.

(23) Park, S. E.; Park, M. Y.; Han, P. K.; Lee, S. W. *Bull. Korean Chem. Soc.* **2006**, *27*, 1341-1345.

(24) Phonthammachai, M.; Kah, J. C.; Jun, G.; Sheppard, C. J. R.; Olivo, M. C.; Mhaisalkar, S. G.; White, T. J. *Langmuir* **2008**, *24*, 5109-5112.

(25) Ye, J.; Van Dorpe, P.; Van Roy, W.; Lodewijks, K.; De Vlaminck, I.; Maes, G.; Borghs, G. *J. Phys. Chem. C* **2009**, *113*, 3110-3115.

(26) Gotesman, G.; Naaman, R. *Langmuir* **2008**, *24*, 5981-5983.

(27) Siqueira Petri, D. F.; Wenz, G.; Schunk, P.; Schimmel, T. *Langmuir* **1999**, *15*, 4520-4523.

(28) Zhou, J.; Beattie, D. A.; Ralston, J.; Sedev, R. *Langmuir* **2007**, *23*, 12096-12103.

(29) Ipe, B. I.; Thomas, K. G. *J. Phys. Chem. B* **2004**, *108*, 13265-13272.

(30) Chandrasekharan, N.; Kamat, P. V.; Hu, J.; Jones II, G. *J. Phys. Chem. B* **2000**, *104*, 11103-11109.

(31) Kometani, N.; Tsubonishi, M.; Fujita, T.; Asami, K.; Yonezawa, Y. *Langmuir* **2001**, *17*, 578-580.

(32) Tom, R. T.; Suryanarayanan, V.; Reddy, P. G.; Baskaran, S.; Pradeep, T. *Langmuir* **2004**, *20*, 1909-1914.

(33) Franzen, S.; Folmer, J. C. W.; Glomm, W. R.; O'Neal, R. *J. Phys. Chem. A* **2002**, *106*, 6533-6540.

(34) Dulkeith, E.; Ringler, M.; Klar, T. A.; Feldmann, J.; Javier, A. M.; Parak, W. J. *Nano Lett.* **2005**, *5*, 585-589.

(35) Li, C.; Liu, X.; Yuan, M.; Li, J.; Guo, Y.; Xu, J.; Zhu, M.; Lv, J.; Liu, H.; Li, Y. *Langmuir* **2007**, *23*, 6754-6760.

(36) Berkovic, G.; Krongauz, V.; Weiss, V. *Chem. Rev.* **2000**, *100*, 1741-1753.

(37) Rosario, R.; Gust, D.; Garcia, A. A.; Hayes, M.; Taraci, J. L.; Clement, T.; Dailey, J. W.; Picraux, S. T. *J. Phys. Chem. B* **2004**, *108*, 12640-12642.

(38) Dattilo, D.; Armelao, L.; Fois, G.; Mistura, G.; Maggini, M. *Langmuir* **2007**, *23*, 12945-12950.

(39) Wen, G.; Yan, J.; Zhou, Y.; Zhang, D.; Mao, L.; Zhu, D. *Chem. Commun.* **2006**, 3016-3018.

(40) Ahonen, P.; Schiffrin, D. J.; Paprotny, J.; Kontturi, K. *Phys. Chem. Chem. Phys.* **2007**, *9*, 651-658.

(41) Bell, N. S.; Piech, M. *Langmuir* **2006**, *22*, 1420-1427.

(42) Bradamante, S.; Facchetti, A.; Pagani, G. A. *Journal of Physical Organic Chemistry* **1997**, *10*, 514-524.

(43) Signorini, R.; Ferrante, C.; Pedron, D.; Zerbetto, M.; Cecchetto, E.; Slaviero, M.; Fortunati, I.; Collini, E.; Bozio, R.; Abbotto, A.; Beverina, L.; Pagani, G. A. *J. Phys. Chem. A* **2008**, *112*, 4224-4234.

(44) Abbotto, A.; Beverina, L.; Bozio, R.; Bradamante, S.; Ferrante, C.; Pagani, G. A.; Signorini, R. *Adv. Mater.* **2000**, *12*, 1963-1967.

(45) Bethencourt, M. I.; Srisombat, L.; Chinwangso, P.; Randall Lee, T. *Langmuir* **2009**, *25*, 1265-1271.

(46) Cai, L.; Yao, Y.; Yang, J.; Price, D. W.; Tour, J. M. *Chem. Mater.* **2002**, *14*, 2905-2909.

(47) Ray, K.; Badugu, R.; Lakowicz, G. R. *J. Phys. Chem. C* **2007**, *111*, 7091-7097.

(48) JZhu, J.; Zhu, K.; Huang, L. *Physics Letters A* **2008**, *372*, 3283-3288.

CHAPTER 4

Morphology

In this chapter, we describe the morphological characterization of gold nanostructures. We extensively studied nanoshells (NSs) morphology both with AFM (Atomic Force Microscopy) and TEM (Transmission Electron Microscopy). AFM and TEM microscopies give us complementary information not only about nanostructure's size but also about surface morphology.
The TEM characterization of naked and functionalized nanorods (NRs) is also performed.

4.1. AFM

Atomic force microscopy (AFM) belongs to the family of the Scanning Probe Microscopy (SPM) techniques.[1] In SPM, a 3-D scanning of a sample surface is performed using a special probe which locally interacts with the surface. The probe is placed near the surface ($d < 50$ nm). Depending on the specific type of interaction between the probe and the surface, different kind of microscopy can be distinguished, such as Atomic Force Microscopy (AFM), and Scanning Kelvin Microscopy (SKM), which are the two techniques used in this thesis.

In AFM (for SKM see Chap.7), we measure interatomic force, usually Van der Waals force, between the atoms on the sample surface and atoms on the tip of a special probe

made by an elastic cantilever with a sharp tip at the end (Figure 4.1). The force applied to the tip by the surface, results in bending of the cantilever. The cantilever deflection is detected by a laser beam focused on its back surface and reflected onto the area of a quad-photodiode. The cantilever deflection causes a displacement of the reflected beam over the four different sections of the quad-photodiode, allowing a precise detection of cantilever movements. The probe (or the sample) is moved on top of the sample (or under the probe) by a piezoelectric transducer (called scanner). Vertical movements are guided by a feedback system which keeps the surface-probe interaction fixed. These movements are recorded and used to determine the surface height. An electronic system measures the surface-probe interaction at every (x,y) point in the sample. The interaction strength depends on the sample-probe distance. By mapping the strength in the (x,y) points, we can reconstruct an image of the sample surface.

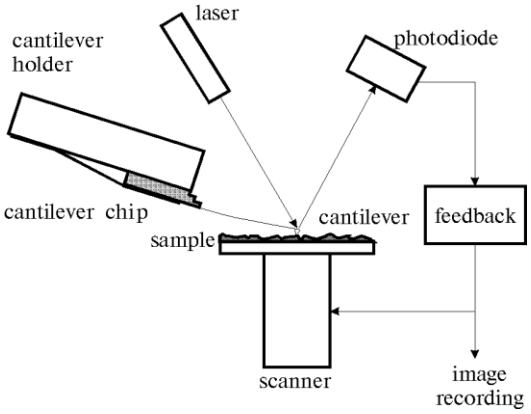

Figure 4.1: AFM scheme of the working system.

AFM instruments typically operate in three ways: contact mode (short range forces), non contact mode (long range forces) and semi-contact mode (Figure 4.2).

In the contact mode (Figure 4.2a), the tip touches the sample surface and the cantilever deflection is caused by the repulsive forces between the tip and the sample. There are two operation modalities for contact mode:

- constant force, the feedback system drives the piezoelectric actuator to keep the cantilever bending fixed;
- constant height, the tip height is kept constant and the different force strengths between tip and surface are recorded.

In non contact mode (Figure 4.2b), the cantilever, vibrating with a small amplitude, experiences the influence of a non-uniform force field near the sample surface. This interaction modifies the resonance frequency of the cantilever and physical information about the surface is obtained from these variations. This mode of operation is less detrimental to the sample but has worse lateral resolution.

In the semi-contact or tapping-mode (Figure 4.2c), the cantilever oscillates at its resonance frequency, like in non contact mode, but the tip touches the surface in an intermittent way. The tip moves in a field of both attraction and repulsion forces. Away from the surface the lever makes free oscillations, while, when there is an interaction with the surface, the oscillations amplitude is reduced until a set value (set-point) is reached. In this case, the piezoelectric actuator moves the cantilever in order to keep the oscillation amplitude fixed, reflecting the differences in the surface morphology. The surface morphology can be reproduced through the actuator movements. The advantages of this procedure are low sample damaging and good lateral resolution.

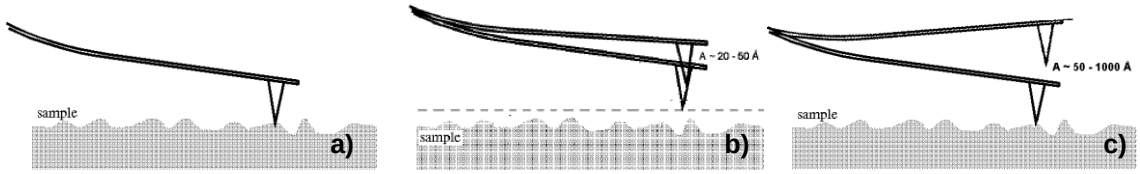

Figure 4.2: scheme of the AFM working modalities: a) contact; b) non contact; c) semi-contact.

By mapping the phase of the cantilever oscillation during the semi-contact mode scan, it is possible to obtain, in addition to topography, information about surface properties such as composition, adhesion, friction, viscoelasticity. Phase Imaging gives valuable information for a wide range of applications, in some cases giving contrast where none was anticipated from the material properties.

Atomic force microscopy (AFM) was performed with an NT-MDT (NT-MDT-Europe B.V., Nuenen, the Netherlands) instrument operating in air in the semi-contact mode with a 3-μm scanner. The operational scheme of the instrument is the classic scanning by sample in which the sample moves and the cantilever oscillates in a fixed position. The probe tip has a typical curvature radius of 10 nm, a cantilever resonant frequency of 200 kHz, and a force constant of 5.5 N/m. We characterized, both in topography and phase

contrast mode, gold NSs deposited on glass and ITO slides. These measurements gave us information about the silica nanoparticles and NSs size, metallic film coverage morphology, growth process and slides coverage.

Measurements have been performed in collaboration with Dr. Piero Schiavuta and Dr. Francesco Marinello at Nano Fabbrication Facility – NanoFab (Venice).

4.1.1. Nanoshells growth process

The growth process of gold shell on silica nanoparticles is well described in the work of Oldenburg et al[2] in which TEM images show the nuclei growth and coalescence. Briefly, a subsequent reduction of an aged mixture of chloroauric acid and potassium carbonate by a solution of formaldehyde, where the gold-decorated silica nanoparticles are used as nucleation sites for the reduction, results in an increasing coverage of gold on the nanoparticle surface. We exploited AFM phase contrast images to confirm this mechanism and give greater details in the morphology of the gold shell produced in our lab (Figure 4.3). A phase contrast image of a 100 nm diameter silica colloid decorated with gold nanoparticles is shown in Figure 4.3a. The seed colloid adsorbates increase in size as reduction proceeds. During the reduction, colloids begin to coalesce on the nanoparticle surface (Figure 4.3b) until, finally, the apparent formation of a continuous metallic nanoshell on the dielectric nanoparticle surface can be observed (Figure 4.3c).

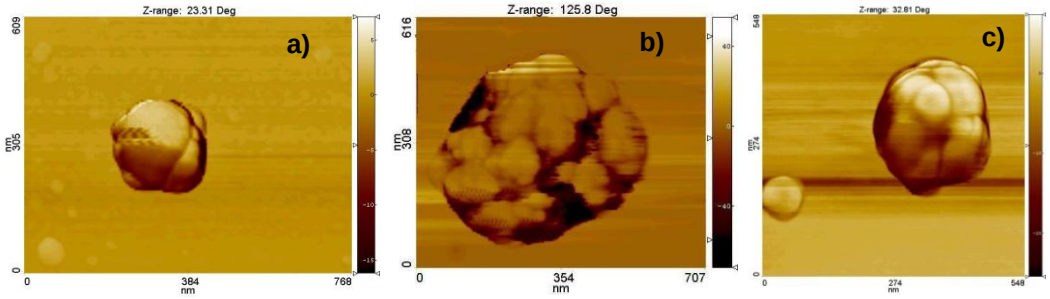

Figure 4.3: AFM contrast images: a) silica nanoparticle (R = 50 nm) covered by some large nuclei; b) nuclei on the silica nanoparticle grow and start to coalesce; c) complete shell.

4.1.2. Silica nanoparticles and nanoshells size

In this section, we present some images of NSs with different core and shell thickness.

In Figure 4.4, we show two examples of silica nanoparticles of different size. Through the topography images (Figures 4.4a e 4.4c) we evaluate the diameter (D) and the distribution of the two silica nanoparticles: for the small one D = 189 ± 10 nm , for the large D = 315 ± 30 nm. The error is likely underestimated, because we were able to average only on a small number of nanoparticles but from the topography images it is clear that smaller or larger nanoparticles are present, especially for larger silica nanoparticles batch. Silica nanoparticles tend to organize in a hexagonal close-packed structure but nanoparticles of different size create some defects in the packing. From the phase contrast images (Figures 4.4b and 4.4d), we can see that small nanoparticles present a quite smooth surface, instead the larger ones are inhomogeneous and present some branches that contribute to create defects on the packing and make size distribution broader.

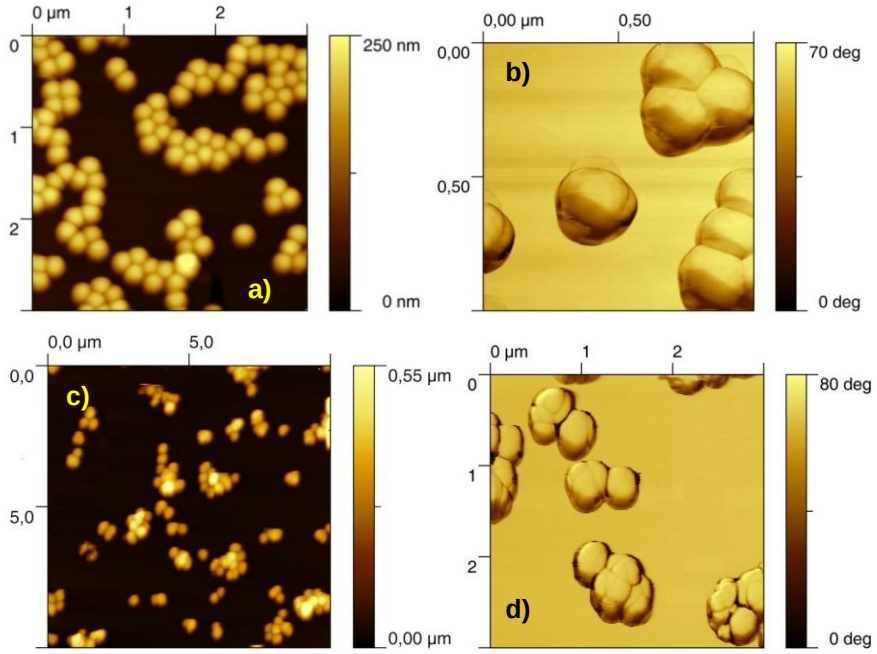

Figure 4.4: AFM a) topography and b) phase contrast images of silica nanoparticles of 189 nm diameter; c) topography and d) phase contrast images of silica nanoparticles of 315 nm diameter.

In Figures 4.5 and 4.6, we compare different NSs thickness for the same core size (R_1 = 95 nm in Figure 4.5 and R_1 = 158 nm in Figure 4.6). The NSs distribution appears quite broad especially for thicker shells. In fact, as we can see in figures 4.5b and 4.6b, NSs with a thicker coverage become more irregular because of the growth mechanism. Once nuclei grow and coalesce to form the film, further reduction of $HAuCl_4$ takes place on the shell creating larger domains and broader size distribution. Thin coverage (Figures 4.5d

and 4.6d) are instead homogeneous and coalescence of nuclei in small uniform domains is clearly visible. If the core surface is irregular, as for large silica nanoparticles, shell will grow irregular as well.

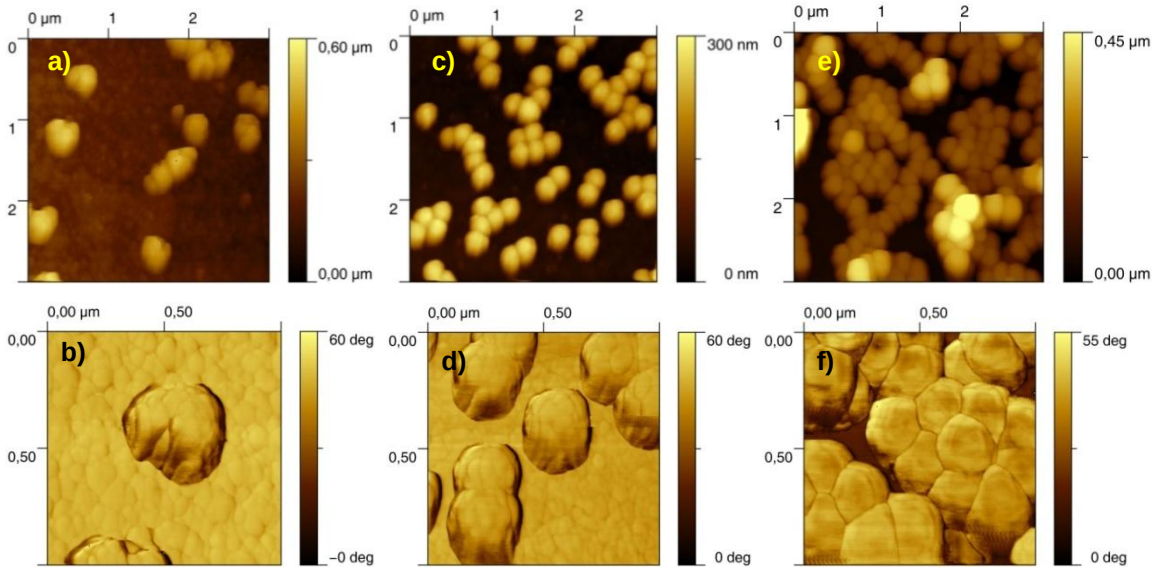

Figure 4.5: topography (top) and phase contrast (bottom) images of NSs with inner R_1 = 95 nm and outer radius: a) and b) R_2 = 138 ± 13 nm; c) and d) R_2 = 108 ± 6 nm; e) and f) R_2 = 95 ±5nm.

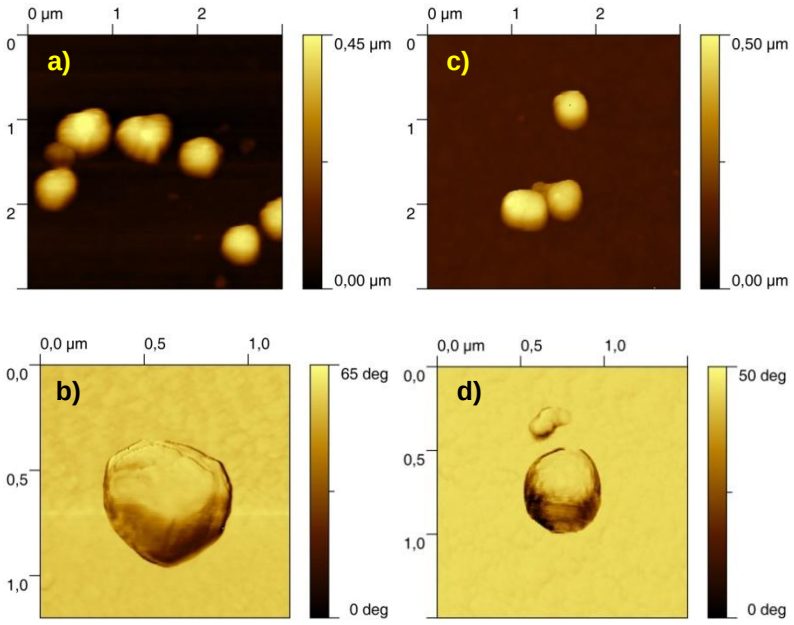

Figure 4.6: topography (top) and phase contrast (bottom) images of NSs with inner R_1 = 158 nm and outer radius: a) and b) R_2 = 198 ± 19 nm; c) and d) R_2 = 175 ± 7 nm.

The surface morphology of single particle influences the NSs aggregation. Particles covered by an irregular shell, as NSs with a thick coverage, aggregate randomly. Instead, more regular particles self-assemble in a hexagonal close-packed structure.

4.2. TEM

The origin of each mode of TEM analysis, is the Coulomb interaction between an electron beam and the atoms in the sample, which generates a series of signals useful to characterize materials.[3] We must distinguish between elastic and inelastic scattering. The former is used to construct images (including electron diffraction), while the latter gives rise to the spectroscopic analysis. From scattered and transmitted electrons, Auger electrons and X-ray, we can obtain information about:

- morphology and lattice image (bright field BF, dark field DF and high-resolution HRTEM images);
- crystal structure and symmetry (selected area electron diffraction SAED)
- composition (Energy Dispersive X-ray Spectroscopy EDS, Electron Energy Loss Spectroscopy EELS).

Generally, a Transmission Electron Microscope consists of three basic parts (Figure 4.7): the source of electrons, the system objective lens and the sample-block display with projectors, screens and EELS spectrometers.

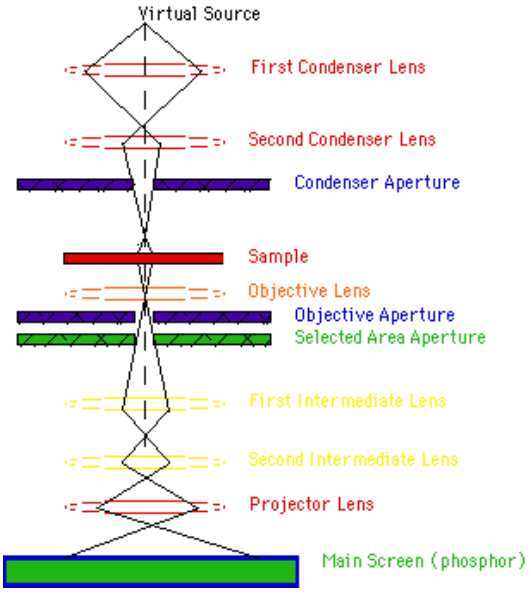

Figure 4.7: schematic structure of TEM.

The "virtual source" represents the electron gun, which is the source of electrons. This is based on field emission (FEG), i.e. the electrons are extracted after applying a potential difference on a tungsten filament. This type of source provides a more temporal and spatial coherence of the electron beam. The beam is then homogenized by a diaphragm placed immediately after the filament. The whole system needs a vacuum that is greater than 10^{-8} Pa for the source, while it is reduced to 10^{-6} Pa along the column (to avoid spread of the beam and contamination of the sample) and 10^{-3} Pa close to the screen that collects the image. The beam is then focused by two condenser lenses which are used to vary the geometry of the beam from parallel to convergent, depending on the type of analysis desired.

Magnetic lenses are used to focus and deflect the electrons. They consist of toroidal coils with an applied current, generating a magnetic field with a cylindrical symmetry and the axis directed parallel to the direction of the electron beam. By varying the intensity of current through the toroidal coils, electrons are deflected by the magnetic field. Like all lenses, even the magnetic ones have aberrations that affect the resolution available: spherical aberration, due to non-paraxial ray; chromatic aberration, due to dispersion in the electron beam energy; astigmatism due to the inhomogeneity of the magnetic field. The objective lens collects the rays of electron beam scattered and diffracted by the sample and focuses them on the focal plane, where it is possible to collect the diffraction image. Beyond the focal plane, rays are recombined, interfering with each other, to generate the image of the sample on the image plane. The intermediate and projector lenses magnify it on the screen. Directly facing the sample, there is an Energy Dispersive Spectrometer (EDS) which analyses the energy of the X-ray produced by the interaction of the electron beam with the sample. Another accessory, that may be present on a TEM, is an Electron Energy Loss Spectrometer with magnetic prism which analyses the energy of the electrons that have crossed the sample.

Structural and compositional characterization of NSs was performed, in collaboration with the group of Prof. Mattei (Dept. Physics at the University of Padova), by TEM at CNR-IMM (Bologna, Italy) with a field-emission gun (FEG) microscope (FEI Tecnai F20 Super Twin) operating at 200 kV equipped with an EDAX energy-dispersive X-ray spectrometer (EDS) and a Gatan STEM controller for performing scanning transmission electron microscopy (STEM). For NRs, we used TEM at the National Nanotechnology

Laboratory (NNL, Lecce, Italy). It is a Jeol model JEM-1011 microscope, operating with an acceleration voltage of 100 kV.

4.2.1. TEM characterization of nanoshells

Nanoshells with an inner and outer radius of $R_1 = 95 \pm 4$ nm $R_2 = 110 \pm 4$ nm, measured by AFM, were also characterized by TEM. A TEM Bright-Field (BF) micrograph of the silica particles is shown in Figure 4.8a: the silica nanoparticles exhibit a mean diameter <D> = 167 nm with a standard deviation of the size distribution σ = 12 nm (see Figure 4.8b), i.e. corresponding to an average nanoparticle radius $R_{TEM} = 84 \pm 6$nm. In the BF image of silica nanoparticles functionalized by 3-aminopropyltrimethoxysilane (APTMS) (Figure 4.8c), it is visible an organic layer with a thickness of about 10 ÷ 15 nm. Some organic shells form necks around NPs. The presence of C on the projection of the core-region of the particles (Table 4.1) is due both to the organic shell covering the particles and to the carbon film on which the SiO_2 particles are deposited for TEM analysis.

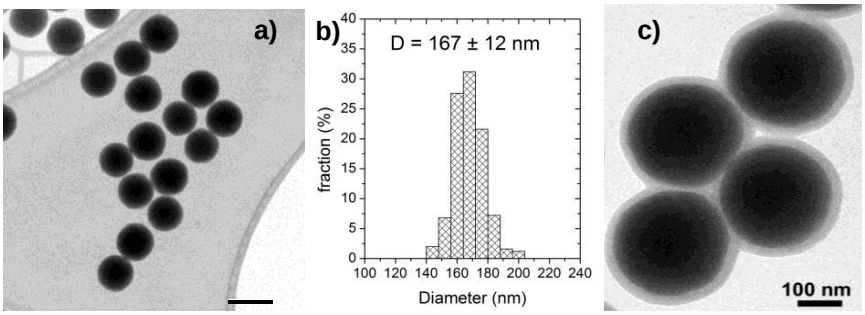

Figure 4.8: a) BF-TEM image and b) size distribution of the silica nanoparticles; c) BF-TEM image of the SiO_2@APTMS NPs.

The atomic ratio O/Si found by EDS compositional analysis is about 2.2 ± 0.2 (Table 4.1).

Table 4.1: EDS compositional results obtained focusing the electron beam on the core and on the shell region of a silica nanoparticles.

Region:	**Core**	**Shell**
Element	**Atomic %**	**Atomic %**
C (K)	74	99
O (K)	18	1
Si (K)	8	0

This can be an indication of a slightly less dense silica, as sometimes it is found for the Stöber synthesis. The silica core radius measured by AFM is slightly larger than that measured by TEM: this 10% discrepancy can be ascribed to the different spatial resolution and sensitivity of the two techniques but also to a possible shrinking effect of the not-fully densified NPs under the TEM electron beam.[4]In Figure 4.9, we show the BF micrographs of silica nanoparticles covered by gold nuclei. In this sample SiO_2/Au composite particles are present having a total mean diameter <D> = 175 nm with a standard deviation of the size distribution σ = 10 nm. The silica cores are covered by well defined Au NPs (see Figure 4.9b) having mean dimension of about 2 nm. The atomic ratio Au(L)/Si(K) on the particles found by EDS compositional analysis (see Table 4.2) is about 0.03, corresponding to a density of Au NPs on SiO_2 particle surface of about 0.07 NPs/nm^2 (assuming the bulk density for Au and a slightly less dense SiO_2).

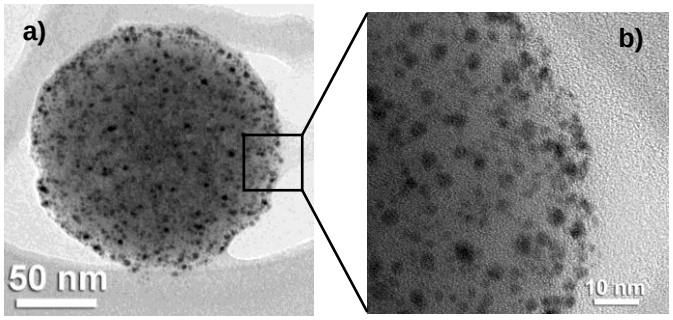

Figure 4.9: BF-TEM images at different magnifications of the silica nanoparticles covered with Au nuclei of about 2 nm size.

Table 4.2: EDS compositional analysis on silica nanoparticles covered by gold nuclei.

Element	Atomic %
C (K)	73.9
O (K)	18.8
Si (K)	7.1
Au (L)	0.2

Figures 4.10 a and b show the BF-TEM images of gold NSs with a spherical shape and a mean diameter <D> = 220 nm with a standard deviation of the size distribution σ = 15 nm, perfectly comparable with the value obtained by AFM. Few smaller or irregularly shaped NSs are also visible in Figure 4.10a. The contrast analysis of the TEM image

(Figure 4.10b) indicates that the Au shell covering the silica particles is not continuous, i.e., its thickness is not homogeneous. HR-TEM analysis (Figures 4.10 c and d) confirmed that the Au shell is polycrystalline, as can be expected from the colloidal-nucleated growth of the fabrication process (Chap. 3).

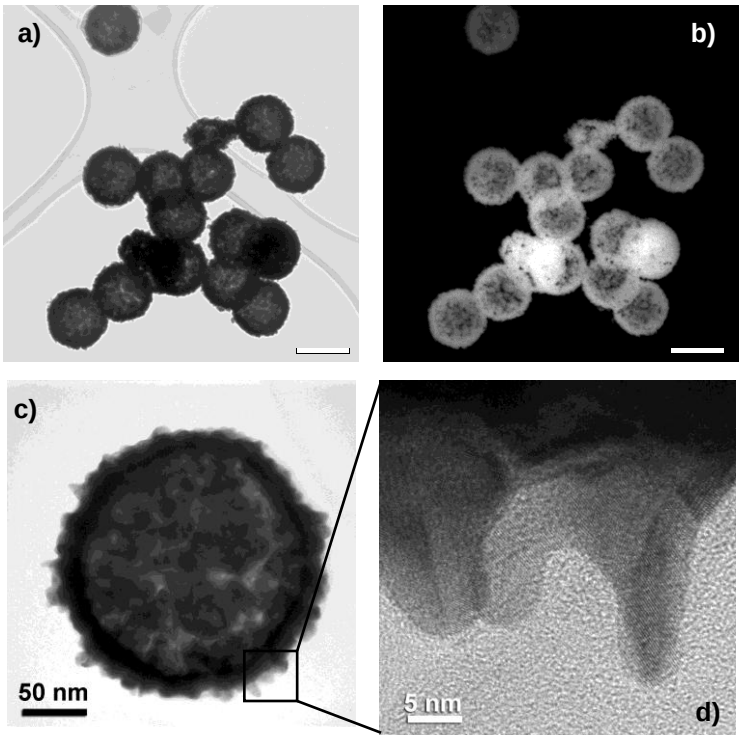

Figure 4.10: TEM images of gold NSs at different magnification. a) e b) BF images (in b the contrast is reversed to enhance the shell visibility); c) and d) High-Resolution TEM images in which the Au (111) crystalline planes are well visible.

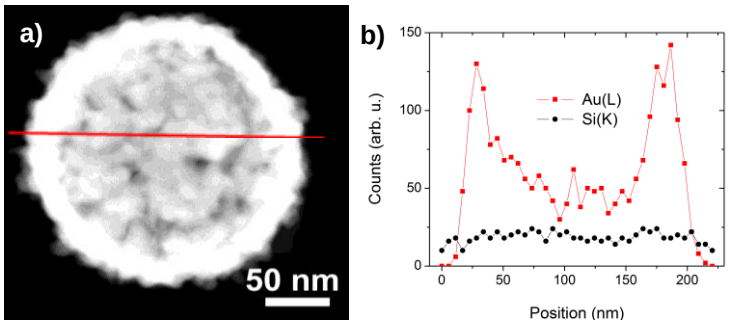

Figure 4.11: a) Scanning TEM Dark-Field images of a NS. The Au shell, giving a brighter contrast, is well visible. b) Au(L) and Si(K) compositional profile for a NSs obtained by scanning a 1nm (FWHM) electron beam on the red line showed in S-TEM Dark-Field image.

The Au surface appears very rough or bumpy. Therefore the definition of the size has been done by radially averaging the image intensity, so as to average the roughness effect.

Figure 4.11a show a Dark Field-Scanning TEM image of a nanoshell while in Figure 4.11b the corresponding EDS line-scan for Au and Si X-ray signal across the particle shown in the Z-contrast image. The total atomic ratio Au(L)/Si(K) in the core-shell particles found by EDS compositional analysis (see Table 4.3) is about 3.5.

Table 4.3: EDS compositional analysis on silica nanoparticles covered by gold shell.

Element	Atomic %
C (K)	61
O (K)	12
Si (K)	6
Au (L)	21

We performed also some TEM measurements on large NSs with inner radius R_1 = 158 nm, confirming both AFM analysis and TEM results obtained on small NSs. Figure 4.12 shows the BF-TEM image of some large NSs. They are not spherical and present a more inhomogeneous size distribution comparing with the small particles (as demonstrated by AFM characterization). The Au shell covering the silica particles is not continuous and there are several holes on the film.

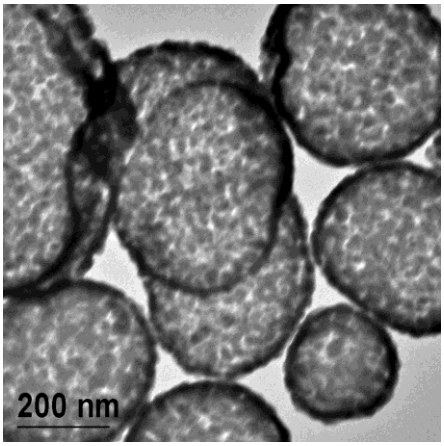

Figure 4.12: BF TEM image of gold large NSs.

The irregular morphology of gold shells observed in the TEM images is very interesting. In fact, in the literature, several works report stronger electromagnetic local

field in irregular and tip shaped metal nanostructures comparing to symmetric and spherical particles.[5-7] Both SERS signals[8] and two-photon absorption[6] are amplified if molecules are located in "hotspots" of nanoparticles aggregates. "Hotspots" are due to the interaction of the particles in clusters leading to a concentration of the plasmon amplitude into interstitial spots among a few particles, producing giant local fields in subwavelength sized areas, called "hotspots".

Moreover, local field on sharp tips are also demonstrated to be strong. For example, Kelly et al[5] calculated, using DDA method, the electromagnetic field enhancement on the contours external to the Ag trigonal prism and they estimated it to be over 500 times the applied field.

In the light of these considerations, we predict a stronger local field on these rough and bumpy surfaces comparing to uniformly covered nanoshells and a larger enhancement of linear and nonlinear optical properties of molecules functionalizing the nanostructures.

4.2.2. TEM characterization of nanorods

TEM measurements have been performed on naked and functionalized NRs. In Figure 4.13, micrographs of NRs transferred in organic solvents[9] and stabilized by dodecanethiol (DDT) (Figure 4.13a) and NRs stabilized by dodecanethiol and spiropyran (SP-C6-SH) (Figure 4.13b), both after 20 hours, are shown.

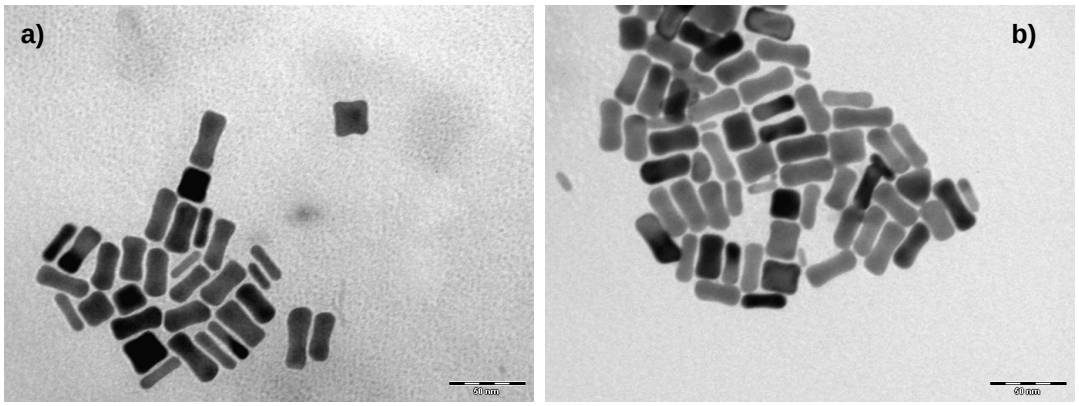

Figure 4.13: BF TEM images a) NRs in dodecanethiol; b) NRs stabilized by dodecanethiol and spiropyran.

NRs stabilized by DDT have the long axis $R_{long\ axis} = 32 \pm 4$ nm and the short one $R_{short\ axis} = 12 \pm 4$ nm. After the place exchange reaction between DDT and SP-C6-SH, NRs

maintain the same size within the experimental error: $R_{long\ axis}$ = 32 ± 4 nm and the short one $R_{short\ axis}$ = 13 ± 3 nm. Both NRs are well separated and exhibit minimal changes in shape and size as a result of thiol interactions.

In Figure 4.14, BF images of naked (Figure 4.14a) and PEP-C12-SH functionalized (Figure 4.14b) NRs are shown. Naked NRs have the long axis $R_{long\ axis}$ = 30 ± 4 nm and the short one $R_{short\ axis}$ = 10 ± 3 nm. After the functionalization with PEP-C12-SH, NRs there seems to be a slight reduction in NRs size, even if within the experimental error: $R_{long\ axis}$ = 27 ± 5 nm and $R_{short\ axis}$ = 9 ± 3 nm.

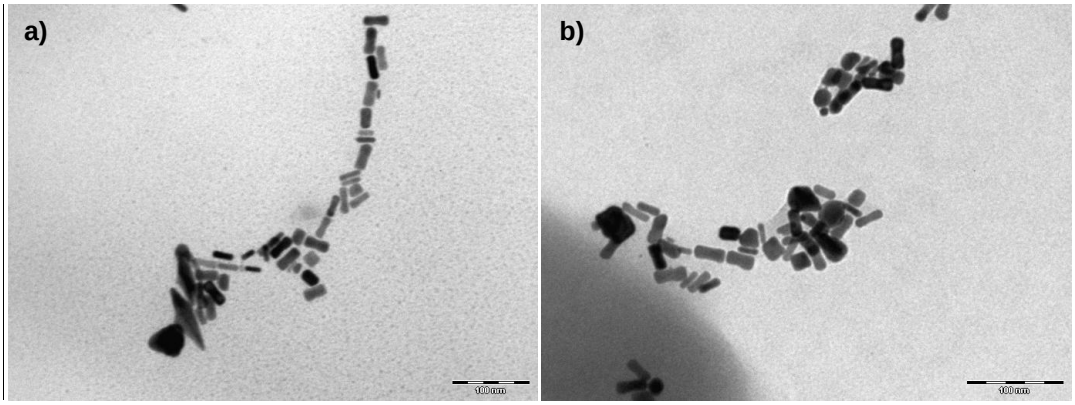

Figure 4.14: BF TEM images a) NRs in water; b) NRs functionalized by PEP-C12.

NRs morphological changes are more evident for NRs functionalized with PEP-C3-SH (Figure 4.15).

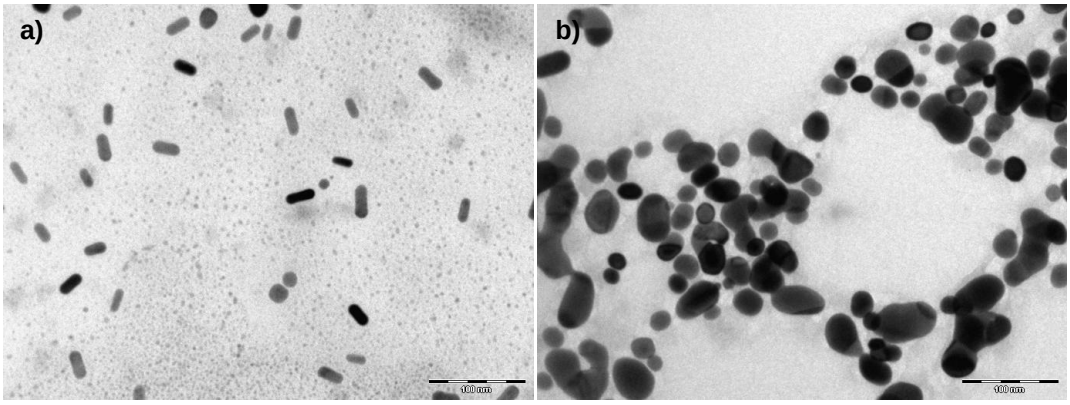

Figure 4.15: BF TEM images a) naked NRs; b) NRs functionalized by PEP-C3.

Naked NRs (Figure 4.15a) have the long axis $R_{long\ axis}$ = 26 ± 4 nm and the short one $R_{short\ axis}$ = 11 ± 2 nm. In contrast, the TEM image obtained with the PEP-C3-bound NRs sample

shows rods with distorted structures. This indicates that the surface modification of the NRs with PEP-C3-SH leads to the destruction of their protective capping layer, provoking the loss of the rod-like shape to assume shapes ranging from ellipsoidal to spherical.

This effect is not new in the literature; for this kind of nanostructures, reshaping in spherical nanoparticles, under laser pulse illumination, is common.[10] In this case, reshaping is not due to melt of gold, but it is due to etching of the surface by PEP-C3-SH during the penetration of the dye molecules inside the double CTAB layer, as observed for the place exchange reaction between DDT and $Ru(bpy)_3^{2+}$-C5-SH.[9]

Etching of the surface of gold nanoparticles by different length thiols was previously demonstrated by Wilcoxon and Provencio.[11] In their work they observed that the corrosion process is more effective for short thiol chains. Starting from this finding, we can explain why the phenomenon is strong for PEP-C3-SH and hardly visible for PEP-C12-SH, but this is not enough to justify the absence of etching for NRs functionalized by spiropyran.

In this case, we have to add two considerations. In the literature it is reported that addition of electrons to gold nanorods with aspect ratios ranging from 2 to 4 has been found to change the morphology as a result of surface charging effects.[12] The redox nature of the PEP moiety, compared to the one of spiropyran group, is likely to make the thiol interaction more reactive for the PEP substituted thiols and induce surface corrosion for these compounds. The second, simple consideration is that, as shown in the IR spectrum in Chapter 3, less SP-C6-SH units are bound to NRs in comparison with PEP-C12-SH and PEP-C3-SH, therefore the etching effects should be lower for SP-C6-SH.

References

(1) Howland, R.; Benatar, L. In *A practical guide to scanning probe microscopy;* 2000.

(2) Oldenburg, S. J.; Averitt, R. D.; Westcott, S.; Halas, N. J. *Chemical Physics Letters* **1998**, *288*, 243-247.

(3) Feldmann, L. C.; Mayer, J. W. In *Fundamentals of Surface and Thin Films Analysis*.

(4) Van Blaaderen, A.; Kentgens, A. P. M. *J. Non-Cryst. Solids* **1992**, *149*, 161-178.

(5) Kelly, K. L.; Coronado, E.; Zhao, L. L.; Schatz, G. C. *J. Phys. Chem. B* **2003**, *107*, 668-677.

(6) Wenseleers, W.; Stellacci, F.; Meyer-Friedrichsen, T.; Mangel, T.; Bauer, C. A.; Pond, S. J. K.; Marder, S. R.; Perry, J. W. *J. Phys. Chem. B* **2002**, *106*, 6853-6863.

(7) Wang, H.; Wu, Y.; Lassiter, B.; Nehl, C. L.; Hafner, J. H.; Nordlander, P.; Halas, N. J. *PNAS* **2006**, *103*, 10856-10860.

(8) Kneipp, K.; Kneipp, H.; Kneipp, J. *Acc. Chem. Res.* **2006**, *39*, 443-450.

(9) Jebb, M.; Sudeep, P. K.; Pramod, P.; Thomas, K. G.; Kamat, P. V. *J. Phys. Chem. B* **2007**, *111*, 6839-6844.

(10) Link, S.; El-Sayed, M. A. *Int. Revews in Physical Chemistry* **2000**, *19*, 409-453.

(11) Wilcoxon, J. P.; Provencio, P. *J. Phys. Chem. B* **2003**, *107*, 12949-12957.

(12) Novo, C.; Mulvaney, P. *Nano Lett.* **2007**, *7*, 520-524.

CHAPTER 5

Linear optical properties of gold nanostructures

In this chapter, we describe the linear optical properties of nude and functionalized gold nanostructures. We compare surface plasmon band position for different shape nanoparticles using UV-visible spectroscopy and we focus on the effect on the emission properties of molecules functionalizing nanoparticles.

5.1 UV-visible absorption

The intense colour of colloidal gold nanostructures is due to their surface plasmon absorption.[1] Depending on the particle properties, as shape, dimensions or surrounding environment, the surface plasmon band changes its wavelength position. For example gold spherical nanoparticles (NPs) are red, gold nanorods (NRs), because of the longitudinal plasmon peak, are blue or violet depending on the aspect ratio and gold nanoshells (NSs) should be red, blue, violet, green and so on depending on the inner and outer radius ratio.

In general, the surface plasmon band is rather narrow (about 100 nm) but may become broad if nanoparticles are non uniform in size and shape[2-4] or if they aggregate.[5]

In the next paragraphs, we show UV-visible spectra of nude and functionalized gold nanostructures.

5.1.1 Gold nanoparticles

Gold NPs present a plasmon resonance which is not widely tunable. Usually the plasmon peak wavelength ranges between 510 and 580 nm, depending on the particle size.

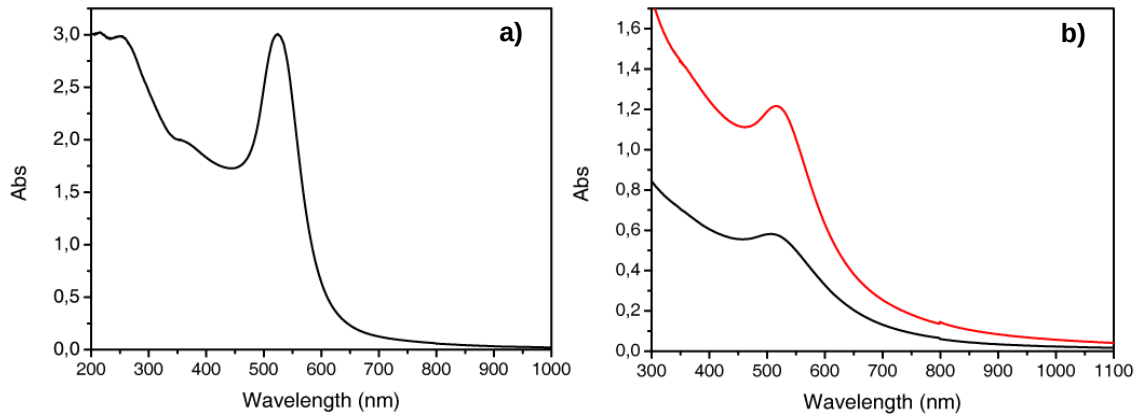

Figure 5.1: UV-visible absorption spectra of gold NPs: a) in water; b) in toluene, with two different annealing treatment (rotary evaporator annealing in black, hot plate in red).

In Figure 5.1, UV-visible absorption spectra of gold NPs in water and in toluene are shown (the synthesis is described in Chap. 3). The NPs in water present a narrow band peaked at 524 nm. For NPs in toluene annealed in rotary evaporator and with hot plate, the plasmon oscillations are strongly damped and a weak and broad absorption band is peaked at 505 (black trace) and 518 nm (red trace), respectively. This behavior can be phenomenologically explained considering that, on reducing the cluster size, the mean free path is limited. If the electrons scatter with the surface in an elastic but totally random way, the coherence of the overall plasmon oscillation is lost.[1] A second explanation to the plasmon band weakening and broadening is given by the chemical interface damping (CID) model.[6,7] In this model, the empty LUMOs of the acceptor molecules on the particle surface are coupled to the free electrons in the conduction band of the metal. After excitation of a plasmon resonance, electrons transfer between the levels becomes possible and this causes, again, loss of coherence in the plasmon oscillation.

With the hot plate annealing treatment, we obtain larger NPs comparing with the rotary evaporator one, so the plasmon band is red shift and less broad.

5.1.1.1. Gold nanoparticles functionalized with PEP-C12-SH in water

The UV-visible characterization of PEP-C12-SH functionalized NPs gives some informations about NPs stability after molecules attach and chemical modifications of reactants.

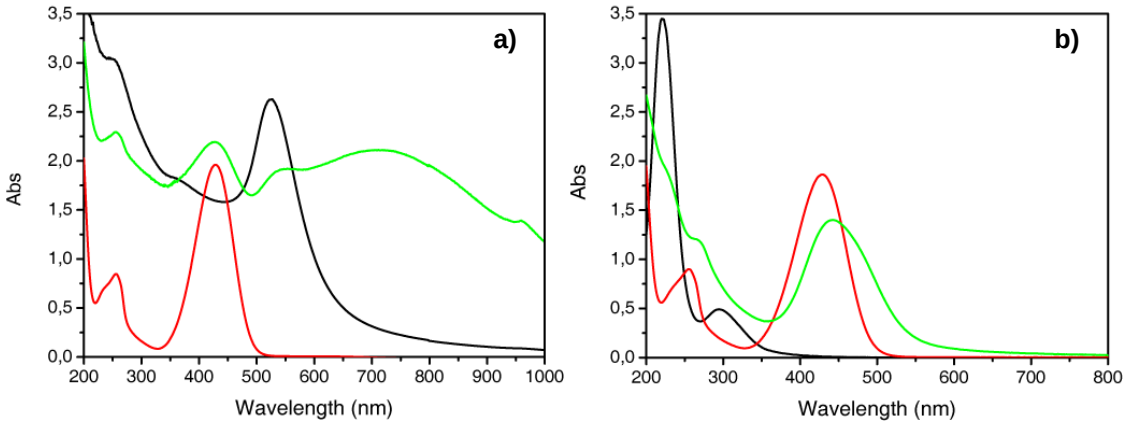

Figure 5.2: a) UV-visible absorption spectra of: nude NPs (black trace), PEP-C12-SH in water (red trace), PEP-C12 functionalized NPs (green trace). b) UV- visible absorption spectra of: $HAuCl_4$ (black trace), PEP-C12-SH (red trace), PEP-C12 and $HAuCl_4$ after mixing (green trace).

In Figure 5.2a, the UV-visible absorption spectra of NPs before and after functionalization with PEP-C12-SH are shown. NPs were purified from the dye excess by centrifugation and the precipitate collected and dissolved in water. The NPs are characterized by a plasmon band at 527 nm whereas PEP-C12-SH in water presents an absorption band at 428 nm (in ethanol the band is red shifted to 450 nm). The UV visible spectrum of functionalized NPs is not the simple sum of the two spectra, but it is broad and presents three peaks: at 428 the one associated to PEP-C12, at 544 and 720 nm two plasmon bands due to aggregation. According to the Electrical Double Layer theory (Chap. 3), the positive charge on the pyridine ring reduces the thickness of the protective double layer before the dye attaches on the NPs surface and so NPs aggregate.

In Figure 5.2b, we demonstrate chemical degradation of PEP-C12-SH because of the reaction with $HAuCl_4$ (prior to adding $NaBH_4$ as reductant). $HAuCl_4$ in water is characterized by two peaks at 220 and 294 nm. After mixing with PEP-C12-SH, the two peaks disappear and the dye band broadens and shifts to 442 nm.

Considering these results, we ruled out the possibility to functionalize gold NPs with PEP-C12-SH.

5.1.1.2. Gold nanoparticles functionalized with spiropyran in toluene

In Figure 5.3, the UV-visible absorption spectra of closed and open form of spiropyran in toluene and methanol are shown. Spiropyran ring aperture is obtained by illuminating the sample solution with a common tungsten lamp. In toluene (Figure 5.3a), spiropyran closed form is more stable, due to the low solvent polarity. It presents a peak at 334 nm. When it is illuminated for 5 minutes, a weak peak appears at 602 nm which is characteristic of the open merocyanine form (inset in Figure 5.3a). The peak disappear very quickly when the illumination is turned off.

In methanol (Figure 5.3b), the merocyanine form is promoted, due to the solvent polarity. The peak at 334 nm red shifts to 338 nm and a new peak at 533 nm, the one associated to the open form, emerges without illumination. When the solution is illuminated for 20 minutes, the peak at 533 nm slightly increases but less than in toluene, indicating that most of the dye is present, in methanol, in the merocynine form also without illumination (inset in Figure 5.3b).

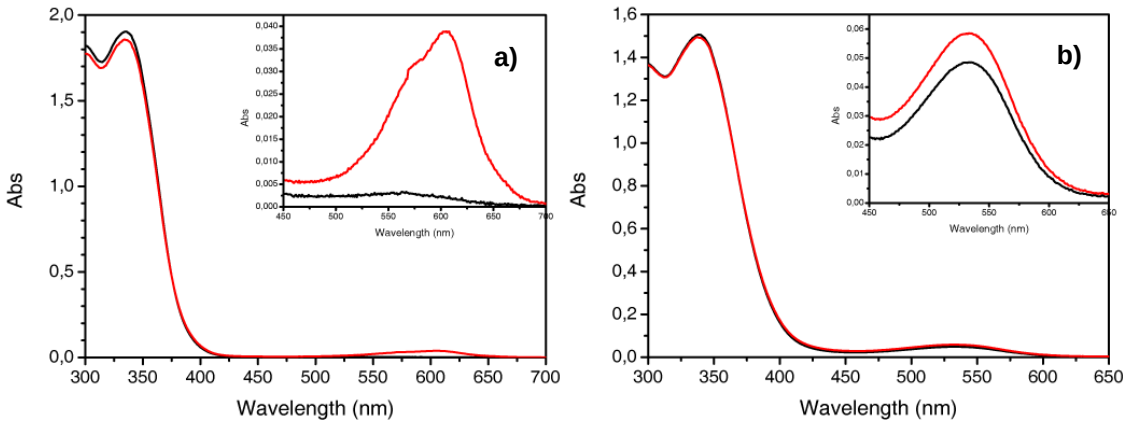

Figure 5.3: UV-visible absorption spectra of spiropyran-merocyanine forms: a) in toluene (black trace) and after illumination with a lamp for 5 minutes (red trace); b) in methanol (black trace) and after illumination with a lamp for 20 minutes (red trace). In the inset, a detail of the peak associated to the merocyanine form.

In Figure 5.4, the UV-visible absorption spectra of NPs before and after functionalization with spiropyran are shown.

Dodecanethiol stabilized NPs are characterized by a plasmon band at 508 nm. When NPs are mixed with spiropyran, the plasmon band slightly red shifts to 512 nm and broadens due to a change in dielectric constant of the medium. After purification, the spiropyran absorption peak at 334 nm is visible, confirming the NPs functionalization.

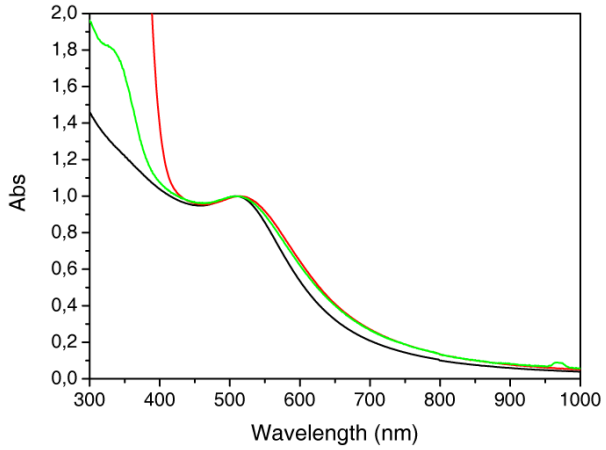

Figure 5.4: UV-visible absorption spectra of: nude NPs (black trace), NPs with spiropyran excess (red trace) and purified (green trace).

5.1.2 Gold nanorods

Gold NRs synthesized in water, due to their asymmetric structure, present two plasmon bands. One, at 520 nm, arises from the electrons coherent oscillation along the short axis (transverse mode) and it is equivalent to the plasmon oscillation in a spherical particle of the same size. The second band arises from the electrons coherent oscillation along the long axis (longitudinal mode). The longitudinal plasmon wavelength is strongly tunable and it red shifts on increasing the rod length.

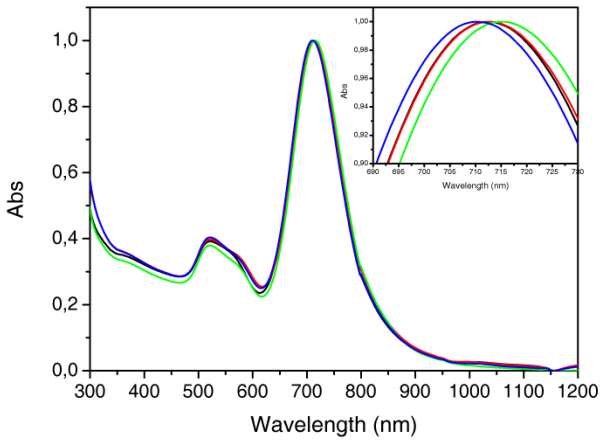

Figure 5.5: UV-visible normalized absorption spectra of NRs prepared in the same conditions but in different batches.

In Figures 5.5 and 5.6, the normalized UV-visible spectra of NRs in water are shown to determine the synthesis reproducibility and the stability of the NRs. The seeded growth of Au nanorods is a convenient synthesis with respect to both yield and uniformity. However,

it must be noted that the resonance wavelength of NRs produced with the same reagents ratio, after a time interval, varies from batch to batch and appears to be quite sensitive to nucleation and stirring conditions. We have observed that nanorod batches, prepared and isolated under apparently identical conditions, can differ in their optical resonances by 2-20 nm (Figure 5.5).

Moreover, the longitudinal plasmon resonance drifts toward shorter wavelengths by as much as 50 nm over a period of hours to days. For example, freshly synthesized NRs presents a longitudinal plasmon band at 707 nm and a transverse one at 520 nm (Figure 5.6a). After three months, the plasmon shifts to 673 nm. The blue shift of the longitudinal plasmon band reaches a plateau in three months (Figure 5.6b).

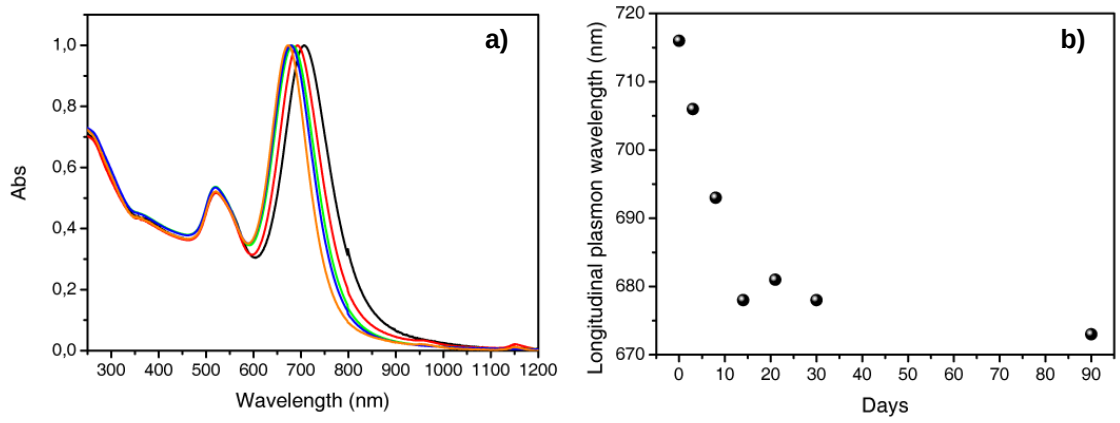

Figure 5.6: a) UV-visible normalized absorption spectra of NRs over a period of three month (black t = 0; red t = 8 days, green t = 21 days, blue t = 30 days, orange t = 3 months); b) longitudinal plasmon maximum wavelength as a function of time.

A likely explanation for this evolution was given by Zweilfel at al.[8] They considered that the unreacted Au ions were not freely dispersed in solution but were adsorbed instead onto the surfaces of CTAB micelles. For this reason, also in samples purified from the reaction solution, this effect is still observable. Gold ions, trapped in CTAB micelles, reduce on the nanorods surface modifying the structure.

After transfer in toluene using dodecanethiol (DDT), the UV-visible absorption spectrum of NRs modifies again (Figure 5.7). When NRs are suspended in dodecanethiol, we observe weakening of the longitudinal plasmon absorption peak. In addition, a red shift and broadening of about 150 nm in the absorption band can also be seen (red trace in Figure 5.7).

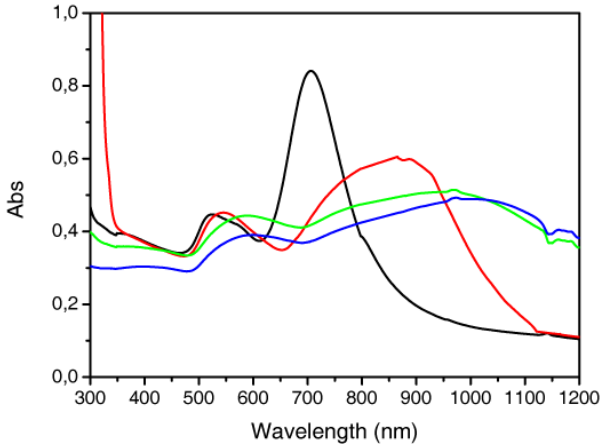

Figure 5.7: UV-visible absorption spectra of NRs in water (black trace), DDT-NRs in toluene (red trace), DDT-NRs in toluene purified from dodecanethiol excess (green trace), DDT-NRs in toluene purified from dodecanethiol excess after 12 hours (blu trace).

Earlier studies of interaction of gold particles with thiols have established the response of plasmon absorption to surface modifications.[7] Despite the broadening effect and red shift in the absorption, both longitudinal and transverse plasmon absorption features are retained, confirming the absence of dramatic morphological changes upon their binding to dodecanethiol. After purification, a further broadening of the plasmon band is visible, due to aggregation of NRs. NRs are still stable after 12 hours.

5.1.2.1. Gold nanorods functionalized with PEP-C3-SH and PEP-C12-SH in water

In Figure 5.8, UV-visible spectra of NRs functionalized with PEP-C3-SH and PEP-C12-SH in water are shown and compared with the spectra of nude NRs and PEP-C3-SH and PEP-C12-SH in water. PEP-C3-SH in water presents a peak at 431 nm instead for PEP-C12-SH the maximum absorption is slightly blue shifted at 428 nm, indicating a dependence on the aliphatic chain length. NRs are characterized by two bands, the transverse plasmon at 529 nm and the longitudinal one at 678 nm.

The appearance of the 427 - 430 nm bands confirms the binding of the two dyes to the gold nanorods. After NRs functionalization with both molecules, the longitudinal plasmon resonance changes. NRs with PEP-C3-SH and PEP-C12-SH present a red shift and broadening of both transverse and longitudinal plasmon band. The latter shifts to 784 nm for NRs with PEP-C3-SH and to 774 nm for the others. Despite the apparent retention of both longitudinal and transverse features, TEM analysis (Chap. 4) confirmed the presence of morphological changes upon the dyes binding, especially for NRs functionalized with

PEP-C3-SH. Moreover, the spectra of PEP functionalized NRs are quite similar to the spectrum of PEP-C12-SH functionalized NPs (Figure 5.2a). Probably the red shifted peak should not be univocally associated to longitudinal mode but it is due to aggregation of reshaped and shortened NRs, after functionalization and stabilization with charge molecules.

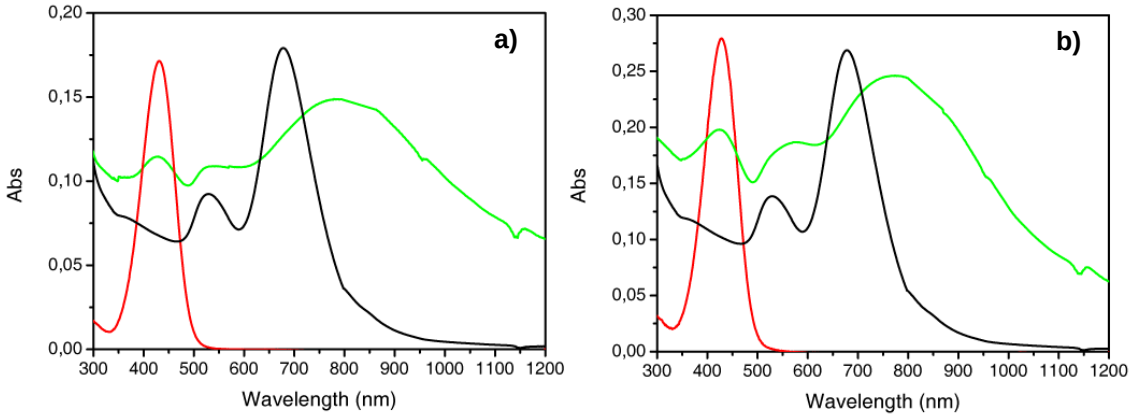

Figure 5.8: a) UV-visible absorption spectra of nude NRs in water (black trace), PEP-C3 (red trace) and PEP-C3 functionalized NRs (green trace); b) UV-visible absorption spectra of nude NRs in water (black trace), PEP-C12 (red trace) and PEP-C12 functionalized NRs (green trace).

5.1.2.2. Gold nanorods functionalized with spiropyran in toluene

In Figure 5.9, the UV-visible spectrum of NRs functionalized with spiropyran in toluene is shown and compared with the spectra of DDT functionalized NRs and spiropyran in toluene.

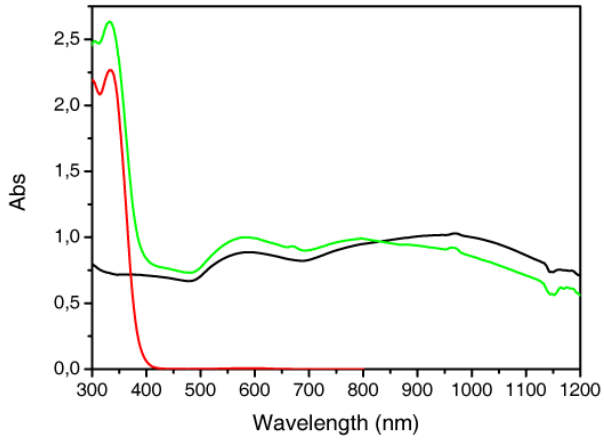

Figure 5.9: UV-visible absorption spectra of DDT functionalized NRs (black trace), spiropyran in toluene (red trace) and spiropyran functionalized NRs (green trace).

Spiropyran presents a band at 335 nm and NRs are characterized by two bands, the transverse plasmon at 590 nm and the longitudinal one at 980 nm. Both plasmon band are red shifted and damped compared with the UV-visible spectrum of NRs in water, as previously reported.

After functionalization with spiropyran and purification from dye excess, the appearance of the 334 nm band confirms the binding of spiropyran to gold nanorods. The binding of spiropyran affects the plasmon absorption band. The characteristic transverse and longitudinal plasmon absorption bands of rods are both red shifted. The former shifts to 581 nm, the latter to 800 nm. These changes are due to the longitudinal band sensitivity to surface interactions and morphological changes.

5.1.3 Gold nanoshells

Gold NSs synthesized in water possess a plasmon band which is tunable anywhere across the visible or infrared regions of the spectrum simply by adjusting the relative size of the dielectric core and the thickness of the gold overlayer. Depending on the particle size, further bands, due to the presence of surface plasmon multipolar resonances, should emerge.

Different size NSs were prepared varying both in core radius and shell thickness. We synthesized silica NPs with three core radii (R_1): 50 ± 10 nm; 95 ± 15 nm and 158 ± 30 nm. The gold shell thickness, instead, varies between 10 and 50 nm.

In Figure 5.10, we show the UV-visible absorption spectra of NSs with an inner radius of 50 nm and shell thickness varying between 0 and 50 nm. By varying the ratio between the gold ions growth solution and the amount of gold-decorated silica particles, we achieved different shell thickness.

All the spectra in Figure 5.10a are characterized by a broad plasmon peak with a long shoulder at longer wavelength. As described previously,[9,10] the peak broadening of the spectra can arise from: (1) the polydispersity of the core particles,[3] (2) the roughness of the shell surfaces, (3) the presence of particles with incomplete shells,[11] (4) the overlap of multipole surface plasmon resonances (e.g., quadrupole and octupole) arising from the large NS particles, (5) particle aggregation.

The position of the plasmon band maximum depends on the shell thickness and thereby on the amount of gold-decorated silica nanoparticles used in the preparation. As shown in Figure 5.10b, the plasmon wavelength red shifts linearly by increasing the particles

concentration till the amount of gold ions in solution is not enough to cover completely the core surface. In this case, the plasmon band shifts to shorter wavelength, resembling the plasmon band of gold nanoparticles or of nanoparticle aggregates.

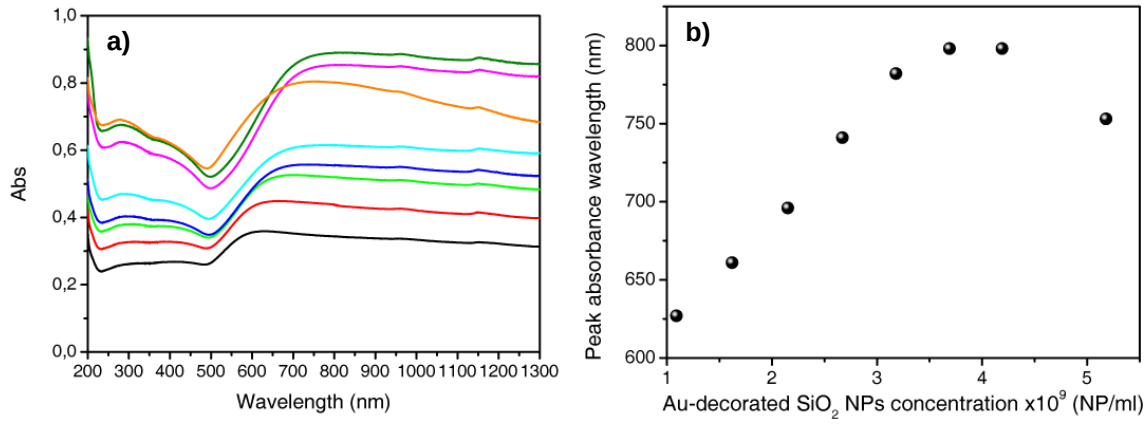

Figure 5.10: a) UV-visible absorption spectra of NSs with a inner radius of 50 nm and shell thickness varying between 0 and 50 nm; b) dependence of the plasmon band maximum wavelength on the concentration of gold-decorated silica nanoparticles concentration.

The plasmon resonance wavelengths of the NSs with inner radius of 50 nm are tunable over about 150 nm but larger diameter nanoshells are significantly more tunable.[3]

In Figure 5.11, the extinction spectra of NSs with 95 (a) and 158 nm (b) inner radius and different shell thickness are shown.

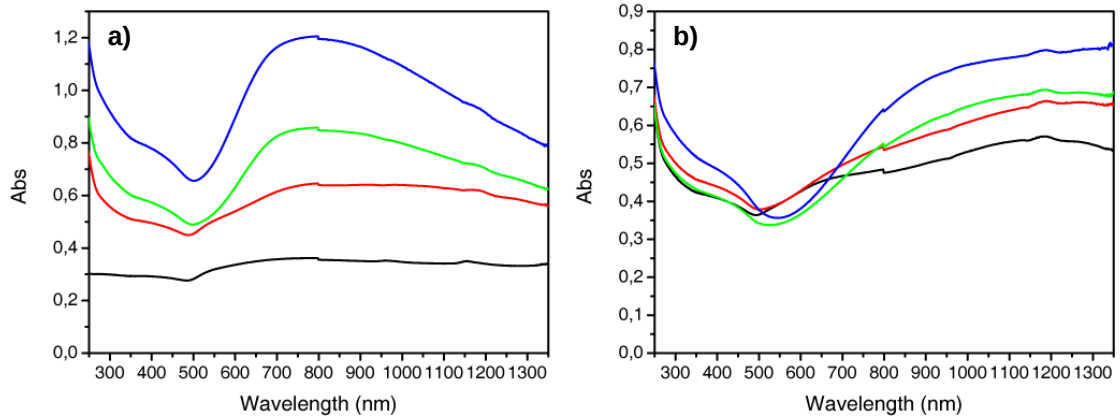

Figure 5.11: a) UV-visible absorption spectra of NSs with a inner radius of 95 nm and shell thickness of 43 nm (black trace), 27 nm (red trace), 14 nm (green trace), 2 nm (blue trace); b) UV-visible absorption spectra of NSs with a inner radius of 158 nm and shell thickness of 40 nm (black trace), 17 nm (red trace), 14 nm (green trace), 13 nm (blue trace).

It is difficult to completely appreciate the plasmon red shift with increasing core radius because the spectra are very broad. Considering the morphological characterization shown in Chap. 4 and the models used in the literature to described plasmon resonance for core-shell structures,[1,12] it is clear that NSs with an incomplete coverage full of apexes do not possess a narrow band and their extinction spectra should not be predicted by these models.

When we deposited NSs on functionalized glass slides, the UV-visible spectra of the particles slightly modify, depending on the level of organization of NSs on the substrates. In Figure 5.12, we show extinction spectra of different NSs in solution and deposited on the substrate. One sample presents an inner and outer radius of 50 and 60 nm, with not spherical shape and an irregular shell. The surface morphology appears similar to the one shown in Figure 4.5a, Chap. 4. The other NSs are 110 nm in size, with a core radius of 95 nm and a homogeneous size distribution (like Figure 4.5c, Chap. 4).

Irregular NSs (black trace in Figure 5.12 a and b) present the same broad extinction spectrum in solution and after deposition, due to a random aggregation present both in solution and in solid state. Instead larger and homogeneous particles aggregate in a different way when they are deposited on the substrate. In fact, the peak at 714 nm blue shifts to 685 nm and the broad shoulder extends to longer wavelengths.

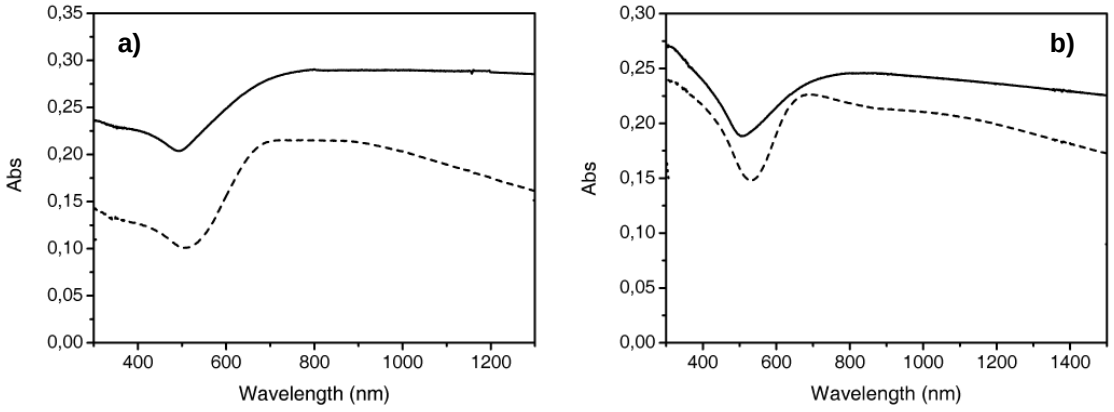

Figure 5.12: a) UV-visible absorption spectra of NSs with an inner and outer radius of 50 and 60 nm, respectively (black trace) and 95 and 110 nm (red trace) a) in water b) deposited on glass substrates.

As described in Chap. 4, the surface morphology of single particle influences the NSs aggregation. Particles covered by an irregular shell aggregate randomly, instead, more regular particles self-assemble in a hexagonal close-packed structure. As reported in the

literature,[13,14] the plasmonic properties are strongly dependent on interparticle interactions. In fact, in aggregates, the oscillating electrons in one particle feel the electric field due to the oscillation of the free electrons in a second particle, which can lead to a collective plasmon oscillation of the aggregated system. The coupled-particle SPR occurs at a frequency that is shifted from the single-particle localized SPR frequency. For example, the aggregation of gold nanoparticles in water results in a red-shift of the plasmon extinction wavelength maximum from that of isolated gold nanoparticle, as also evidenced by a visual color change from red to purple. The frequency and intensity of the assembly-induced plasmon shift depends on the degree of aggregation as well as the orientation of the individual particles within the aggregate. Park et al[15] observed a red or blue shift of the longitudinal plasmon resonance in nanorods end to end or side by side assembly, respectively.

5.1.3.1 Gold nanoshells functionalized with PEP-C3-SH and PEP-C12-SH in water

In Figure 5.13, the UV-visible spectra of NSs functionalized with PEP-C3-SH and PEP-C12-SH in water are shown and compared with the spectra of nude NSs and PEP-C3-SH and PEP-C12-SH in water. PEP-C3-SH in water presents a peak at 430 nm instead for PEP-C12-SH the maximum absorption is slightly blue shifted at 428 nm.

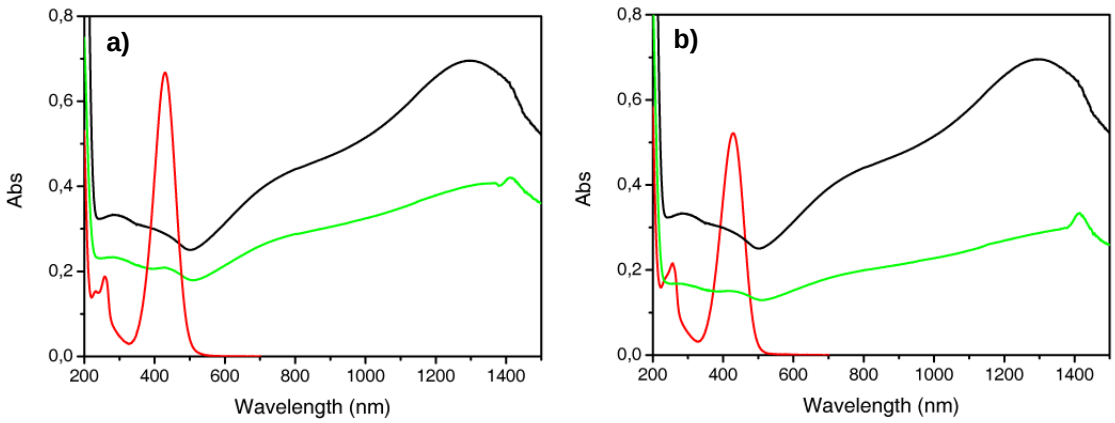

Figure 5.13: a) UV-visible absorption spectra of NSs in water (black trace), PEP-C3 (red trace) and PEP-C3 functionalized NSs (green trace); b) UV-visible absorption spectra of NSs in water (black trace), PEP-C12 (red trace) and PEP-C12 functionalized NSs (green trace).

NSs are characterized by a band at 1300 nm and a small shoulder at about 780 nm. The plasmon band is narrower and well defined compared with the spectra shown previously and it better matches theoretical predictions developed for nanoshell of similar size

(Figure 5.14). It is possible clearly assign the peak at 1300 nm to the dipolar plasmon band and the shoulder at 780 nm to the quadrupolar oscillations, which are present in larger nanoshells.

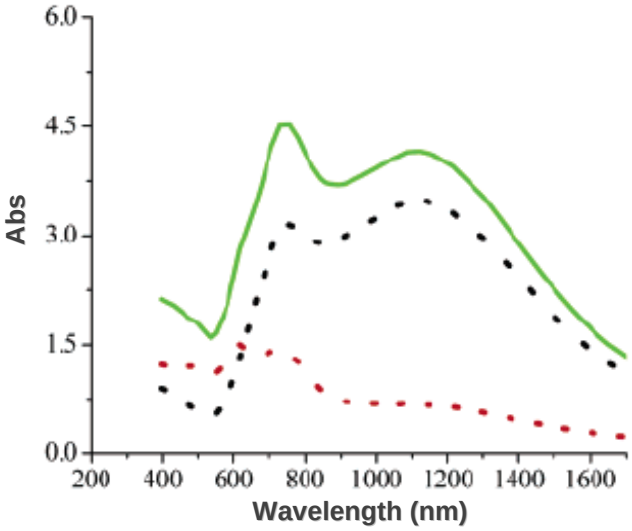

Figure 5.14: calculated spectra of the efficiency of absorption (red dashed), scattering (black dashed) and extinction (green solid) for NSs with dimensions R_1 = 120 nm and R_2 = 140 nm (adapted from ref. 16).

The appearance of a very small shoulder at 427-430 nm confirms the binding of the two dyes to the gold nanoshells. After NSs functionalization with both molecules, the NSs become less stable in water and the plasmon resonance broadens and damps.

5.1.3.2 Gold nanoshells functionalized with Rhodamine B in water

In Figure 5.15, the UV-visible spectra of NSs functionalized with Rhodamine B (RhB) in water are shown and compared with the spectra of nude NSs and RhB in water.

RhB in water presents a peak at 553 nm. NSs are characterized by a band at 1300 nm and a small shoulder at about 780 nm. After functionalization, NSs are stable, compared with NSs functionalized with PEP but in the spectrum of NSs functionalized with the dye, there is no clear evidence of Rhodamine B.

This is simply understood considering the concentration of gold nanoshells and how many molecules should bind to the particles surface.[17]

The concentration of NSs is C_{NS}~10^9 NP/ml.

The surface area of one NS $SA_{NS} = 4\pi R_2^2$ =2×10^{-13} m^2.

The diameter of a Rhodamine B molecule is approximately 1 nm.

The surface area of one molecule of RhB is $SA_{RhB} = 4\pi R^2$ =3×10^{-18} m^2.

The number of RhB molecules for NSs is SA_{NS}/SA_{RhB}~ 40000 molecules for NSs.

Total concentration of RhB molecules $C_{NS} \times \frac{SA_{NS}}{SA_{RhB}}/N_A$ ~10^{-7} M.

Considering that the absorption molar coefficient of RhB in water is ε = 90400 $M^{-1}cm^{-1}$, for the Lambert-Beer relation we should measure an absorbance of about 10^{-3}, which is under the detection limit.

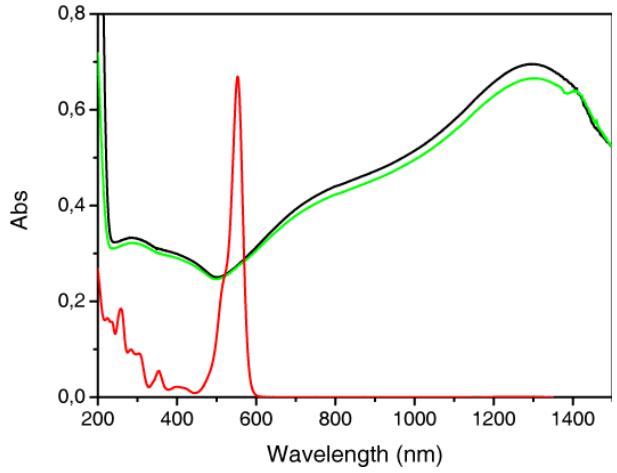

Figure 5.15: UV-visible absorption spectra of NSs in water (black trace), RhB (red trace) and RhB functionalized NSs (green trace).

5.2 Fluorescence

Photoluminescence from bulk gold was first observed by Mooradian.[18] It was found that the emission peak was centred near the interband absorption edge of the metal and therefore was attributed to direct radiative recombination of the excited electrons in the sp band with the holes in the d band. However, the quantum efficiency of the photoluminescence from bulk noble metals is very low, typically of the order of 10^{-10}.

The luminescence was found to be enhanced by several orders of magnitude on rough metal surfaces and on gratings.[19] The rough metal surface can be regarded as a collection of randomly oriented hemispheroids of nanometre size dimension on a smooth surface. These hemispheroids show a surface plasmon resonance and therefore the incoming and outgoing electric fields are amplified by the local field induced around the hemispheroids by the plasmon resonances.[1]

A similar enhancement has been found by El-Sayed group for the luminescence of gold nanorods[20] and by Wilcoxon et al[21] for very small spherical gold clusters (less than 5 nm). In both cases, the quantum yield is increased to 10^{-4}-10^{-5}.

Gold nanostructures should be defined as non luminescent even when compared with a slightly fluorescent molecule, So we consider that emission observed in our samples comes only from the dyes attached to the nanostructure.

The commonly used method to calculate the quantum yield, is by using the following expression:[22]

$$Q = Q_r \left(\frac{\mathrm{I}}{I_r}\right)\left(\frac{n^2}{n_r^2}\right)\left(\frac{OD_r}{OD}\right) \tag{5.1}$$

where Q is the quantum yield, *I* is the integrated intensity, *OD* is the optical density, and *n* is the refractive index. The subscript *r* refers to the reference fluorophore of known quantum yield. In this expression it is assumed that the sample and reference are excited at the same wavelength, so that it is not necessary to correct for the different excitation intensities of different wavelengths.

The problem in calculating quantum yields in this way is to define univocally the optical density of the dye bound to metallic nanostructure. In fact, at the excitation wavelength (375 nm), both PEP and NRs absorb, so we cannot assume a priori that a photon absorbed by NR will contribute to the emission of the dye bound to NR. For this reason, the quantum yield calculated from Eq. (5.1) may be overestimated or underestimated if we consider that all the photons adsorbed by the system PEP-NR or only photons absorbed by PEP, respectively, contribute to the emission of the dye.

We decided not to use the fluorescence quantum yield to verify an enhancement or quenching of emission by PEP bound to NRs. In the following sections, we show fluorescence spectra of PEP-C3 and PEP-C12 and we try to study the interaction between molecules and nanorods using fluorescence decay time.

5.2.1 Fluorescence spectra of PEP-C3-SH and PEP-C12-SH

PEP-C12 and PEP-C3 are not strongly fluorescent, as shown in Figure 5.16.

Emission spectra are obtained exciting at 375 nm and opening almost completely both the excitation and emission slits because of the low fluorescence signal. PEP-C3 and PEP-C12 maximum emission wavelength is 525 nm.

In Figure 5.17, emission and absorption spectra of functionalized NRs are shown. PEP bound to NRs is still less fluorescent comparing with the unbound dye but this is likely due to less concentrated solution. We recorded emission spectra exciting at 426nm (the maximum absorption wavelength) and opening almost completely both the excitation and emission slits.

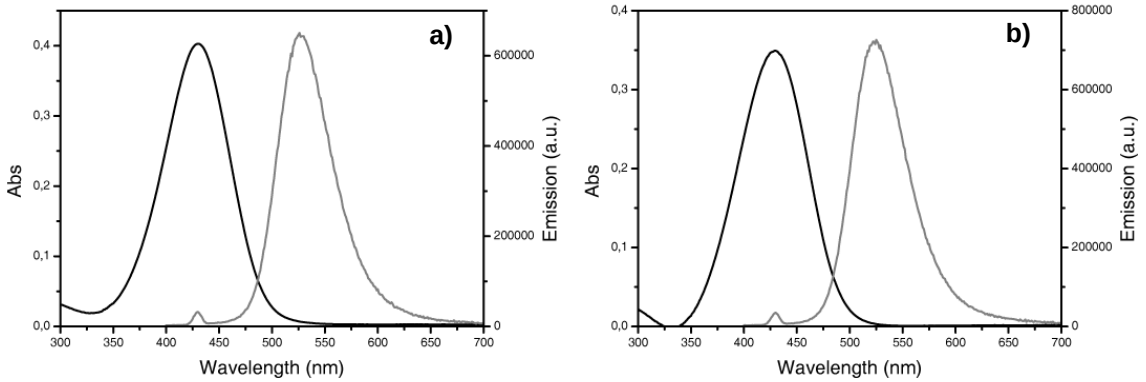

Figure 5.16: a) absorption (black trace) and emission (gray trace) spectrum of PEP-C3 in water; b) absorption (black trace) and emission (gray trace) spectrum of PEP-C12 in water (λ_{exc}=375 nm).

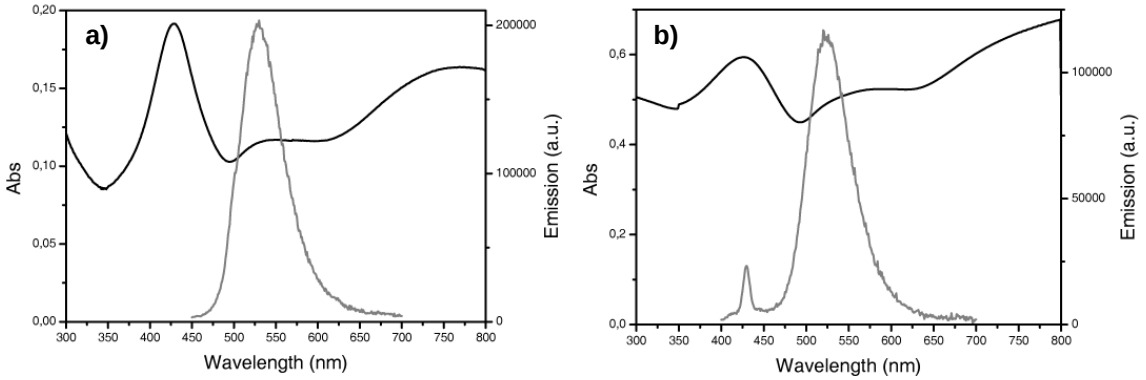

Figure 5.17: a) absorption (black trace) and emission (gray trace) spectrum of PEP-C3 bound to NRs in water; b) absorption (black trace) and emission (gray trace) spectrum of PEP-C12 bound to NRs in water (λ_{exc} = 426 nm).

5.2.2 Fluorescence decay times of PEP-C3-SH and PEP-C12-SH free and bound to nanorods

Fluorescence decay time measurements are performed with a Horiba Jobin Yvon spectrofluorometer (Model Fluorolog-321), using a laser diode at 375 nm wavelength, 80ps pulse duration and 1MHz repetition rate. Time decay longer than 400 ps can be detected. Fluorescence lifetime is measured with the time-correlated single-photon counting (TCSPC) method. TCSPC relies on the principle that the probability distribution for the emission of a single fluorescence photon is equivalent to the actual intensity versus time distribution for all photons emitted (Figure 5.18).[23] The experiment starts with the excitation pulse that excites the samples and sends a signal to the electronics. This signal is passed to a time-to-amplitude converter (TAC), which generates a voltage ramp that is a voltage that increases linearly with time on the nanosecond timescale. A second channel

detects the pulse from the single detected photon. The arrival time of the signal is accurately determined using a constant function discriminator (CFD), which sends a signal to stop the voltage ramp. The TAC now contains a voltage proportional to the time delay (Δt) between the excitation and emission signals. As needed, the voltage is amplified by a programmable gain amplifier (PGA) and converted to a numerical value by the analog-to-digital converter (ADC). To minimize false readings the signal is restricted to a given range of voltages. If the signal is not within this range the event is suppressed by a window discriminator (WD). The voltage is converted to a digital value that is stored as a single event with the measured time delay. A histogram of the decay is measured by repeating this process numerous times with a pulsed-light source.

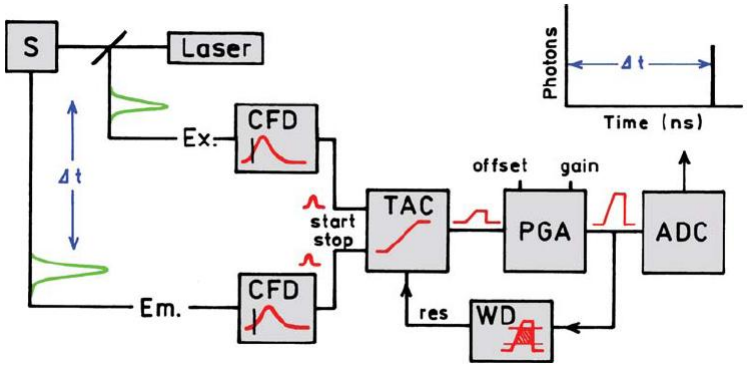

Figure 5.18: electronic schematic for TCSPC.[22]

In Figure 5.19, time decays of PEP-C3 and PEP-C12 are shown at different time ranges. As expected, the two dyes present the same dynamics, with two characteristic times: a short one of 6.2 ± 0.5 ns and a long one of 61 ± 2 ns.

When the dye is bound to NRs, the interaction between the molecules and the nanoparticles causes a change in the PEP dynamics (Figure 5.20). For example, PEP-C3 bound to NRs, decays faster. The shorter time reduces by 2 ns (τ = 4.0 ± 0.5 ns) instead the longer one remains unchanged. Nanorods quench PEP fluorescence activating other faster decay channels. Quenching and enhancement of dye fluorescence are well described in the literature.[24,25] A fluorophore in the excited state should be described as an oscillating dipole and can induce oscillations of the electrons in the metal.[22] The electric field created by the metal can interact with the excited fluorophore and alter its emission. This interaction is almost certainly bidirectional so that light-induced oscillations in the metal can affect the fluorophore. The interactions of fluorophores with metallic surfaces can have a number of useful effects, including increased/decreased quantum yields,

increased photostability, increased distances for resonance energy transfer, and decreased lifetimes.

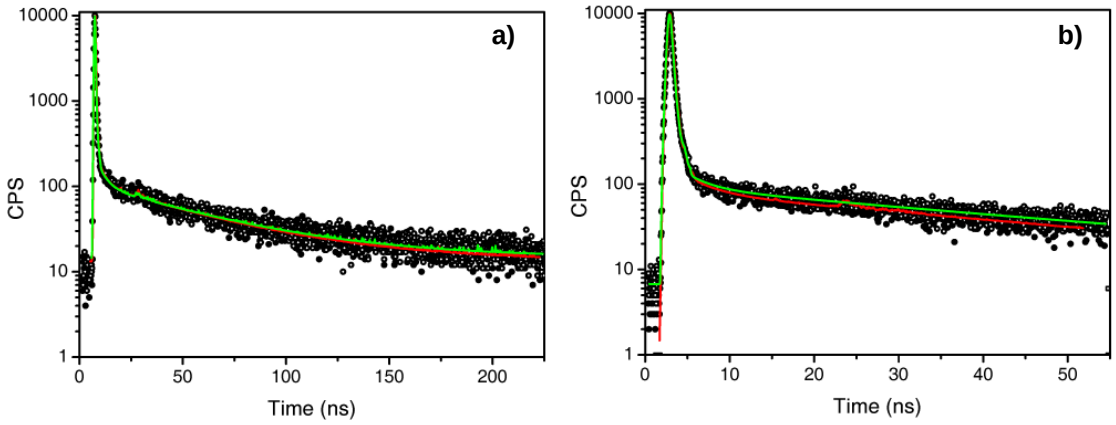

Figure 5.19: fluorescence time decay of PEP-C3 (black dot) and PEP-C12 (void dot) at a) 220 ns range time and b) 55 ns range time. Solid lines correspond to fitting.

The interaction between molecules and a metallic surface depends on the relative distance.[26] For a very short separation distance between the chromophore dipoles and the metal surface a substantial 'radiationless' de-excitation with a corresponding reduction of the radiative lifetime and the fluorescence intensity is found: the fluorescence is 'quenched', dissipating the excitation energy in the metal as heat, as shown for PEP-C3 bound to nanorods (Figure 5.20a). The aliphatic chain length (about 0.5 nm) is too short to avoid this kind of interaction.

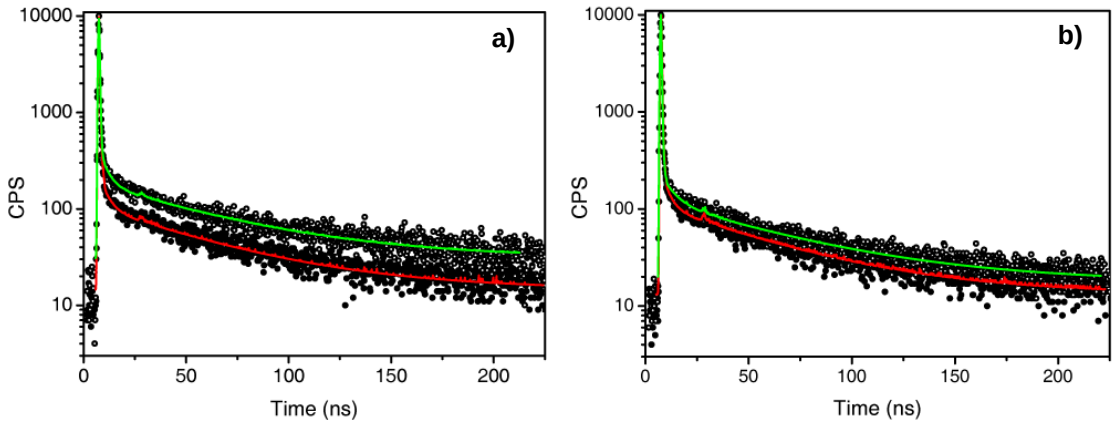

Figure 5.20: a) fluorescence time decays of PEP-C3(black dot) and PEP-C3 bound to NRs (void dot); b) fluorescence time decays of PEP-C12 (black dot) and PEP-C12 bound to NRs (void dot). Solid lines correspond to fitting: free dye (red line), bound dye (green line).

For intermediate separation distances the optically excited chromophores can effectively couple back to the plasmonic states of the metal substrate. An optimum separation distance for this resonance energy transfer was found to be ca. 4-20 nm.[27] Considering these distances, we can assume that an aliphatic chain composed of 12 carbon atoms (about 1.6 nm) is not long enough to prevent quenching of fluorescence. The decay time of PEP-C12 bound to nanorods is still faster ($\tau = 5.2 \pm 0.5$ ns) than the one of the free dye but it is less fast than PEP-C3. For larger separation distances, no immediate modification of the radiative emission of the excited state of the chromophore exists anymore.

References

(1) Link, S.; El-Sayed, M. A. *Int. Revews in Physical Chemistry* **2000**, *19*, 409-453.

(2) Muskens, O. L.; Bachelier, G.; Del Fatti, N.; Vallée, F.; Brioude, A.; Jiang, X.; Pileni, M. P. *J. Phys. Chem. C* **2008**, *112*, 8917-8921.

(3) Rasch, M. R.; Sokolov, K. V.; Korgel, B. A. *Langmuir* **2009**, *25*, 11777-11785.

(4) Oldenburg, S. J.; Jackson, J. B.; Westcott, S. L.; Halas, N. J. *Appl. Phys. Lett.* **1999**, *75*, 2897-2899.

(5) Kim, T.; Lee, K.; Gong, M.; Joo, S. W. *Langmuir* **2005**, *21*, 9524-9528.

(6) Personn, B. N. J. *Surf. Sci.* **1993**, *281*, 153-162.

(7) Linnert, T.; Mulvaney, P.; Henglein, A. *J. Phys. Chem.* **1993**, *97*, 679-682.

(8) Zweifel, D. A.; Wei, A. *Chem. Mater.* **2005**, *17*, 4256-4261.

(9) Kim, J. H.; Bryan, W. W.; Randall Lee, T. *Langmuir* **2008**, *24*, 11147-11152.

(10) Kundu, J.; Le, F.; Nordlander, P.; Halas, N. J. *Chemical Physics Letters* **2008**, *452*, 115-119.

(11) Prasad, V.; Mikhailovsky, A.; Zasadzinski, J. A. *Langmuir* **2005**, *21*, 7528-7532.

(12) Wang, H.; Brandl, D. W.; Nordlander, P.; Halas, N. J. *Acc. Chem. Res.* **2007**, *40*, 53-62.

(13) Link, S.; El-Sayed, M. A. *J. Phys. Chem. B* **1999**, *103*, 8410-8426.

(14) Jain, P. K.; Huang, W.; El-Sayed, M. A. *Nano Lett.* **2007**, *7*, 2080-2088.

(15) Park, H. S.; Agarwal, A.; Kotov, N. A.; Lavrentovich, O. D. *Langmuir* **2008**, *24*, 13833-13837.

(16) Jain, P. K.; Lee, K. S.; El-Sayed, I. H.; El-Sayed, M. A. *J. Phys. Chem. B* **2006**, *110*, 7238-7248.

(17) Bardhan, R.; Grady, N. K.; Cole, G. R.; Joshi, A.; Halas, N. J. *ACS Nano* **2009**, *3*, 744-752.

(18) Mooradian , A. *Phys. Rev. Lett.* **1969**, *22*, 185-187.

(19) Raether, H. In *Surface Plasmons on Smooth and Rough Surfaces and on Gratings;* Springer-Verlag: 1986; .

(20) Mohamed, M. B.; Volkov, V.; Link, S.; El-Sayed, M. A. *Chem. Phys. Lett.* **2000**, *317*, 517-523.

(21) Wilcoxon, J. P.; Martin, J. E.; Parsapour, F.; Wiedenman, B.; Kelley, D. F. *J Chem. Phys.* **1998**, *108*, 9137.

(22) Lakowicz, J. R. In *Principles of Fluorescence Spectroscopy;* Springer: 2006; .

(23) Anonymous In *Data Station Hub: User Guide;* Horiba Jobin Yvon: 2004; .

(24) Kamat, P. V. *J. Phys. Chem. B* **2002**, *106*, 7729-7744.

(25) Thomas, K. G.; Kamat, P. V. *Acc. Chem. Res.* **2003**, *36*, 888-898.

(26) Liebermann, T.; Knoll, W. *Colloids and Surfaces A: Physicochem. Eng. Aspects* **2000**, *171*, 115-130.

(27) Tam, F.; Goodrich, G. P.; Johnson, B. R.; Halas, N. J. *Nano Lett.* **2007**, *7*, 496-501.

CHAPTER 6

Nonlinear optical properties of gold nanostructures

In this chapter, the nonlinear (NL) optical properties of nude and functionalized gold nanostructures are described. Z-scan technique is used to characterize nonlinear absorption of nude nanorods (NRs) and nanoshells (NSs). Pump and Probe method and Surface Enhanced Raman Spectroscopy (SERS) are used to study the interaction between molecules and nanoshells.

6.1 Laser system

Z-scan and Pump and Probe experiments are performed with a femtosecond amplified laser system by Spectra Physics. It comprises a Titanium-Sapphire oscillator (*Tsunami*) pumped by the second harmonic of a Nd:YVO_4 laser (*Millennia*) and amplified by a regenerative optical amplifier (*Spitfire*) pumped by the second harmonic of a Q-switched Nd:YLF laser (*Merlin*). The laser beam from the oscillator is a train of femtosecond pulses at 82 MHz repetition rate, each of approximately 80 fs duration and energy of few nJ. The oscillator is tunable within the range 750-840 nm but in all experiments the wavelength is set at 806 nm. The pulses are subsequently amplified inside the Spitfire, whose

performance is based upon the Chirped Pulse Amplification. The pulses entering the amplifier are first stretched in time, then undergo amplification up to almost 100.000 times and finally are sent to the compressor which restores the initial temporal duration. The output pulses of the laser system have the following features: wavelength of 806 nm with 10 nm bandwidth, repetition rate ranging from 1 Hz to 1 kHz, average time duration of 150 fs and energy for single pulse in the order of 1 mJ.

During the experimental measurements, the beam properties – time duration, energy and beam waist – were periodically verified. In particular, the time duration is determined by means of an external autocorrelation experiment in a BBO crystal, the energy content is sampled with a pyroelectric detector (*Molectron J3-0,5m*) and the spatial shape of the beam is measured with a CCD camera *(Pulnix TM-7CN*).

6.2 Z-scan

Through the z-scan technique, it is possible to measure characteristic constants associated with NL optical phenomena (i.e. NL refractive index and NL absorption coefficient) simply measuring variations in transmittance. The method relies on the idea that these NL optical effects depend on the irradiance of the incident beam.[1]

With this technique it is possible to obtain the NL refractive index n^I_2 and the NL absorption coefficient β through the analysis of the dependence of the signal from the incident beam irradiance, which is continuously varied in a tight focus geometry as shown in Figure 6.1. In this configuration, a laser beam is focused by a lens (L1) of suitable focal length onto a sample mounted on a translation stage and reaches its maximum irradiance at the focus. The stage is moved around the focal region along the beam propagation direction (Z axis) from the side of the detector toward that of the focal lens (negative values of Z correspond to locations of the sample between the focusing lens and its focal plane, positive values correspond to the sample positioned between the detector and the focal plane). Starting the scan from a distance far away from the focus, the beam irradiance is low and nonlinear optical (NLO) effects are negligible; hence, the transmittance remains rather constant. As the sample is brought closer to the focus, the beam irradiance increases, leading to sizeable NLO phenomena. The experiment records the transmittance of the incident beam as a function of the sample position along the z direction of propagation of the focusing beam.

In the "closed aperture" method, a suitable aperture A is placed in the far field before the collecting lens L2, so that it is possible to detect variations in the intensity of the transmitted beam due to NL refraction as well as NL absorption phenomena. This method is commonly employed for the n_2^I measurement. In the "open aperture" method such aperture is not present and the whole transmitted beam is detected. Since in this way the variations of the beam transmittance derive from NL absorption effects, the open aperture method allows to measure β. If $\beta < 0$, open aperture z-scan will produce a peak-shaped curve, indicating photo-induced transparency due to saturable absorption whereas if $\beta > 0$, open z-scan will produce a valley-shaped curve, indicative of multiphoton absorption and/or reverse saturable absorption. In this work only measurements in the open aperture configuration were performed, so in the following treatment only this method will be described.

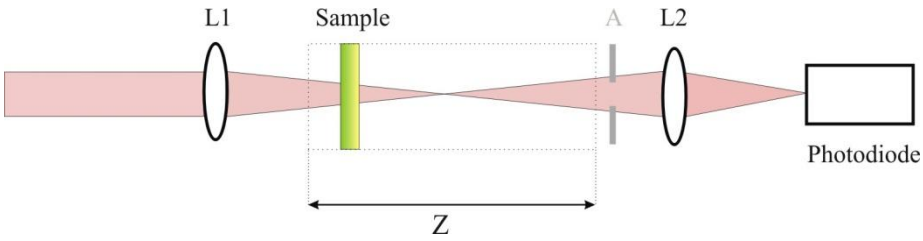

Figure 6.1: tight focus geometry in a z-scan experiment. L1, L2=convex lens, A=aperture (present only in the "closed aperture" configuration).[1]

6.2.1 Technique and fundamental relations of open aperture z-scan

The starting point to examine the propagation behaviour of an electric field in a nonlinear medium is Maxwell's equations.[2] For a dielectric non-magnetic medium, combination of the Maxwell's equations gives the following wave equation for the electric field in the time-domain:

$$\nabla \times \nabla \times E(\omega) = \frac{\omega^2}{c^2} E(\omega) - \omega^2 \mu_0 P(\omega) \qquad (6.1)$$

where $E(\omega)$ is the electric field and $P(\omega)$ is the total polarization (in terms of their Fourier transform), c is the light speed and μ_0 is free-space permeability.

If one assumes that:

(i) at frequency ω linear processes can be neglected and only third order phenomena contribute to NL response;

(ii) SVEA (*slowly-varying envelope approximation*) can be applied, so that the second derivative of the field can be neglected;

(iii) the incident field can be decomposed in monochromatic plane-waves travelling along *z* direction;

(iv) considering a single beam technique;

the differential equation describing the optical loss at frequency becomes:

$$\frac{\partial}{\partial z}E_1 = \frac{i\omega_1}{2cn_1}\cdot\chi^{(3)}(-\omega_1;\omega_1,-\omega_1,\omega_1)\cdot E_1\cdot|E_1|^2 \tag{6.2}$$

Furthermore, remembering that the intensity for a running wave with frequency ω_1 is:

$$I_1 = \frac{1}{2}\varepsilon_0 cn_1|E_1|^2 \tag{6.3}$$

Eq. 6.2 will give:

$$\frac{\partial}{\partial z}I_1 = -\beta I_1^2 \tag{6.4}$$

with the β as NL absorption coefficient.

In general, the z-scan response can be rigorously interpreted for any kind of beam by integrating Eq. 6.4 with suitable boundary conditions. However, for simplicity, further approximations are usually applied to obtain expressions that can be easily employed in the interpretation of the experimental data.

An usual assumption is that the laser beam has a Gaussian profile in time and space, the latter characterized by a beam waist w_0 in the focal plane along the z direction.

Moreover, if the sample length L is small enough that changes in the beam diameter within the sample due to diffraction or NL refraction are negligible, then the "thin" sample approximation can be applied. This implies that $L << z_0$, where z_0 is the diffraction length of the Gaussian beam.

Under these assumptions, the normalized transmittance after the sample is given by:

$$T(z) = \frac{1}{\sqrt{\pi}q_0(z)}\int_{-\infty}^{+\infty} d\tau\, ln[1+q_0(z)\cdot exp(-\tau^2)] \tag{6.5}$$

where

$$q_0(z) = \frac{\beta I_0 L_{eff}}{1+z^2/z_0^2}$$

β being the NL absorption coefficient, $L_{eff} = (1-e^{\alpha_0 L})/\alpha_0$ is the effective interaction length with the sample thickness of L, α_0 is the linear absorption coefficient, I_0 the peak irradiance in the focal plane,

In general, for a Gaussian beam profile in time and in space the irradiance is calculated by:

$$I(Wcm^{-2}) = \frac{2E(J)}{\pi^{3/2}w_t(s)w_0^2(cm^2)} \tag{6.6}$$

where $E(J)$ is the pulse energy, w_0 is the beam waist and w_t is the time parameter related to *FWHM* by the relation: $FWHM = 2\sqrt{ln2}w_t$.

If $|q_0| < 1$, the logarithm function in Eq. 6.5 can be expanded in a Taylor series and the result integrated term by term, giving (Sheik-Bahae model[2]):

$$T(z) = \sum_{m=0}^{\infty} \frac{[-q_0(z)]^m}{(m+1)^{3/2}} \tag{6.7}$$

Usually only few terms of the infinite sum need to be retained for an accurate result.

Although z-scan is a very simple technique, it presents some limitations in measuring NLO properties of metal nanoparticles and other materials in general. First of all, the absorption by the sample of a laser pulse train can cause heating of the sample. Thermal phenomena may mask electronic properties of the material since they can produce very intense nonlinearities. It is thus necessary to work with short pulses, for example femtosecond pulses instead of nanosecond ones, at low repetition rates to reduce thermal effects. The second limitation is due to the fact that the time scale of the experiment is set by the pulse duration. Transient phenomena that die out too quickly may at most reach a steady state that is too weak to detect. On the other hand, phenomena occurring on a time scale much longer than the pulse width do not have time to set in. Therefore, z-scan experiments provide an effective measurement of the NLO response dominated by phenomena occurring on the same time scale as the duration of the laser pulse employed.

6.2.2 Experimental set up of open aperture z-scan

In Figure 6.2, the experimental set up for open aperture z-scan experiments is shown.

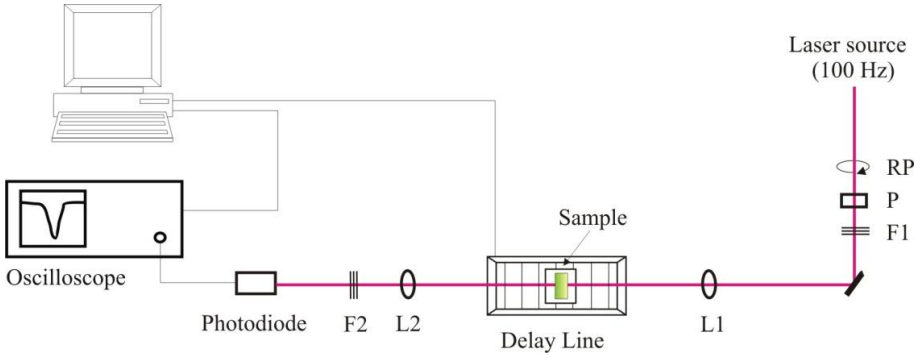

Figure 6.2: experimental set up for open aperture *z*-scan experiments. RP=half waveplate, P=polarizer, L1, L2=convex lens, F1, F2=neutral density filters.[1]

The beam wavelength is set at 806 nm and the repetition rate at 10, 20 or 200 Hz to avoid thermal effects in the sample. The linearly polarized laser beam is focused with a 200 mm focal length lens (L1) and the sample is moved across the focus by means of a 15 cm computer controlled micrometric translation stage (delay line, Newport M-ILS150cc). The beam waist at the focus was typically 22 ± 5μm. The pulse energy is suitably attenuated by means of neutral density filters (F1). For fine tuning of the input laser irradiance, an attenuating system formed by a half waveplate (RP) followed by a polarizer (P) is employed. The input pulse energy in the experiments shows typical values in the range 100-500 nJ. After the sample, the transmitted beam is recollected by a second lens (L2) and, after suitable attenuation (neutral density filters F2), it is detected by a Si photodiode. The signal is averaged by an oscilloscope and then processed by a PC acquisition program.

6.2.3 Z-scan measurements on metallic nanostructures

NL optical properties of noble metal NPs in solution[3-7] and embedded in a glass matrix[8-12] have been investigated by the open aperture z-scan technique because of their large third-order susceptibility and the ultrafast response times. In general, when excited near the SPR band, metal NPs behave as a saturable absorbers owing to the bleaching of the ground-state plasmon band. In some cases, at higher pump intensity, gold nanorods[3], platinum[5] and silver[10] NPs change their behavior from saturable absorber to reverse saturable absorber (i.e., absorption increases at high input intensities) due to free carrier absorption. Open aperture z-scan measurements can be performed either under one-photon resonant conditions or by shining light in a transparent region of the material. In the latter case, the data provide information on instantaneous two- or multi-photon absorption processes. Metal nanostructures have been excited by 532 nm nanosecond and picosecond laser pulses (gold, silver and platinum NPs) or 805 nm femtoseconds laser pulses (gold nanorods and twin linked gold NPs), depending on the SPR band wavelength. By fitting the experimental results, it is possible to obtain the NL absorption coefficient; the data obtained are strongly dependent on the experimental conditions (nature of the sample as well as pulse characteristics). Very different nonlinearity values are published for gold nanoparticles[6, 8, 10-12], from -10^{-2} cmW^{-1} for gold nanorods in a silica matrix excited by a 22 ns pulses at 532 nm[12], to -10^{-10} cmW^{-1} for gold nanoparticles in water excited by 30 ps

pulses at 532 nm[6]. For this reason, comparing NL absorption coefficient for different nanostructures should be meaningless when the experimental condition are not the same.

Nude nanorods (NRs) and nanoshells (NSs) are characterized by z-scan technique. For NRs there are some experiments reported in literature[3, 12] and so we dedicate only a small section. A more complete analysis is described for nanoshells, for which this is the first time that NLO properties have been investigated.

6.2.3.1 Z-scan measurements on gold nanorods

In the literature, different examples of z-scan measurements on nanorods, both in solution and glass matrix, are reported.[3, 12] We performed an experiment similar to the one presented by Helim et al[3] on NRs prepared in water and using a Ti-Sapphire laser as excitation source. The laser pulse, in this case, is at 806 nm wavelength (not completely resonant with the longitudinal plasmon which is located at 720 nm), with 150 fs duration and repetition rate of 20 and 200 Hz. As shown in Figure 6.3, NRs in solution behave as saturable absorbers at both 20 and 200 Hz repetition rate and in all the range of pulse energies employed. The amplitude of the saturation signal increases with energy but not with the repetition rate, excluding accumulation effects. However, a peculiar phenomenon is observed which has never been reported in the literature: the saturation peak is strongly asymmetric. The asymmetry is so strong that it is impossible to fit the data with the Sheik-Bahae model.

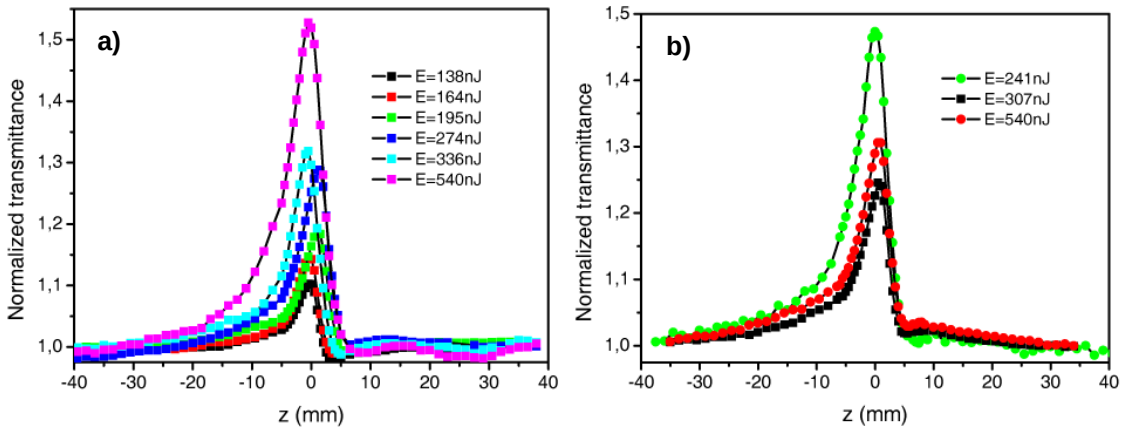

Figure 6.3: Open aperture z-scan measurements at a) 20 Hz and b) 200 Hz of NRs.

In Figure 6.4 the NLO response of NRs at the same energy (365 nJ) and reversing the direction of the stage motion along the beam (from positive to negative values of z or viceversa) is shown. The asymmetry reverts on approaching the focal plane either from the

side of the laser source or from that of the detector. This is a clear indication that a residual effect of NL refraction or NL scattering does not contribute to the phenomenon since it would be unaffected by the reversal of the stage motion.

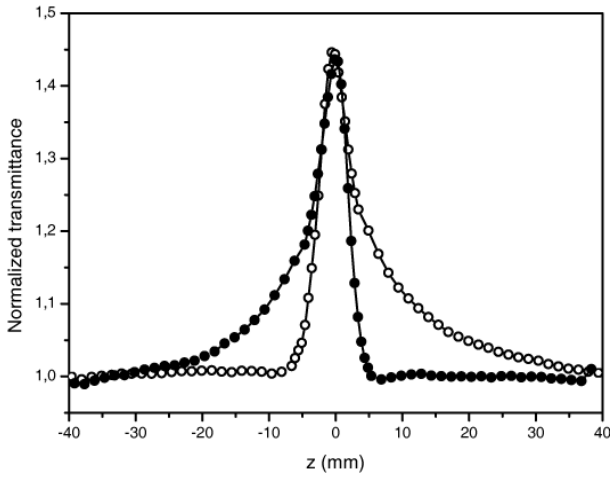

Figure 6.4: Open-aperture z-scan measurements of NRs at 20 Hz repetition rate and at 365 nJ with regular (black dot) and inverted (empty dot) translation stage motion.

The saturation peak asymmetry is due to a reshaping of the NRs under femtosecond illumination.[13] Time diffusion of NRs covered by CTAB in water is too long to constantly supply fresh nanoparticles into the illumination area, during z-scan measurement. As the sample approaches the focus and the intensity increases, gold nanorods reshape causing the nonlinear optical response changes because they have not enough time to diffuse out of the beam waist.

6.2.3.2 Z-scan measurements on gold nanoshells

Z-scan measurements are performed on gold NSs in solution and deposited on glass substrates with a 170 fs long pulses centered at 806 nm with a repetition rate of 20 or 200 Hz. Typical pulse energies, after suitable attenuation, were in the range 100-600 nJ. Two different size NSs are studied: with a inner and outer radius $R_1 = 50 \pm 10$ nm and $R_2 = 60 \pm 20$ nm; with a inner and outer radius $R_1 = 95 \pm 4$ nm, $R_2 = 110 \pm 4$ nm.

As shown in Figure 6.5, all the NSs in solution samples behave as saturable absorbers at both 20 and 200 Hz repetition rate and in all the range of pulse energies employed. The amplitude of the saturation signal increases with energy at both repetition rates. However, a peculiar phenomenon is observed on increasing energy and/or repetition rate: the saturation peak becomes increasingly asymmetric. The asymmetry is not so strong to

avoid to fit the data with the Sheik-Bahae model. Comparing the z-scan traces for the same samples at the same energies but at different repetition rates, saturation is larger at 200 Hz. This is probably due to thermal effects.

The NSs size influences the femtosecond laser pulse response. Although the UV-visible spectra are broad and it is quite difficult to locate a unique or a central wavelength of the surface plasmon resonance (see Chap. 5), the saturation is clearly enhanced for NSs with R_2 = 110 nm. For example, comparing, in figure 6.5, z-scan traces at the same pulse energy (210 nJ) and repetition rate (20 Hz) for NSs with R_2 = 60nm (black full square) and NSs with R_2 = 110 nm (green full triangle), saturation is 8% for the former and 20% for the latter even if the concentration of larger NSs is lower than the concentration of smaller ones.

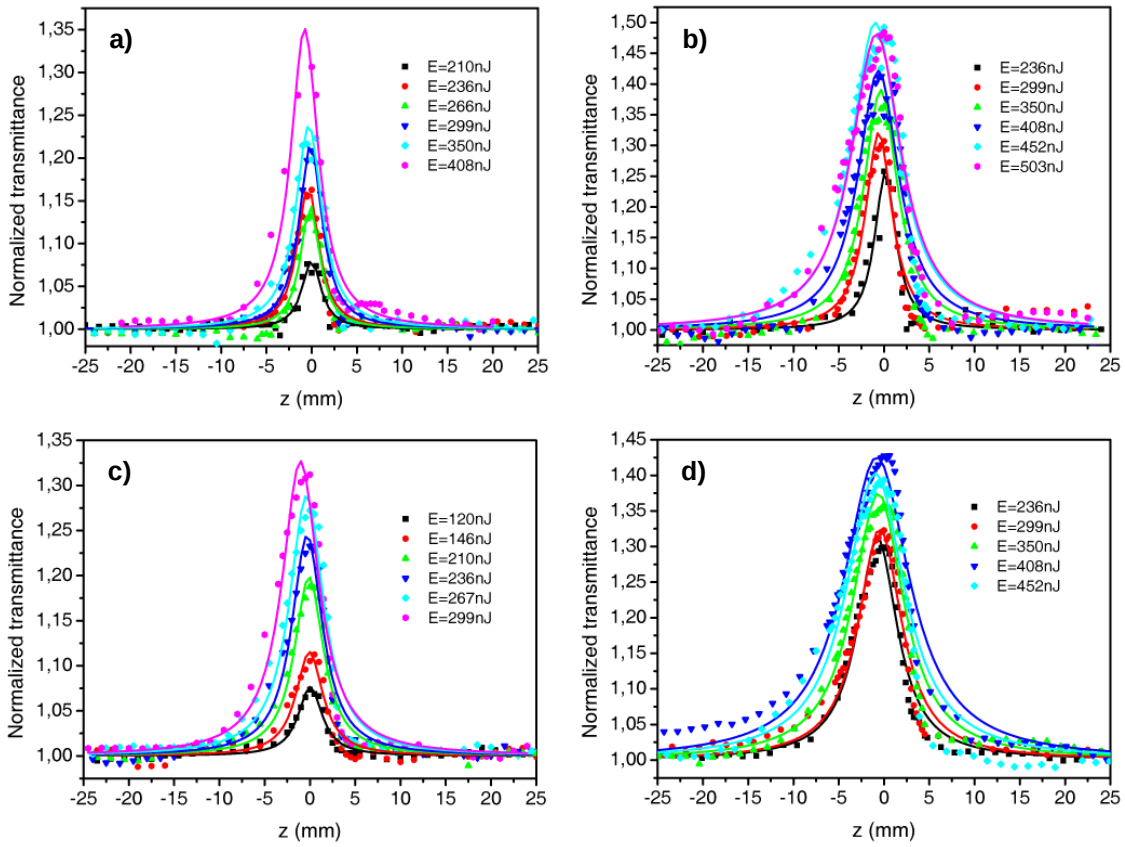

Figure 6.5: Open-aperture z-scan measurements at a) 20 Hz and b) 200 Hz repetition rate of the NSs R_2 = 60 nm in solution, c) 20 Hz and d) 200 Hz repetition rate of NSs R_2 = 110 nm in solution. The solid lines indicate theoretical fit.

The peak asymmetry is made evident by plotting the fit residues for NSs R_2 = 60 nm and R_2 = 110 nm at two energies and both repetition rates. The residues show a sigmoidal

trend, negative values are associated to calculated values greater than experimental data, and viceversa. Increasing energy causes an enlargement of the sigmoid and of the peak to peak difference at both the repetition rates.

In Figure 6.6, the NLO response of NSs R_2 = 110 nm at the same energy and reversing the direction of the stage motion along the beam (from positive to negative values of z or viceversa) is shown. The asymmetry reverts on approaching the focal plane either from the side of the laser source or from that of the detector. This is a clear indication that a residual effect of NL refraction or NL scattering does not contribute to the phenomenon since it would be unaffected by the reversal of the stage motion.

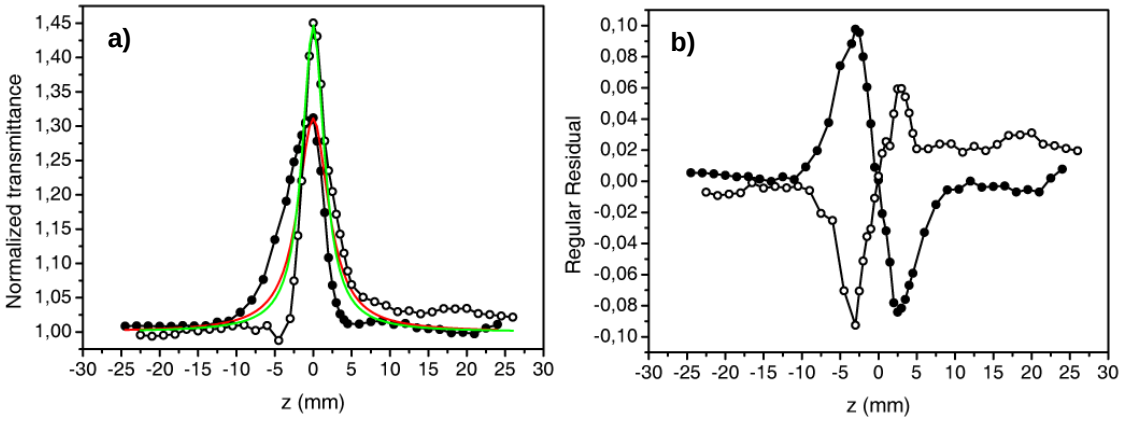

Figure 6.6: a) Open-aperture z-scan measurements at 20 Hz repetition rate and b) fit residual trend of gold nanoshells R_2 = 110 nm in solution, at 299 nJ with regular (black dot) and inverted (empty dot) translation stage motion. The solid lines indicate theoretical fit.

The saturation peak asymmetry is due to a reshaping of the NSs under femtosecond illumination.[14, 15] Time diffusion of NSs covered by PVP in water is too long to constantly supply fresh nanoparticles into the illumination area, during z-scan measurement. As the sample approaches the focus and the intensity increases, gold nanoshells reshape causing the nonlinear optical response changes because they have not enough time to diffuse out of the beam waist. However, the gold coverage is not completely destroyed because the NSs response continues also after reshaping. UV-visible spectra of NSs, exposed to laser irradiation for times comparable to those used by Aguirre et al[14], do not change after laser irradiation and apparently, a complete shell is not required to maintain absorption in the near infrared.

We also measured the NLO properties of NSs with R_2 = 60 nm and R_2 = 110 nm deposited on glass substrates at 20 Hz (Figure 6.7). Again, the behavior is that of a

saturable absorber but because of the inhomogeneous NSs coverage of glass substrates, the peak is large and its intensity depends on the area illuminated. Far from the focal position, the response of the two samples should be linear; however, especially for smaller NSs which form larger and disordered aggregates, the normalized transmittance deviates significantly from one.

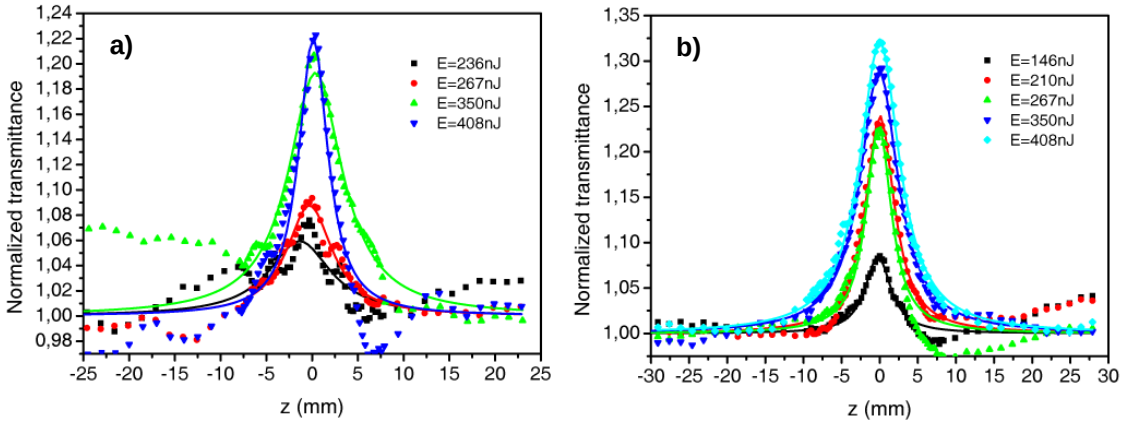

Figure 6.7: Open-aperture z-scan measurements at 20 Hz repetition rate a) of gold nanoshells R_2 = 60 nm and b) of the gold nanoshells R_2 = 110 nm deposited on glass slides, at different pulse energies. The solid lines indicate theoretical fit.

Comparing with z-scan measurements in solution (Figure 6.5c), the saturation peak for NSs with R_2 = 110 nm deposited on glass substrates (Figure 6.7b) is in general more symmetric also at high energies. Apparently, NSs deposited do not reshape during laser pulses irradiation. Large NSs deposited on glass substrate aggregate in a hexagonal close-packed structure which causes a red shift of the plasmon band shoulder from 900 to 1100 nm, due to the coupling of the plasmon oscillation mode of each particle with the neighboring NSs. Even if the excitation is at 806 nm for both samples in solution and deposited on glass, in the first case we are irradiating a single isolated particle, in the second case we irradiate a particle surrounded by and interacting with other NSs. Both the above factors may contribute to making less efficient the reshaping mechanism responsible for the peak asymmetry.

6.2.3.3 Analysis of z-scan curves for gold nanoshells

The relaxation dynamics of plasma excitations in metallic systems has been investigated extensively.[13,16,17] Briefly, the laser pulse causes an interband or intraband electron transition in the NS, depending on the excitation wavelength and intensity. The

electrons, thus excited, have a non equilibrium distribution different from the Fermi-Dirac statistics for fermions.[13] Through electron-electron scattering, the electron gas thermalizes and riches a new Fermi distribution with a higher electron temperature within 500 fs. After electron thermalization and partly during that process, electrons lose their energy further by thermal equilibration with the lattice through electron-phonon interactions. A thermalization time for the electronic gas through electron-phonon coupling of 3 ps has been obtained for different size and shape gold nanoparticles. Phonon-phonon relaxation processes follow: thermal energy will be dumped into the solvent causing the dielectric or surrounding medium to change, thereby influencing the plasmon resonance frequency of the NSs.

According to the above analysis, we believe that the z-scan results arise from the bleaching of the ground-state plasmon band which leads to saturable absorption. Working with higher energies and repetition rates increases the bleaching effect because more energy is provided to the system and a higher temperature is reached. Within a single fs pulse only the rise in electronic temperature should matter. However accumulation effects at higher repetition rate could cause a small increase of lattice or thermodynamic temperature to become of relevance.

Considering the time scale of the thermalization, we can also explain the asymmetry of the saturable absorption peak, which increases both with energy and repetition rate. In the literature the reshaping effect and disruption of NSs by femtosecond pulsed laser irradiation is well known.[14, 15] Depending on the laser pulse energy, on the radiation exposure time and on the shell thickness, it is possible to make a hole in the shell, to completely melt it and produce gold nanoparticles or even to remove the dielectric silica core. During z-scan measurements, as the sample is brought closer to focus, the beam irradiance increases and the shell reshapes but is not completely destroyed by pulses in the range of energy we have used, as shown by the fact that the system continues to behave as a saturable absorber.

The results of the fitting by the Sheik-Bahae model yield β values in the order of -10^{-11} cmW^{-1} but they exhibit a significant dependence on the size of the NSs and on the pulse repetition rate and energy. The minimum value (1.1×10^{-11} cmW^{-1}) is obtained for NSs with R_2 = 60 nm excited with 210 nJ energy pulses at 20 Hz whereas the higher one (9.6×10^{-11} cmW^{-1}) is evaluated for NSs with R_2 = 110 nm excited with 408 nJ energy pulses at 200 Hz. The measured order of magnitude is in sharp contrast with the literature

data reporting values ranging from -10^{-2} to -10^{-10} cmW^{-1}.[17,23] However, those data have been obtained by using laser pulse durations of nanoseconds or picoseconds and repetition rates up to 1 KHz to measure z-scan data on nanoparticles of different size, shape and state of aggregation. As noted above, the difference in pulse duration alone can justify order of magnitude differences in the obtained β values since different processes, occurring in the time scale of the laser pulse, are probed. Add to this the possible occurrence of thermal effects with nanosecond pulses or at high repetition rates and the marked discrepancies with the literature data cannot come as a surprise.

In trying to identify data that are more significant to extract reliable β values for NSs excited at 806 nm, we selected those measured at 20 Hz for NSs with R_1 = 95 nm; R_2 = 110 nm because of the regular shape of the samples and the minimization of possible thermal effects. The estimated β values are shown in Figure 6.8 as a function of pulse energy. One notices a significant increase of the absolute value of (negative) β with increasing pulse energy. This is, in itself, evidence of the fact that third-order processes, assumed as the only responsible of the nonlinear transmission in the Sheik-Bahae model, are not sufficient to account for the observed behavior. Consideration of the excitation processes that can take place in gold and contribute to the NL absorption of at 806 nm (1.54 eV) allows us to propose a simplified, tentative explanation.

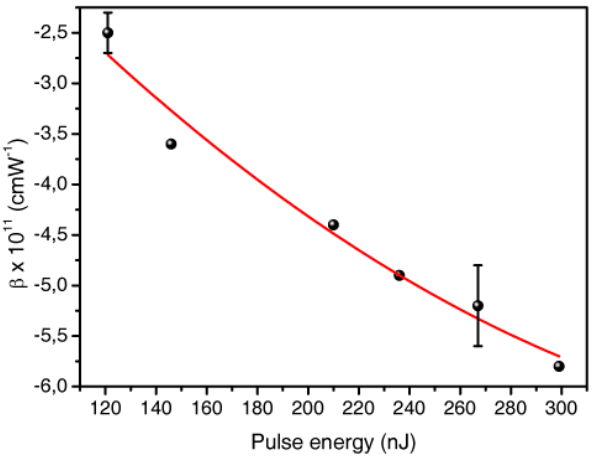

Figure 6.8: Estimated β values for R_2 = 110 nm nanoshells in solution as a function of pulse energy.

The nonlinear propagation equation including a term of order higher than that originating from the third order response reads

$$\frac{dI}{dz} = -\alpha I - \beta I^2 - \gamma I^3 \qquad (6.8)$$

In order to account for saturation effects, Eq. (6.8) should be coupled with rate equations describing the evolution, during the pulse duration, of the electron distribution within an energy range spanning from 1.54 eV below to 1.54 eV above the Fermi level, E_F. The most significant processes contributing to the relevant electron dynamics include (Figure 6.9): (i) intraband absorption of one photon to promote electrons from below to above the Fermi level: this should be the dominant contribution to absorption saturation; (ii) interband one-photon absorption from the *d*-band, lying 2.4 eV below the Fermi level, to the conduction band: this process partially replenishes the electrons up to 0.9 eV below E_F; (iii) interband two-photon absorption from the *d*-band to feed electrons up to 0.7 eV above E_F, thus contributing to saturate the intraband absorption across the Fermi level.

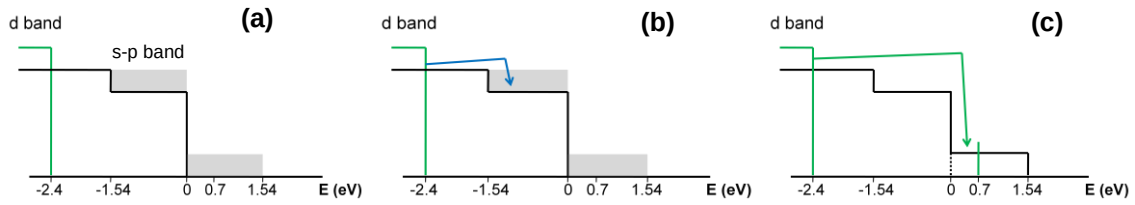

Figure 6.9: Schematic diagrams of processes contributing to the relevant electron dynamics: a) intraband absorption of one photon to promote electrons from below to above the Fermi level; b) interband one-photon absorption from the *d*-band, lying 2.4 eV below the Fermi level, to the conduction band; c) interband two-photon absorption from the *d*-band to feed electrons up to 0.7 eV above E_F.

Furthermore, the third process also gives a direct contribution to NL absorption. These three processes can be accounted for in a very simplified fashion by introducing effective absorption cross sections designated as σ_{intra}, $\sigma_{d1ph,}$ and σ_{d2ph} for the intraband, one-photon interband and two-photon interband absorptions, respectively, and by assuming rectangular pulse of duration much shorter than the electron-electron relaxation time. This latter is a clear oversimplification that however allow us to write down a very simple expression for the propagation equation

$$\frac{dI}{dz} = -\sigma_{intra}N_C I + \left[2(\sigma_{intra})^2 N_C - \sigma_{intra}\sigma_{d1ph}N_d - \sigma_{d2ph}N_d\right]I^2 + \sigma_{intra}\sigma_{d2ph}N_d I^3 \tag{6.9}$$

By comparison with Eq. (6.8) we see that

$$\beta = -\left[2(\sigma_{intra})^2 N_C - \sigma_{intra}\sigma_{d1ph}N_d - \sigma_{d2ph}N_d\right] \quad \text{and} \quad \gamma = -\sigma_{intra}\sigma_{d2ph}N_d \tag{6.10}$$

Therefore, the condition that must be fulfilled in order to have saturated absorption is

$$(\sigma_{intra})^2 N_C > \left(\sigma_{intra}\sigma_{d1ph} + \sigma_{d2ph}\right) N_d/2$$

The negative value of β (Eq. (6.10)) contributes to the saturation of the absorption and, since it derives from a three-photon absorption, it accounts for the observed intensity dependence of the effective value of β that we have measured.

6.3 Time-resolved transient absorption spectroscopy

While *Z*-scan is used as frequency-domain technique, providing information on static properties of a molecular system (absorption coefficients, cross sections, transition dipole moments, etc.) as a function of wavelength, the time-resolved transient absorption (TA) spectroscopy allows studying the time evolution of the excited states and the lifetimes of short living species by measuring the time dependent TA signal.

6.3.1 Technique and fundamental relations of Pump and Probe

In a typical pump and probe (P&P) experiment two ultrashort laser pulses are directed onto a sample in which they spatially overlap. The first pulse ("pump"), more intense, excites the sample and induces optical changes that are monitored through the absorption changes of a second weaker pulse ("probe") as a function of the time delay Δt between pump and probe pulses. If one assumes that the coherent interactions are very fast with respect to population relaxation processes and the time width of the applied laser pulses, then the probe intensity will depend only on the time-dependent population terms. Under this assumption, the absorption of the probe pulse before and after the application of the pump beam will be different, because the resulting depopulation of the ground state will lead to bleaching of the ground state absorption while the population generated in the excited states will cause excited state absorption (ESA) and stimulated emission. Before pump pulse application, the attenuation of the weak probe beam with incident intensity I_0 travelling through a sample with length L and molecular density N, can be expressed by the Lambert-Beer law:

$$I(\infty) = I_0 exp(-\sigma_G NL) \tag{6.11}$$

whereas after application of the pump beam, the corresponding relation is:

$$I(t) = I_0 exp\left\{-\sigma_G L[N - N_e(t)] + \sum_i N_i(t)\left(\sigma_{em,i} - \sigma_{E,i}\right)L\right\} \tag{6.12}$$

with $\sum_i N_i(t) = N_e(t)$, where the sum is over all populated excited states i, $N_i(t)$ are the population density of the excited state i at the time t and $N_e(t)$ denotes the total excitation

density at the same time. $I(\infty)$ and $I(t)$ display the probe beam intensity after the sample, in the absence or presence of the pump pulse respectively. The cross section for ground state absorption, ESA and stimulated emission are denoted by σ_G, σ_E, σ_{em}, respectively.

Combining Eq. 6.11 and 6.12 yields:

$$\frac{I(t)}{I(\infty)} = 1 + \frac{I(t)-I(\infty)}{I(\infty)} = exp\{L[\sigma_G N_e(t) + \sum_i N_i(t)(\sigma_{em,i} - \sigma_{E,i})]\} \quad (6.13)$$

and extracting the natural logarithm:

$$ln\left[1 + \frac{I(t)-I(\infty)}{I(\infty)}\right] = L[\sigma_G N_e(t) + \sum_i N_i(t)(\sigma_{em,i} - \sigma_{E,i})] \quad (6.14)$$

If the change in transmission upon pumping the sample is small, i.e. $I(t) - I(\infty) = \Delta I(t) \to 0$, then:

$ln\left[1 + \frac{I(t)-I(\infty)}{I(\infty)}\right] \approx \frac{\Delta I(t)}{I(\infty)}$ and $I(\infty) \approx I_0$, so that

$$\frac{\Delta I(t)}{I(\infty)} \approx L[\sigma_G N_e(t) + \sum_i N_i(t)(\sigma_{em,i} - \sigma_{E,i})] \quad (6.15)$$

Moreover, it is easy to demonstrate the relation between $\Delta I/I(\infty)$ and the optical density variation (ΔOD) or transmittance variation (ΔT) induced by the pump at time t:

$$\frac{\Delta I(t)}{I(\infty)} = \Delta T = -2.302\Delta OD \quad (6.16)$$

When in a P&P experiment ΔOD (or ΔT) is measured as a function of the delay time Δt at a fixed probe wavelength λ_2, we obtain a typical trace in which at $\Delta t < 0$ (the probe reaches the sample before the pump) the signal is zero because the probe is not affected by the pump; at $\Delta t = 0$, when the two pulses are exactly superimposed in time, a sudden change (either positive or negative) of the signal is registered, while for $\Delta t > 0$ (the probe reaches the sample after the application of the pump) the registered signal will vary as function of Δt. From the fitting of these time dependent signals, with a proper kinetic model, the time constants characterizing the relaxation processes of the system can be determined. Moreover, if the decays are measured at several λ_2, it is possible to plot ΔOD at fixed Δt as a function of λ_2, obtaining the TA spectrum. Therefore the P&P technique allows exploring not only the dynamics of a medium, but also its ESA properties. In both cases, Eq. 6.14 shows that ΔOD is positive when ESA dominates, while it is negative when ground state bleaching and/or stimulated emission dominate.

6.3.2 Experimental set up of P&P

Figure 6.10 shows the experimental set up employed for P&P measurements.

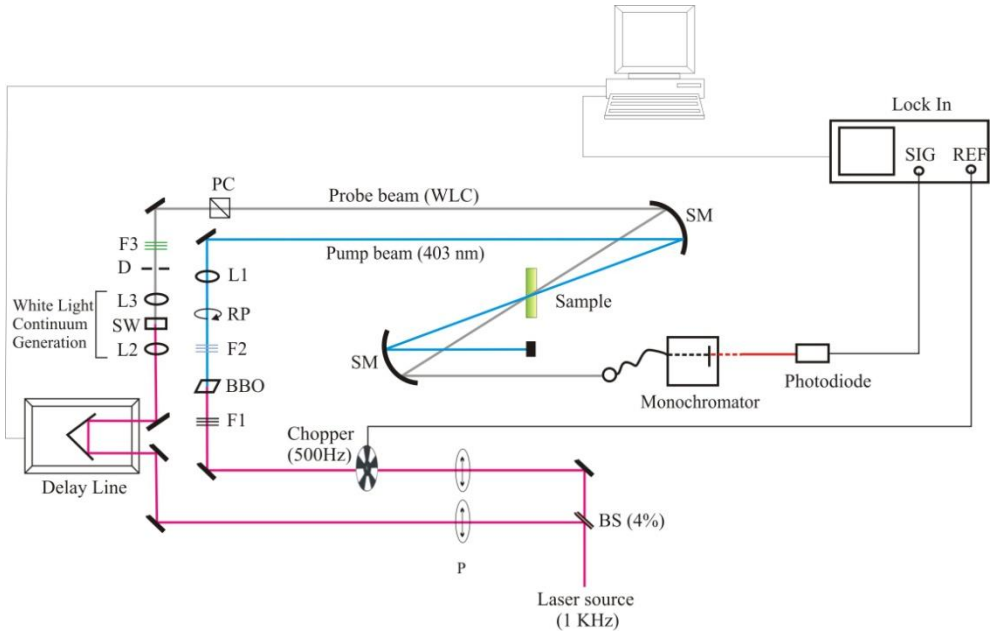

Figure 6.10: Experimental set up for P&P technique. P=half waveplate for verticalize the polarization of the laser beam; BS=beam splitter; L1, L2, L3=convex lens; SW=sapphire window; D=diaphragm; F1=neutral density filters; F2=colored glass filters; F3=longpass or shortpass filters; BBO=doubling crystal; RP=half waveplate; PC=cubic polarizer; SM=spherical mirror.

The fundamental laser beam at 806 nm is separated by a 4% beam splitter (BS) into two paths: the weaker one is used to generate the probe beam, while the other one is used as pump pulse. The pump is frequency doubled, using a BBO doubling crystal, and set at 403 nm; coloured glass filters (F2) allow removing the fundamental beam from the duplicated one. The intensity of the pump pulse is modulated by means of neutral density filters (F1) until it reaches typical values in the range 150-200 μJcm^{-2}. While the pump goes through a fixed optical path, the probe passes through a computer controlled motorized delay line which allows a continuous modulation of the delay time Δt from zero up to 1 ns between the arrival of the two pulses on the sample. After the delay line, the probe beam is focused (L2) into a sapphire window (SW) to generate WLC from 440 to 1100 nm (probe beam), which is collected and collimated by a second lens (L3).

Since the WLC still contains a large amount of the fundamental beam at 806 nm, that in the P&P experiment can give undesired heating of the sample as well as NL absorption effects, shortwave or longwave pass filters are suitably employed (F3) to remove this contribution. The beam waists of the pump and probe beams are still set so that $w_{0,1} \approx 5\ w_{0,2}$. The pump and the probe beams are then focused inside the sample (inside a 1mm-thick quartz cell) by a spherical mirror. After the sample, the pump pulse is blocked, while

the probe is focused into an optical fibre coupled with a monochromator allowing single wavelength measurements. The signal, at each selected wavelength, is then detected by a photodiode (Si for wavelengths in the visible region and InGaAs in the NIR), averaged by an oscilloscope and finally processed by a PC program.

In order to avoid contributions from relaxation promoted by rotational diffusion, all experiments employ linearly polarized pump and WLC beams and the angle between their polarization vectors is set at approximately 55° (magic angle), by means of a high energy broadband polarizing cube (PC) placed on the WLC beam and an half waveplate (RP) on the pump beam. Some experiments are also performed with the angle between pump and probe polarization vectors set at 0° (VV) or 90° (VH).

A mechanical chopper, set at 500 Hz, is placed on the pump beam, while the probe beam is kept at 1 kHz. A digital Lock-In amplifier (Stanford Research SR830), triggered by the mechanical chopper, averages directly the difference of the probe beam intensity with and without the pump beam. A homemade PC program moves the delay line and measures the average signal from the Lock-In amplifier.

6.3.3 P&P measurements on metallic nanostructures

Electron-phonon interaction is the most important energy relaxation process in metal nanostructures and determines many important properties such as thermal conductivity and electoral conductivity. For this reason, several efforts are done for studying nanostructures ultrafast dynamics.[13, 18, 19]

For gold nanostructures, independently from the size and shape, three processes characterize ultrafast dynamics: electron-electron scattering (about 500 fs), electron-phonon coupling (about 2-5 ps) and phonon-phonon interaction (>30 ps).

Electron-electron scattering is usually of the same time scale as the pulse excitation and so it is quite difficult to measure. Since electron-electron scattering and electron-phonon coupling are not completely sequential processes, deviations from a linear dependence at early times are visible.[13] The delayed rise in the signal intensity corresponds to the internal thermalization of the electron gas and it is detectable only at low pump power. Electron-phonon coupling and phonon-phonon interaction are the two processes responsible of the plasmon bleach recovery. The former gives a relaxation time of 2-5 ps and it is dependent on the pump power[20] and on the lattice crystallinity[21](see Chap. 2). The latter relaxes in more than 50 ps.

Recently, some studies on the ultrafast dynamics of functionalized nanostructures has also been performed.[22, 23] The experiments are realized in two different way, considering changes on the nanoparticle or on the molecule dynamics. Westcott et al[22] studied the effect on the nanoshells dynamics of the interaction with some polar molecules. This provokes increasing or diminishing of the nanoshell electron-phonon relaxation time depending on magnitude of the induced dipole moment of the molecule. Wiederrecht et al[23], instead, studied the coupling between the exciton of a molecular J-aggregate and the electron polarization of noble metal nanoparticles.

Nude and functionalized nanoshells (NSs) are characterized by pump and probe technique to observed changes in the dynamics because of the interaction between nanoshells and Rhodamine B (RhB).

6.3.3.1 P&P measurements on gold nanoshells nude and functionalized with Rhodamine B

P&P preliminary experiments on naked and RhB-covered nanoshells were planned, at the beginning, with the aim to study changes in the RhB dynamics because of NSs interaction. P&P measurements are performed using a 403 nm pump pulse with 1.65×1.35 mm average beam waist and an intensity of 150-200 μJcm^{-2}. The wavelength range of the white-light femtosecond probe pulse is from 450 to 1100 nm. The signal at 550 nm, to study RhB bleaching decay, is selected with a spectrograph.

Figure 6.11 compares the decays measured for naked NSs (black) and RhB-covered NSs (red) for three different relative polarization of pump and probe: magic angle (54.7°), both pump and probe vertical polarized (VV = 0°), pump vertical polarized and probe with horizontal polarization (VH = 90°). The symbols represent the experimental points, whereas the solid lines the corresponding fit. On the y-axis, the differential transmittance $\Delta T/T$ is reported. $\Delta T(t)$ is defined as $T(t)_{\text{with pump}} - T(t)_{\text{without pump}}$, so it is positive when the presence of pump beam leads to an increase of the transmittance (bleaching). Usually, literature works report $-\Delta T/T$ on the y-axis of the decay, so that the bleaching is conventionally represented by a dip in the transient spectrum.

As shown in Figure 6.11, the relaxation dynamics of NSs functionalized with RhB is completely different from the dynamics of RhB molecules (Fig. 6.11d). The dye alone decays very slowly, about 1 ns, instead the system NSs-RhB decays in picoseconds. The dynamics is similar to the one of naked NSs and it can be associated to electron-phonon

relaxation but it is faster. Independent of the relative pump and probe polarization, the NSs time decay is 4.9 ps instead the NSs-RhB time decay is 3.7 ps.

NSs present a relaxation process analogous to the nanoparticles and nanorods one, reported in literature.[13] The pump excitation causes an instantaneous change in the distribution of the conduction electrons of the metal shell. The non-thermal distribution is rapidly relaxed by scattering between electrons in a time which is comparable to the laser pulse duration. A new equilibrium distribution around the Fermi level at higher temperature is obtained in this way. The new equilibrium distribution is thermalized through electron-phonon scattering, in few picoseconds.

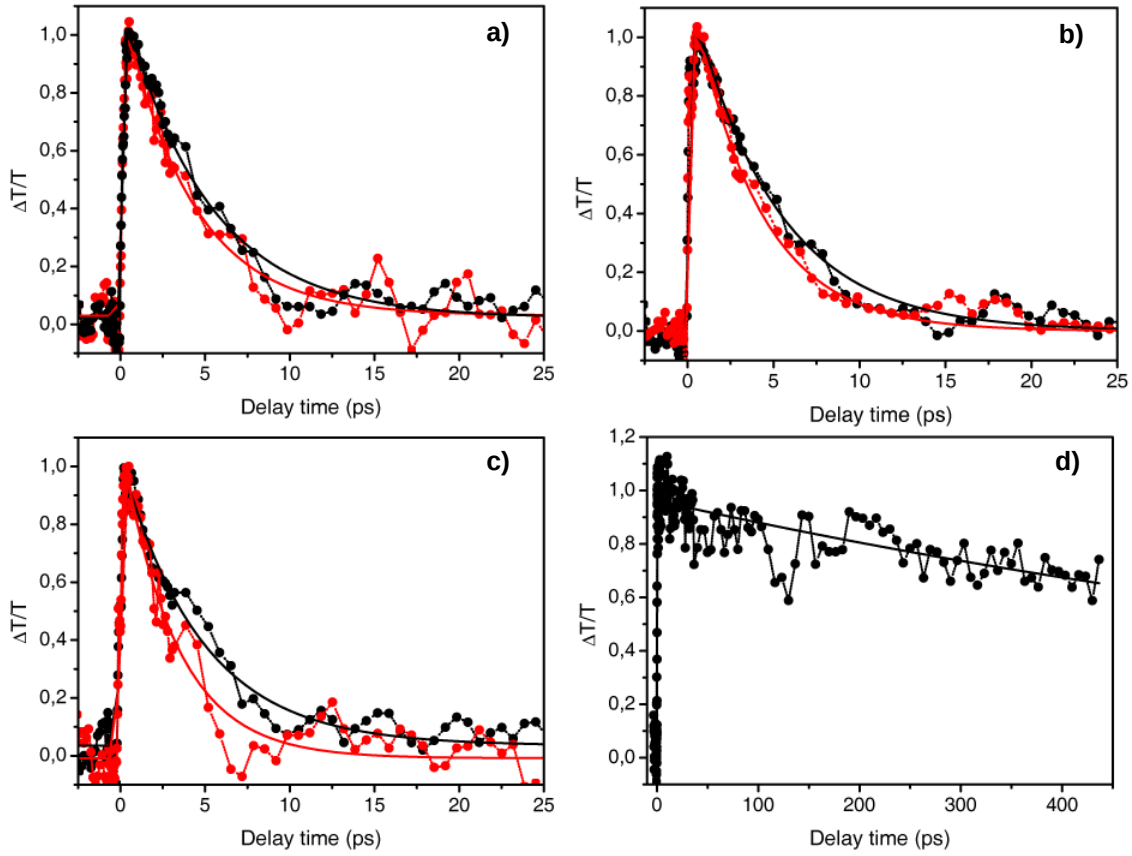

Figure 6.11: P&P measurements of naked NSs (black) and RhB-covered NSs (red) for three different relative polarization of pump and probe: a) magic angle, b) VV = 0°, c) VH = 90°. In d) RhB transient bleach decay.

RhB modifies the NSs dynamics and reduces the electron-phonon scattering time. Physically, the electronic perturbation induced by RhB introduces an additional channel by which hot electrons can decay. In this picture, the interaction between the molecules and the metal perturbs the electronic potential resulting in a local change in the screening of the Coulomb interaction between electrons, modifying the relaxation.

To better understand this effect, further measurements are planned using a 403 nm pump pulse and probing at 806 nm. We will also characterize molecules more polar than RhB to see if the perturbation phenomena are stronger.

In Figure 6.11c, it seems that there are some oscillations. This result should be confirmed, but in literature, some authors discussed about it.[19, 24] They explained these oscillations considering that as the electronic temperature decays there is a concomitant increase in the temperature of the lattice. This rise in the lattice temperature causes the particles to expand. For example,[19] for Au particles larger than ca. 8 nm, the increase in the lattice temperature is faster than the lowest-frequency acoustic phonon mode of the particles. Thus, the lattice cannot instantaneously respond to the temperature increase. This creates a situation where the acoustic phonon modes can be impulsively excited.
As for the perturbation phenomena, also in this case further measurements, in a reduced time scale, have to been performed. We can argue that RhB should also modify the oscillation period due to electrostatic interaction.

6.4 Surface Enhancement Raman Spectroscopy (SERS)

Molecular vibrations and therefore molecular structure can be probed by the Raman scattering process.[25] Raman spectroscopy, owing to its ability to recognize typical molecule fingerprints, provides a unique approach for solving analytical problems. However, Raman scattering has an extremely small cross section, typically 10^{-30} to 10^{-25} cm^2 per molecule, with the larger values occurring only under favorable resonance Raman conditions. The small Raman cross sections require a large number of analyte molecules to achieve adequate conversion rates from excitation laser photons to Raman photons. Therefore, usually, Raman spectroscopy has been considered a technique for structural analysis, rather than a method for ultrasensitive trace detection or even as tool at the level of single molecules. However, Raman scattering literally appears in a new light when it takes place in the local optical fields of metal nanostructures. The favorable optical properties of these metal nanostructures, based on their surface plasmon polaritons, provide the key effect for the observation of enhanced Raman signals for molecules attached to them, the effect of surface-enhanced Raman scattering (SERS). Large enhancement factors of up to 14 orders of magnitude provide for the small Raman cross section and transform Raman spectroscopy from a structural analytical tool to a

structurally sensitive single-molecule and nanoscale probe. At present, SERS is the only way to detect a single molecule and simultaneously probe its chemical structure.

6.4.1 Technique and fundamental relations of SERS

It is generally agreed that two effects contributes to the observed total enhancement of many orders of magnitude, the "electromagnetic" field and the "chemical first layer" ones.[26]

Figure 6.12 presents a schematic of normal and surface enhanced Raman scattering. In normal Raman scattering, the total Stokes Raman signal I_{NRS} is given by:

$$I_{NRS}(\nu_S) = NI(\nu_L)\sigma^R_{free}$$

where σ^R_{free} is the Raman cross section of free molecules, $I(\nu_L)$is the excitation laser intensity and *N* the number of molecules in the probed volume (Fig. 6.12a). Because of the extremely small Raman cross sections, at least 10^8 molecules are necessary to generate a measurable normal Raman scattering signal. In a SERS experiment (Fig. 6.12b), the molecules are attached to a metallic nanostructure (single nanoparticles, nanorods, aggregates, nanoshells, etc). The surface enhanced Stokes Raman signal I_{SERS} is given by

$$I_{SERS}(\nu_S) = N'I(\nu_L)|A(\nu_L)|^2|A(\nu_S)|^2\sigma^R_{ads}$$

and it is proportional to the Raman cross section of the adsorbed molecule σ^R_{ads}, the excitation laser intensity $I(\nu_L)$, and the number of molecules which are involved in the SERS process *N*'. $|A(\nu_L)|$ and $|A(\nu_S)|$represent field enhancement factors of the laser and Stokes fields, respectively.

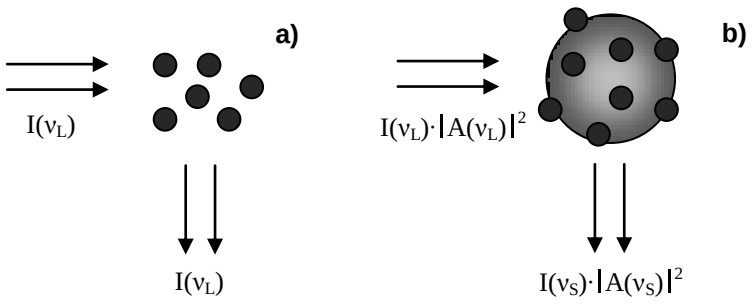

Figure 6.12: Comparison of a) normal and b) surface enhanced Raman scattering.

"Chemical first-layer" effects include enhancement mechanisms of the Raman signal, which are related to specific interactions, i.e., electronic coupling between the molecule and metal, resulting in an "electronic" enhancement.[27] Chemical SERS enhancement is

expressed as an increased Raman cross section of the adsorbed molecule compared to the cross section in a normal Raman experiment. Possible electronic SERS mechanisms involve a resonance Raman effect due to a new metal molecule charge-transfer electronic transition or a dynamic charge transfer between the metal and molecule, which can be described by the following four steps: (a) photon annihilation, excitation of an electron into a hot electron state, (b) transfer of the hot electron into the LUMO of the molecule, (c) transfer of the hot electron from the LUMO back to the metal, (d) return of the electron to its initial state and Stokes photon creation. The magnitude of chemical enhancement has been estimated to reach not more than factors of 10-100.

The electromagnetic or field enhancement factors ($|A(\nu_L)|$ and $|A(\nu_S)|$) arise from enhanced local optical fields, near the metal surface, due to excitation of surface plasmon resonances. In fact, the light from the laser beam excites the surface plasmons that radiate a dipolar field. The coherent interaction of the incoming electric field with the dipolar field leads to a redistribution of the electric field intensities near the nanostructure surface and a molecule adsorbed on the metal feels an enhanced excitation. In the same way, the Raman scattered field is enhanced. SERS enhancement is particularly strong when both laser and scattered field are in resonance with the surface plasmons and this is quite common because the width of the surface resonance is larger than the frequency shift between the laser and the scattered lights. Therefore, the laser and Raman scattered fields increase by about the same amount and the signal power scales with the fourth power of the local optical field enhancement.[28] The enhancement depends on the type of metal and on the nanostructures. Electromagnetic field enhancement has been calculated for isolated single colloidal silver and gold spheroids and for coupled nanoparticles.[29] Closely spaced interacting particles seem to provide extra field enhancement, particularly near the gap sites between two particles in proximity, resulting in electromagnetic SERS enhancement factors up to 10^8. Theory also predicts strong enhancement of electromagnetic fields for sharp features and large curvature regions[30] and on nanoshells structures.[31, 32]

6.4.2 Experimental set up for SERS

The Surface Enhanced Raman Spectroscopy (SERS) measurements are performed with a Renishaw micro-Raman instruments employing a 50× microscope objective.

The instrument, directly interfaced to a confocal microscope (Leica DMLM), has low-power laser sources and a computer management tool. Laser sources available are the 488

nm of an Argon laser and the 632.8 nm of the He-Ne laser (which is the one used to excite the sample). The key characteristics of this system are: high stability and optical efficiency (> 30%), possibility of continuous scanning for extended spectral ranges, high spatial resolution and a completely integrated software with Windows XP.

In Figure 6.13, a schematic image is shown. The He-Ne laser has a maximum output of 17 mW at 632.8 nm while the Argon laser has a maximum intensity of 48 mW at 488 nm. The laser beam covers a path defined by mirrors driven by stepper motors whose position has been stored for each laser line used. At the beginning of its route, the laser beam is attenuated through a series of filters with different optical density, interchangeable via software. After the input mirrors, Beam Expander lenses are mounted to expand the nearly point source input radiation into a parallel beam of about 6mm in diameter (equal to the back microscope aperture). By varying the distance of the two components of the Beam Expander, the spot size changes and it is possible to control the focus position of the microscope. Between the two blocks of the Beam Expander, there is a pin-hole, used for self-alignment by software or as a diaphragm for confocal microscopy, which allows greater spatial resolution in depth.

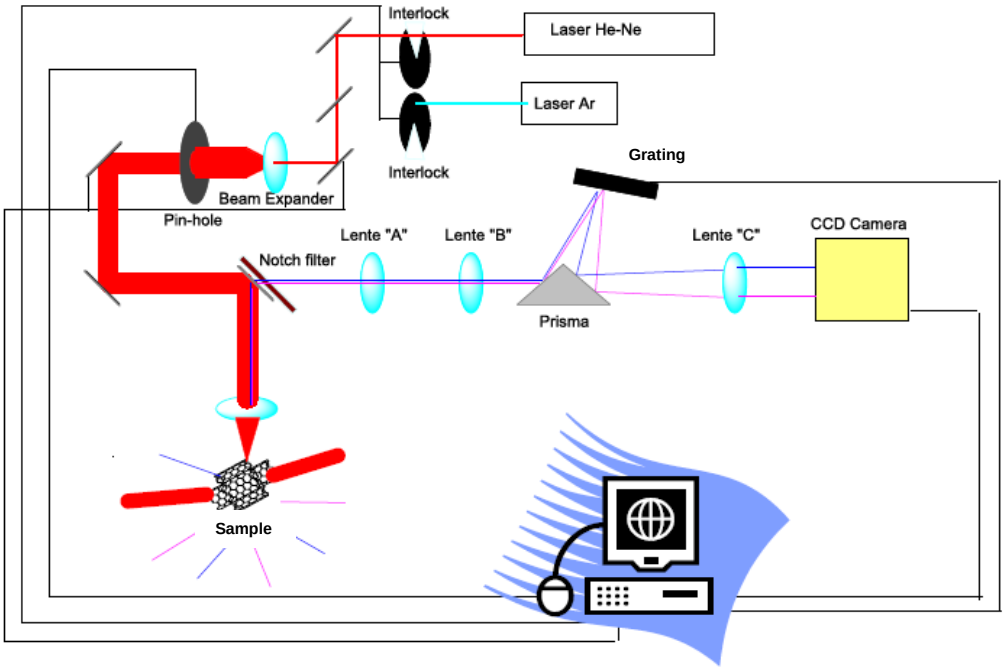

Figure 6.13: Experimental set up for Micro Raman.

The beam is then reflected by the notch-filter to the sample. The microscope allows the focusing of the incident beam with a precision of about 2 microns. The Podule, located

near the microscope, includes a beam splitter that sends the beam on the sample and from the sample to the camera, by which it is possible to see the sample on a screen, or on the CCD. Inside the Podule, a monocrystalline silicon reference is located which is used for a rapid calibration of the instrument.

The illumination of the sample with visible light is obtained with a source inside the Podule. The microscope has four objectives 5×, 20×, 50× (Olympus) and a 20× with a long focal (Leica), all assembled under the same support so that the focus is kept, going from one objective to another. The laser spot on the sample is about 2 μm using the 50× objective, 5 μm for 5× and 20×. The sample holder plate moves with a 1 μm resolution.

The light, collected in backscattering by the same objective, is filtered through the notch-filter that cuts almost all elastically scattered light, transmitting only the Raman emission of the sample. The introduction of holographic notch-filters, for filtering the exciting radiation, has allowed to use monochromators extremely compact with great gain of sensitivity and simplicity of the apparatus. In any case, cut-off capability of a notch-filter is limited to about 80 cm^{-1}, against few cm^{-1} for a system based only on gratings. The cut is optimized in the Stokes, while in the anti-Stokes the usable area comes from about 100 cm^{-1} to more than 200 cm^{-1}. The radiation scattered and collected by the objective of the microscope, after been filtered by two notch filters, passes a series of lenses for each specific wavelength and then reaches the diffraction grating with 1800 lines/mm, a new specific lens and thus the CCD.

The detector is made of a CCD (Charge-Coupled Device) of 400 pixels, each of size 22μm × 22μm, mounted on a spectrograph with planar focus. Each pixel consists of a silicon diode that generates a current when hit by electromagnetic radiation. Columns of pixels are the channels within which electrons, in a given range of energy, are collected. The sensor can analyze a range of wavelengths, or alternatively should be centered around a given value of Raman shift. CCD detector can be used also to capture two-dimensional images of the sample through the technique of Raman Global Imaging, using all 400 pixels of the CCD.

6.4.3 SERS measurements on gold nanoshells functionalized with benzenethiol

TEM measurements on nanoshells (Chap. 4) showed that such nano-objects did not present a complete gold shell but rather an incomplete and rough-edge layer. Such structure should be quite interesting for SERS analysis. In fact, it is reported in the

literature that nanoshells present a SERS enhancement as large as 10^{10}.[32] Moreover, such shell geometry can be appealing to exploit the huge enhancement in the local field that take place in apex.[30] In order to explore the potentiality of the nanoshells in SERS, preliminary study on NSs deposited on aminopropyltrimetoxysilane functionalized glass substrates are performed. A 29% nanoshells glass slides coverage is estimated from AFM images. In general, all estimates of enhancement factors based on the comparison of SERS intensity with normal Raman intensity suffer from the fact that the number of target molecules really involved in the SERS process is unknown. At the moment, we have not solved this problem and we are not able to estimate precisely the amount of NSs under illumination nor the number of molecules for covered a single NSs. For this reason, the following SERS characterization is only qualitative.

NSs functionalized glass slides have been functionalized with a commercial benzenethiol. Particularly, we dipped the samples in a solution of 25 μL of benzenethiol in 15 mL of methanol for 20 hours. Then we rinsed the sample repeatedly in methanol.
In Figure 6.14, microscope image of the sample area illuminated (at 632.8 nm) and the relative SERS signal are shown. The spectra are collected at different laser excitation powers (1.7×10^{-2} mW, 0.17 mW, 0.85 mW and 1.7 mW) with three accumulation each of 30 seconds. No degradation signs are observed even at 1.7mW laser power.

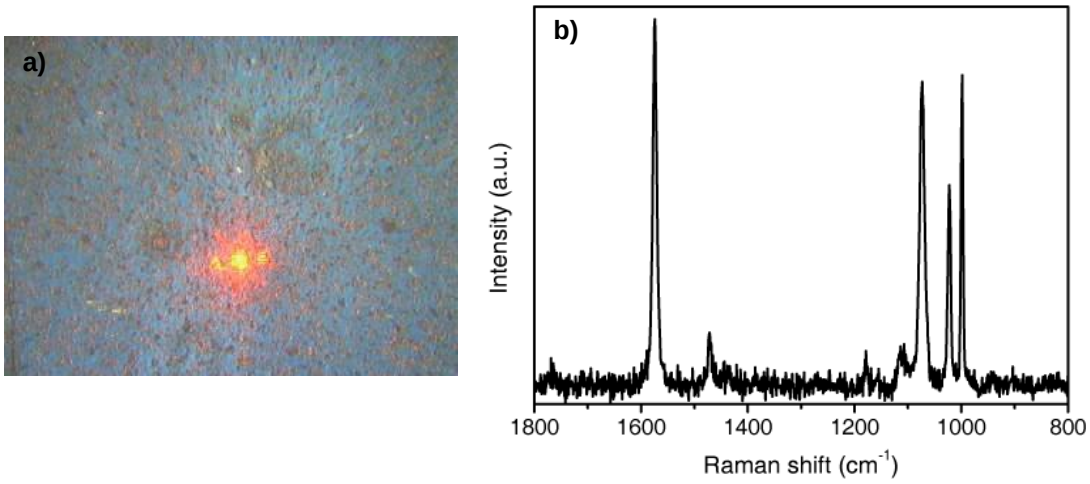

Figure 6.14: a) Microscope image of nanoshells on glass substrate. The bright red spots indicate point of collection of SERS signals. b) SERS signal of the benzenethiol deposited on nanoshells.

In Figure 6.14b, benzenethiol Raman bands are clearly visible: 998 cm^{-1} is assigned to the in-plane ring-breathing mode, 1023 cm^{-1} to the in-plane C-H bending mode, 1073 cm^{-1} to

the in-plane ring-breathing mode coupled with the C-S stretching mode, and 1574 cm^{-1} to the C-C stretching mode.

Let us do some qualitative considerations. As estimated in Chap. 5, about 10000 molecules should attach on a single nanoshell (and this is probably an overestimated value) but in this sample only half of nanoshell surface is available because of the glass substrate deposition. The laser spot size is 2 μm and so the illuminated area is ca. 4 μm^2, of which only 29% is covered by nanoshells (each nanoshell of 0.11 μm outer radius occupies c.a. 0.04 μm^2). In this way, c.a. 30 nanoshells are estimated to be excited. If we consider the number of molecules for single nanoshell, it is clear that the concentration of benzenethiol is too low to give the Raman signal in Figure 6.14b, except in case of strong enhancement field effects.

As for P&P characterization, also in this case, further measurements will be done because of the promising results.

References

(1) Collini, E. Self-assembled systems in condensed phases: nonlinear response and excited state dynamics, Università degli Studi di Padova, Padova, 2006.

(2) Sheik-Bahae, M.; Said, A. A.; Wei, T. -.; Hagan, D. J.; Van Stryland, E. W. *IEEE Journal of Quantum Electronics* **1990**, *26*, 760-769.

(3) Elim, H. I.; Yang, J.; Lee, J. Y.; Mi, J.; Ji, W. *Applied Physics Letters* **2006**, *88*, 083107.

(4) Falcão-Filho, E. L.; De Araújo, C. B.; Rodrigues, J. J. *J. Opt. Soc. Am. B* **2007**, *24*, 2948-2956.

(5) Gao, Y.; Zhang, X.; Li, Y.; Liu, H.; Wang, Y.; Chang, Q.; Jiao, W.; Song, Y. *Optics Communications* **2005**, *251*, 429-433.

(6) Smith, D. D.; Fischer, G.; Boyd, R. W.; Gregory, D. A. *J. Opt. Soc. Am. B* **1997**, *14*, 1625-1631.

(7) Philip, R.; Kumar, G. R.; Sandhyarani, N.; Pradeep, T. *Physical Review B* **2000**, *62*, 13160-13166.

(8) Wang, W.; Wang, Y.; Dai, Z.; Sun, Y.; Sun, Y. *Applied Surface Science* **2007**, *253*, 4673-4676.

(9) Piredda, G.; Smith, D. D.; Wendling, B.; Boyd, R. W. *J. Opt. Soc. Am. B* **2008**, *25*, 945-950.

(10) Qu, Q.; Zhang, Y.; Li, H.; Qiu, J.; Zhu, C. *Optical Materials* **2006**, *28*, 259-265.

(11) Matsubara, S.; Hayakawa, T.; Yang, J.; Nogami, M.; Okamoto, S.; Koshikawa, N. *J. Phys. Chem. C* **2008**, *112*, 13917-13921.

(12) Lamarre, J. M.; Billard, F.; Kerboua, C. H.; Lequime, M.; Roorda, S.; Martinu, L. *Optics Communications* **2008**, *281*, 331-340.

(13) Link, S.; El-Sayed, M. A. *Int. Revews in Physical Chemistry* **2000**, *19*, 409-453.

(14) Aguirre, C. M.; Moran, C. E.; Young, J. F.; Halas, N. J. *J. Phys. Chem. B* **2004**, *108*, 7040-7045.

(15) Prasad, V.; Mikhailovsky, A.; Zasadzinski, J. A. *Langmuir* **2005**, *21*, 7528-7532.

(16) Muskens, O. L.; Del Fatti, N.; Vallée, F. *Nano Lett.* **2006**, *6*, 552-556.

(17) Park, P.; Pelton, M.; Liu, M.; Guyot-Sionnest, P.; Scherer, N. F. *J. Phys. Chem. C* **2007**, *111*, 116-123.

(18) Logunov, S. L.; Ahmadi, T. S.; El-Sayed, M. A.; Khoury, J. T.; Whetten, R. L. *J. Phys. Chem. B* **1997**, *101*, 3713-3719.

(19) Hodak, J. H.; Henglein, A.; Hartland, G. V. *Pure Appl. Chem.* **2000**, *72*, 189-197.

(20) Link, S.; El-Sayed, M. A. *J. Phys. Chem. B* **1999**, *103*, 8410-8426.

(21) Huang, W.; Qian, W.; El-Sayed, M. A.; Ding, Y.; Lin Wang, Z. *J. Phys. Chem. C* **2007**, *111*, 10751-10757.

(22) Westcott, S. L.; Averitt, R. D.; Wolfgang, J. A.; Nordlander, P.; Halas, N. J. *J. Phys. Chem. B* **2001**, *105*, 9913-9917.

(23) Wiederrecht, G. P.; Wurtz, G. A.; Hranisavljevic, J. *Nano Lett.* **2004**, *4*, 2121-2125.

(24) Grant, C. D.; Schwartzberg, A. M.; Norman, T. J.; Zhang, J. Z. *J. Am. Chem. Soc.* **2003**, *125*, 549-553.

(25) Kneipp, K.; Kneipp, H.; Kneipp, J. *Acc. Chem. Res.* **2006**, *39*, 443-450.

(26) Kneipp, K.; Kneipp, H.; Itzkan, I.; Dasari, R. R.; Feld, M. S. *Chem. Rev.* **1999**, *99*, 2957-2975.

(27) Kneipp, K.; Kneipp, H.; Manoharan, R.; Itzkan, I.; Dasari, R. R.; Feld, M. S. *Bioimaging* **1998**, *6*, 104-110.

(28) Kneipp, K. *Physics Today* **2007**, 40-46.

(29) Javier Garcıà de Abajo, F. *J. Phys. Chem. C* **2008**, *112*, 17983-17987.

(30) Kelly, K. L.; Coronado, E.; Zhao, L. L.; Schatz, G. C. *J. Phys. Chem. B* **2003**, *107*, 668-677.

(31) Tanabe, K. *J. Phys. Chem. C* **2008**, *112*, 15721-15728.

(32) Jackson, J. B.; Halas, N. J. *PNAS* **2004**, *101*, 17930-17935.

CHAPTER 7

Work function of gold nanoshells

In this chapter, work function (WF) measurements of nanoshells deposited on ITO (Indium Tin Oxide) substrates are described. This section may appear a little far from the main interest in studying interactions between molecules and metallic nanostructure but it is not. Recent efforts have been concentrated on the exploitation of surface plasmon resonances of metal nanoparticles (NPs) to improve photovoltaic devices. The large electromagnetic field enhancement that occurs in the vicinity of the metal surface and the dependence of the resonance wavelength on the NPs' size and shape have been demonstrated to increase optical absorption of incident photons and photocurrent in both organic[1, 2] and solid-state[3, 4] photovoltaic device structures. Also nanoshells (NSs) have been employed in photovoltaic research field. For example by changing the NSs size, the device may improve the solar spectrum harvesting[5] and, in particular, it can enhance or suppress photocurrent[6] at specific wavelengths, owing to its plasmon bands.

Furthermore, metal nanostructures not only interact with molecules and polymers to enhance absorption and emission properties, but they also modify the work function of ITO glass substrate, the hole injecting electrode on common organic semiconductors device.[7-10] Several strategies are reported in the literature to modify ITO WF with surface conditioning[8, 11] or with formation of self-assembled monolayers (SAMs) of dipolar molecules[12-16] The interest is to control the electrode-semiconductor interface and

especially the height of the barrier for charge injection. Both this parameters are crucial to improve device performance and to prolong its lifetime.

WF measurements on NSs have been performed with Kelvin Probe Microscopy (KPM) method. I spent three months in the group of Professor Franco Cacialli at University College London (Department of Physics and Astronomy and London Centre for Nanotechnology - LCN) working on this topic.

I also performed some studies on the sub-microscopic distribution of work functions and potentials, using Scanning Kelvin Probe Microscopy (SKPM) method, thanks to the implementation of a Kelvin probe mode in an atomic force microscope. These measurements have been performed in collaboration with Dr. Piero Schiavuta and Dr. Francesco Marinello at Nano Fabrication Facility – NanoFab (Venice).

7.1. Kelvin Probe Microscopy and Scanning Kelvin Probe Microscopy: fundamental principles

For a better understanding of how KPM and SKPM work, it is necessary to briefly discuss some fundamental principles behind these techniques.[17]

When we talk about electrode potentials, we usually refer to the potential drop at the metal/solution interface. However, this potential difference is not directly measurable because the electrode potentials are referred to a standard.

First, we consider the definition of the work function: the WF is defined as the minimum work that is required for extracting an electron from the sample to the vacuum level. It is comprised of two parts, the chemical work and a part that takes into account the electrostatic work to transport the charged electron through the dipole layer of the surface:

$$\Phi = -\mu_e + e\chi \tag{7.1}$$

where μ_e is the chemical potential (i.e. the chemical work to transfer the electron from the infinity into the sample) and χ is the so called dipole or surface potential, i.e. the potential drop between just inside the bulk and just outside of it.

In the general case, the sample may be charged and so an additional work is required to transfer the electron from just outside the surface to a position infinitely far away: eψ, ψ being the Volta potential. The Volta potential ψ can be directly calculated from the surface charge and the geometry of the sample. The sum of the dipole potential χ and the Volta

potential ψ give the Galvani potential φ, i.e. the potential drop between the bulk and the vacuum level infinitely far away from the surface:

$$\varphi = \chi + \psi \tag{7.2}$$

The absolute electrode potential E_{abs} of a sample covered by a liquid layer, in analogy to the definition of the work function, coincides with the minimum work to extract an electron from the Fermi level, through the solid/liquid interface:

$$E_{abs} = \frac{1}{e}\Phi + (\psi^M - \psi^S) \tag{7.3}$$

where Φ is the work function of the metal and ψ^{M} and ψ^{S} denote the Volta potentials outside the metal and outside the solution.

For a Kelvin probe, electrically connected to the sample M, the potential barrier for transferring an electron from the bulk of M to a point near the surface of the solution phase S is given by the following equation:

$$E_{abs} = \frac{1}{e}\Phi^{\text{M}} + (\psi^M - \psi^S) = \frac{1}{e}\Phi^{\text{KP}} + (\psi^{KP} - \psi^S) \tag{7.4}$$

(no barrier must be overcome for an electron to go from the metal M into the probe KP).

If the work function of the probe KP is known, the measurement of the Volta potential difference (ψ^{KP}–ψ^{S}), directly provides the absolute potential of the sample. The measurement of such Volta potential differences is exactly what the Kelvin probe technique provides.

7.2. KPM

7.2.1 Technique and fundamental relations of KPM

In principle, the Kelvin probe consists of a metallic reference plate, which is positioned near the surface of the sample and connected to the sample by a metallic wire. In this way, the reference plate and the sample form a capacitor.[17]

After connection of the two metals the electrochemical potential $\tilde{\mu}_{\text{e}}$ of the electrons in both materials will be the same, and a charging of one sample with respect to the other causing a Volta-potential difference between the two will be observed:

$$\tilde{\mu}_e^{sample} = -\Phi^{sample} - e\psi^{sample} = \tilde{\mu}_e^{KP} = -\Phi^{KP} - e\psi^{KP} \tag{7.5}$$

where Φ is the work function defined in Eq. 7.2 and ψ is the Volta potential.

From this, it follows:

$$e(\psi^{sample} - \psi^{KP}) = e\Delta\psi_{sample}^{KP} = \Phi^{KP} - \Phi^{sample} \tag{7.6}$$

So, an equivalent Volta potential difference is established due to the difference of the work functions of sample and reference. The charging of the capacitor between reference and sample can be used for the measurement of the Volta potential difference. If the reference vibrates over the surface of the sample, i.e. the sample-reference distance is periodically modulated as $d = \tilde{d} + \Delta d \sin(\omega t)$, this induces a displacement current to flow. Assuming, for simplicity, that the capacitor is an ideal parallel plate capacitor, the capacity C is:

$$C = \varepsilon\varepsilon_0 \frac{A}{\tilde{d}+\Delta d \sin(\omega t)} \tag{7.7}$$

with ε dielectric constant of the medium; ε_0 the electric field constant; ω the frequency of the Kelvin probe vibration; A surface area of the Kelvin probe plate.

The induced ac-current in the external circuit is:

$$i_{ac} = \Delta\psi^{KP}_{sample} \frac{dC}{dt} = \Delta\psi^{KP}_{sample} (\varepsilon\varepsilon_0 A \Delta d \omega) \frac{\cos(\omega t)}{(\tilde{d}+\Delta d \sin(\omega t))^2} \approx \Delta\psi^{KP}_{sample} (\varepsilon\varepsilon_0 A \Delta d \omega) \frac{\cos(\omega t)}{\tilde{d}^2}$$

(for $\tilde{d} \gg \Delta d$)

If an external voltage U_{appl} is applied between sample and Kelvin probe:

$$i_{ac} = \left(\Delta\psi - U_{appl}\right) \frac{dC}{dt} \tag{7.8}$$

The voltage U_{appl} is changed until the current vanishes, and for this condition $\Delta\psi^{KP}_{sample} = U_{appl}$ is measured.

With the Kelvin Probe Microscopy, we measure the difference between the WF of the sample and that of the probe. To obtain the WF of the sample, first the WF of a reference surface (usually pyrolytic graphite) is measured. The difference between experimental and tabulated value reported in literature[18] corresponds to the characteristic potential of the probe.

7.2.2 Experimental set up of KPM

Work function measurements were performed with a Besocke Delta Phi Kelvin Probe S, using newly cleaved highly oriented pyrolytic graphite (HOPG) as reference surface.[19] The sample is mounted on a support which should be moved manually inside a stainless steel chamber. Inside the experimental chamber there is also the probe. The probe is shown in Figure 7.1. It is mounted on a piezoelectric drive. The reference electrode, with a sensitivity smaller than 0.1 mV, is a gold grid with a 3 mm diameter. The mean distance

between reference electrode and sample is about 1mm, measurements are performed with sample on ground potential.

An AC voltage is applied to the piezocrystal so that the plate starts to vibrate and a current is induced. The current induced is passed back to the KP control, and then converted to a voltage signal proportional to the current. A nulling routine is performed on the detected current by applying an appropriate DC bias voltage to the probe, which is measured by a multimiter.

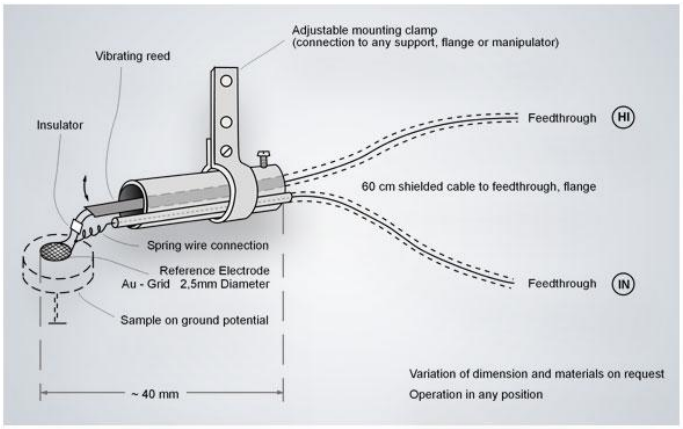

Figure 7.1: Kelvin probe structure. (www.besocke-delta-phi.de/kelvin_probe_s.htm)

7.2.3 KPM on metal nanostructures

Several works about Kelvin probe measurements of the WF of metallic nanostructures are reported in the literature.[20, 21] For example, Carrara et al[20] deposited gold and silver nanoparticles with the electrostatic layer by layer method and they measured the work function of the assembly. Gold nanoparticles WF is 0.2 eV higher than the one of bulk gold (5.1 eV). This is due to the presence of citrate molecules capping gold nanoparticles, accordingly with Turkevich synthesis.[22] It is well known in the literature that molecules can modify the WF of substrates because of their charge. Instead, the work function of silver particles increases from 5.29 to 5.53 eV as the particle size decreased.[21] These values are approximately 0.8eV higher than for clean Ag surfaces (4.30 – 4.81 eV depending on the crystalline facet). The origin of these remarkably high work functions cannot be explained in terms of either citrate induced changes in the surface dipole, as for gold nanoparticles. High resolution XPS spectra of the Ag 3d5/2 core level confirm that as-grown silver particles exhibit partially oxidized surfaces.

7.2.3.1 KPM on gold nanoshells

Work function measurements have been performed on NSs with an inner radius of 95 ± 4 nm and shell ranging from a silica core covered only by gold nanoparticles (0 nm) up to a 45 nm thick layer. We functionalized ITO substrates with NSs by two different methods: a) functionalization by 3-aminopropyltrimethoxysilane (APTMS) and a sequential immersion in NSs solution (for details see Chap. 3); b) drop casting NSs on clean ITO glasses.

In Figure 7.2, we show how the WF of APTMS functionalized ITO glasses changes when the substrate is covered by NSs with a different shell thickness. The WF of cleaned ITO is 4.70 ± 0.05 eV which is lowered to 4.61 ± 0.05 eV when we deposit APTMS on the surface. This is due to the presence of a dipole facing inwards because of the positive charge of the amino group. Depositing NSs on APTMS functionalized ITO induces a further decrease of the WF value which slightly depends on the shell thickness. Thicker shell results in lower WF.

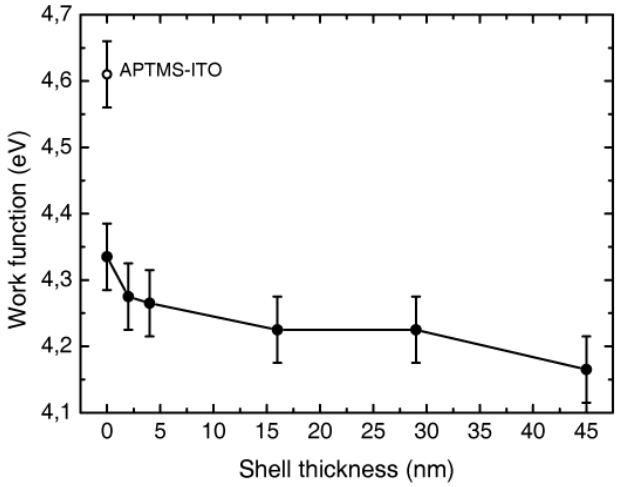

Figure 7.2: WF measurements of APTMS functionalized ITO substrates covered by NSs with an inner radius of 95 nm and different shell thickness. In (○) WF measurement of APTMS functionalized ITO glass.

The WF depends also on the extent of NSs coverage. In Figure 7.3, we report two examples of WF measurements performed on APTMS-ITO substrates covered with different amount of NSs with a shell thickness of 16 nm. Ranging from 17% to 99% coverage, WF varies between 4.2 and 4.4 eV. This result is unexpected if we consider that the WF of APTMS functionalized ITO (i.e. substrate without NSs) is 4.61 eV, whereas the

WF of a thin gold film (hypothetically, a substrate completely covered by NSs), measured in air, is 4.9 eV.[23] In contrast, the range of WF of NSs films is not in between these two values.

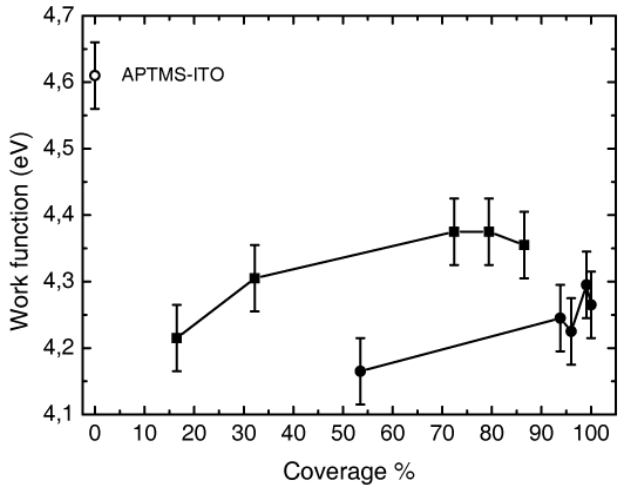

Figure 7.3: WF measurements of two sets (■ and ●) of APTMS functionalized ITO substrates covered by NSs with 95 nm inner radius and 16 nm shell thickness. Different NSs surface coverage are characterized. In (○) WF measurement of APTMS functionalized ITO glass.

We also measured the WF of NSs with different gold shell thickness deposited on ITO substrates not functionalized with APTMS.

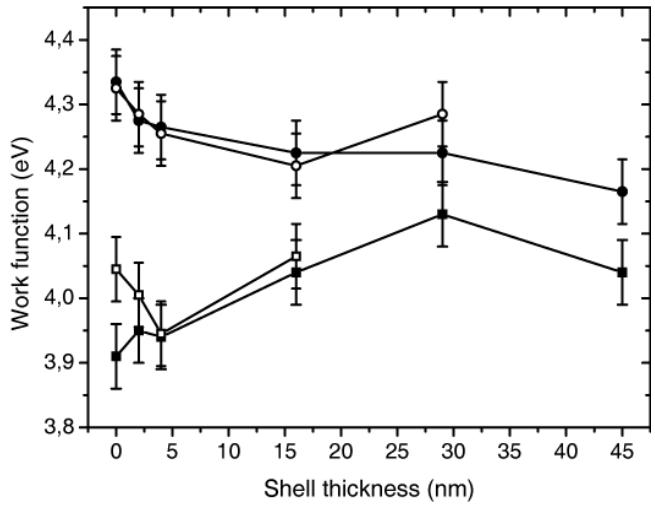

Figure 7.4: WF measurements of NSs with different shell thickness and the same coverage deposited on clean ITO (■ and □) and on APTMS functionalized ITO substrates (○ and ●).

In Figure 7.4, we compare the WF trend vs. shell thickness for NSs-ITO structures with or without APTMS layer. The WF is, in both cases, dependent on the shell thickness: with the APTMS layer it decreases; instead, without it, the WF increases. Moreover, in the latter case, NSs-ITO structures present a lower WF. The WF exhibits a very slight dependence on shell thickness, also considering the error bar. However, a strong reproducibility was obtained on separate series of samples, using freshly made NSs.

To explain these results, some considerations about NSs surface potential should be done. Nanoshells, and colloidal particles in general, are stabilized electrostatically (see Chap. 3). Each colloid carries an electrical charge of the same sign which produces a force of mutual electrostatic repulsion between adjacent particles. For NSs this charge is negative and should contribute to modify the work function of ITO substrates.

In collaboration with the group of Prof. Baglioni, Dept. of Chemistry at the University of Firenze, measurements of the *zeta potential* of NSs with a different coverage thickness have been performed to establish a relation between the surface charge and the shell thickness. The zeta potential is the electrical potential at the junction between the Stern layer and the diffuse layer. If an electric field is applied, a charged particle will move with a velocity proportional to the applied field. The particle's mobility is related to the dielectric constant and viscosity of the suspending liquid and to the electrical potential at the boundary between the moving particle and the liquid. The magnitude of the surface potential (which is on the order of millivolts) is therefore related to the surface charge and the thickness of the double layer.

In Figure 7.5, zeta potential measurements for nanoshells with 95 ± 4 nm and shell ranging from silica core covered only by gold nanoparticles (0 nm) and 45 nm thick are reported. NSs present a negative potential of about – 50 mV, confirming that the surface charge is negative. For incomplete shell (particles with a shell thickness under 5 nm) the zeta potential becomes larger, in absolute value, and reaches – 60 mV. Whereas, for silica particle covered only by gold nanoparticles, the potential reduces (– 49 mV).

In the literature, the zeta potentials of silica nanoparticles were measured in the range of – 70 ÷ – 80 mV and APTMS-modified silica nanoparticles exhibited the zeta-potential of ca. + 40 mV because of the positive charge of the amino group.[24] The attachment of gold nuclei onto the silica nanoparticles was conducted by the electrostatic attractions between gold and APTMS-modified silica nanoparticles with different charges. The zeta potential of this system is – 43 mV.

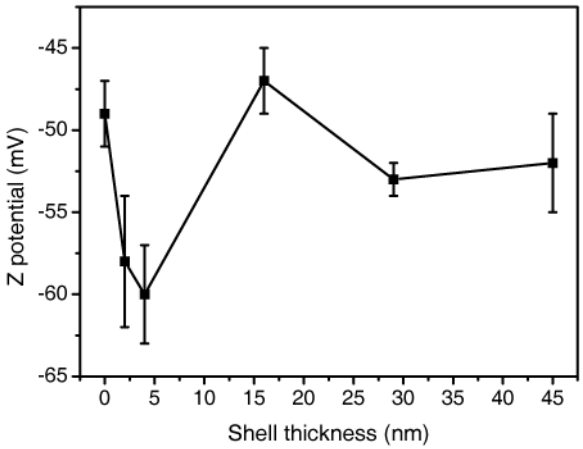

Figure 7.5: zeta potential measurements of NSs with 95 nm inner radius and different shell thickness.

Concluding, the zeta potential presents only a slight dependence on the shell thickness but it is quite interesting that nanoshells exhibit a negative charge on the surface and should allow one to explain the work function measurements.

First, let us consider the WF measurements on NSs deposited on APTMS functionalized ITO substrates. The amino group positive charges polarize the nanoshells and, in this way, NSs still present a dipole facing inwards the ITO surface (Figure 7.6a).

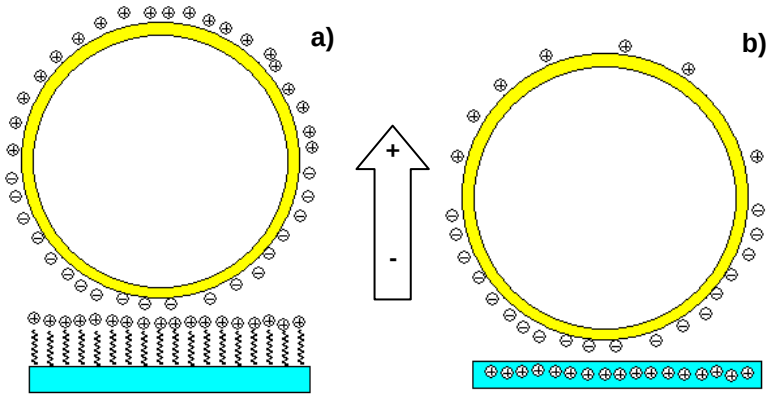

Figure 7.6: a) model to describe WF measurements on NSs deposited on APTMS functionalized ITO substrates. b) model to describe WF measurements on NSs deposited on clean ITO substrates.

This induces a further decrease of the WF, from 4.61 eV of APTMS functionalized ITO to ca. 4.3 eV. For clean ITO (without APTMS), negative charges near the NSs/ITO interface should induce mirror image charges in the ITO layer (Figure 7.6b). This results again in a dipole moment pointing inward in agreement with the experimentally found reduction of the work function and as reported in literature.[16]

To explain the work function trend with different NSs coverage of ITO slides, we still consider that the NSs are negatively charge. High level coverage are possible when the surface potential decreases so that repulsive forces are attenuated and NSs come closer. If the surface potential decrease, also negative charge decreases and so the dipole created on the ITO substrates is weaker. This induces a less pronounced reduction of the ITO work function.

This is only a small and poor effort to develop a model that explains these unexpected results. Further studies are needed to understand the observed behavior.

7.3. Scanning Kelvin Probe Microscopy

Scanning Kelvin probe microscopy is an additional working mode supported by some commercial AFM systems.[25] This mode measures the surface potential of the sample in addition to the sample topography.

7.3.1 Technique and fundamental relations of SKPM

SKPM involves scanning the surface in the AFM tapping mode to determine the topography on a line-by-line basis. After the recording of each line, the metal-coated or doped silicon cantilever is lifted at a fixed distance from the surface, and the tip is rescanned across the surface at this fixed height in "lift mode". In the lift mode, the tip to sample surface distance is set to values between 30nm and up to 3μm. On this rescan, the tapping piezo is turned off, and an AC voltage $U_{ac}\sin\omega t$ is applied to the tip, which stimulates oscillations of the cantilever. The tip and cantilever carry a charge, which is caused by the Fermi level adjustment between the tip and the sample, and which is connected to the Volta potential difference $\Delta\psi$ over the capacitor formed by them. The magnitude of the oscillations at the stimulating frequency ω, monitored by the AFM detection scheme, is made to vanish on a point-by-point basis during the lift mode rescan by adding to the tip a DC voltage U_{appl} that balances the Volta potential difference $\Delta\psi$, and thus the charge. Hence, unlike the standard SKP, in SKPM it is not the displacement current that is made to vanish but the first harmonic of the force exerted by an electric AC field on the charged cantilever/tip.

The electric energy stored in the capacitor formed by tip/cantilever and sample is:[17, 26]

$$W_{cap} = \frac{1}{2}V^2C \tag{7.9}$$

and the z- component of the electric force acting on the tip is

$$F_e = -\frac{dW_{cap}}{dz} = -\frac{1}{2}V^2\frac{dC}{dz} \tag{7.10}$$

with $V = \Delta\psi - V_{dc} + U_{ac}\sin\omega t$.

Considering $\sin^2 x = \frac{1}{2}(1 - \cos 2x)$, the total electric force is the sum of three components (7.11):

$$F_{e(\omega=0)} = -\frac{1}{2}\left[\left(V_{dc} - \Delta\psi^{KP}_{sample}\right)^2 + \frac{1}{2}U_{ac}^2\right]\frac{dC}{dz} \quad \text{constant component;}$$

$$F_{e(\omega)} = -\left(V_{dc} - \Delta\psi^{KP}_{sample}\right)U_{ac}\sin\omega t\frac{dC}{dz} \quad \text{component at frequency ω;}$$

$$F_{e(2\omega)} = \frac{1}{4}U_{ac}^2\cos 2\omega t\frac{dC}{dz} \quad \text{component at frequency 2ω;}$$

Hence, the force modulation at frequency ω becomes zero for $V_{dc} = \Delta\psi^{KP}_{sample}$. Thus, the vanishing of this force component by the applied DC potential directly yields the Volta potential difference.

In SKPM, the problem of contributions to the signal not arising from the tip area becomes very strong. Capacity contributions from the cantilever and sides of the tip to the overall capacity between tip and sample are relevant and the signal is expected to strongly depend on tip-sample distance. Usually the measured potential differences on a sample do not represent the real potential differences between tip and sample as the cantilever contribution is difficult to exclude. The passage of the cantilever over substrate areas far from the tip, with inhomogeneous topographic and compositional features, can significantly influence the Kelvin signal and result in incorrect results.

In addition to the stray capacitances, which yield wrong values of the measured work function, also faulty contrast, especially at steps, is observed. These topographical artifacts are due to the fact that the gradient of the tip contribution is especially small at such features, as the tip does not only "see" the flat surface but also the sides of the protrusions.

At the moment, with SKPM we can obtain a qualitative analysis of the difference in work function between area covered or not by nanoshells.

7.3.2 Experimental set up of SKPM

Atomic force microscopy (AFM) was performed with a NT-MDT (NT-MDT-Europe B.V., Nuenen, the Netherlands) instrument operating in air with a 3-μm scanner.

The operational scheme of the instrument is shown in Figure 7.7.

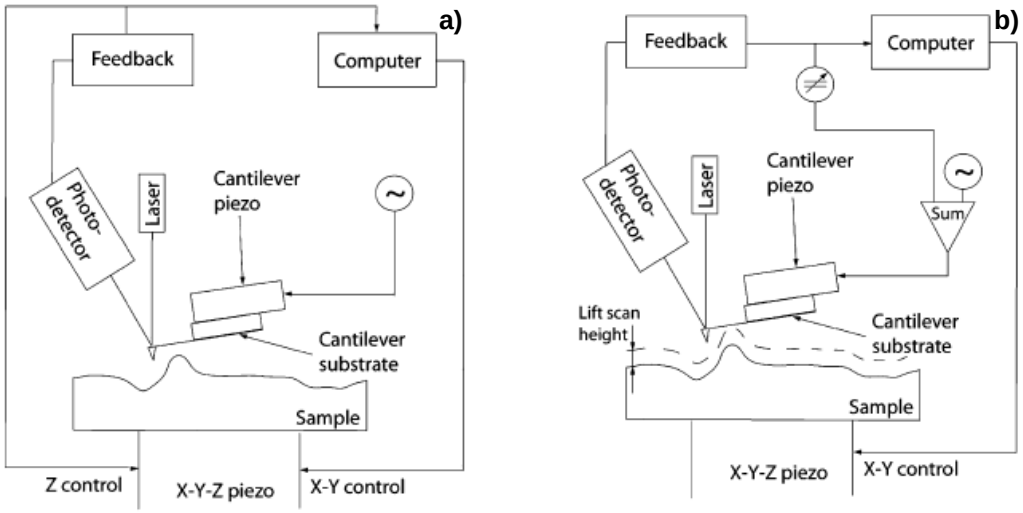

Figure 7.7: a) scheme of first pass of Kelvin probe technique measuring surface height, b) scheme of second pass of Kelvin probe technique measuring surface potential.[27]

Surface potential measurements are conducted using a two pass method. In the first pass, surface topography is measured using the standard AFM tapping mode. A schematic of this operation is shown in Figure 7.7a. In the second pass, the tip is scanned over the previously measured topography at 30 nm above the surface. A schematic of the second pass is shown in Figure 7.7b. In the second pass the piezo normally oscillating the tip in tapping mode is turned off. Instead an oscillating voltage is applied directly to the conducting tip which generates an oscillating electrostatic force.

To measure the surface potential, a DC voltage is applied to the tip until the component at frequency ω of the electric force (see eq. 7.11) vanishes. Thus, the surface potential at that point will equal the DC voltage applied to the tip to give zero oscillating force amplitude. In this study silicon tips coated with platinum/iridium (NSG03/Pt//50 NT-MDT) were used as a conductive tip. The probe has a typical curvature radius of 35 nm, a cantilever resonant frequency of 90 kHz, and a force constant of 1.74 N/m.

Samples were mounted in a special support and connected to ground.

7.3.3 SKPM measurements: some examples from the literature

SKPM is a recent technique and there are not many examples in the literature of its application to nanostructureted materials. Moreover, the difficulty in estimating work

function univocally because of the variety of parameters that affected Kelvin probe measurements makes this technique quite sensitive.

However, we would like to mention some works which we found interesting and promising for further developments. For example, Stiller et al[28] applied SKPM to investigate the optically induced *cis–trans* isomerization of self-assembled monolayers of azobenzene containing thiols. They created, using a microcontact printing technique, an array of circular dots of dodecanethiol with a diameter of ~10 mm on a gold surface. In the area not covered by dodecanethiol, 4-fluoro-methyl-4-(10-mercaptodecyl-oxy)azobenzene was assembled. These two materials have dipole moments that differ in their vertical component and have been detected with the SKPM. Moreover, illuminating the sample with light modulated the amplitude of the surface potential signal detected over the azobenzene-covered areas in such a way that it was possible to observe *in situ* the optical switching of these molecules with a spatial resolution in the micron range.

Also Bengtsson Blücher et al[29] used SKPM to study *in situ* the initial stages of atmospheric corrosion of an Al-Mg alloy. They investigated the evolution of the Volta potential during exposure to CO_2, the resolution being in the submicrometer range. The results showed that CO_2 strongly influences the atmospheric corrosion and allowed to develop a model to describe corrosion on AlMg alloys.

Barth and Henry Kelvin[30] were able to measure the difference in work function of Pd clusters deposited on MgO (001) surface. They measured with SKPM the voltage of the clean (001) surface of UHV cleaved MgO and of the same surface with supported palladium nanoclusters. Kelvin images of the clean surface show a bright contrast at steps, pits, and fragments of MgO due to negatively charged defects. Moreover, Kelvin images of supported Pd nanoclusters exhibit a mean voltage difference of 2.4 V between Pd clusters and the MgO(001) surface which is equal to the work function difference between MgO(001)/Mo and Pd.

These examples, except the latter in which also quantitative measurements are performed, suggest that SKPM should be used to obtain local information about surface potential. With this aim, we used SKPM to study the effect of nanoshells on the work function of ITO substrates at nanometer scale.

7.3.3.1 SKPM measurements on gold nanoshells

The system we are studying with SKPM is quite complex. It is composed of a clean ITO slides covered partially by nanoshells of different inner and outer radius. At the same time, NSs are covered by a thin polyvinylpyrrolidone (PVP) film, so some area of ITO substrate should be covered by PVP. Absolute quantitative values of work function were not reliable for this experiments because of the variety of parameters that affected Kelvin probe measurements but some qualitative remarks may still be done.

In Figure 7.8 SKPM measurements on NSs with a core radius of 95 nm and a shell thickness of 43 nm are shown. The sample presents also some gold nanoparticles of about 80 nm that form during the reduction of acid tetracloroauric.

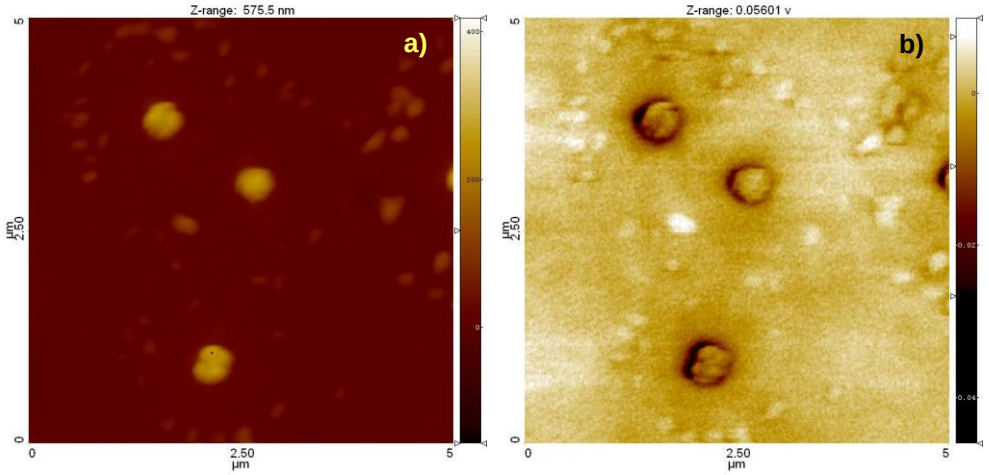

Figure 7.8: SKPM measurement of NSs (R_1 = 95 nm, R_2 = 138 nm) deposited on ITO glass: a) topography, b) Kelvin signal.

The topography image (Figure 7.8a) clearly shows three NSs and a lot of gold nanoparticles. In SKPM image, gold nanoparticles appear as bright spots on a darker but non homogeneous background. Instead NSs are darker, indicating a lower surface potential compared with nanoparticles. This confirms macroscopic WF measurements on gold nanoparticles and NSs. As reported in the literature, substrates covered by gold nanoparticles have the same WF as bulk gold[20], whereas ITO slides covered by NSs have a WF ranging between 3.9 and 4.4 eV. The background does not present a uniform potential and especially the area around nanoshells is usually less bright, indicating a lower surface potential. This is due to the presence of PVP which lowers the work function of ITO substrates and it is located near NSs.

In Figure 7.9, SKPM measurements on NSs with a core radius of 95 nm and a shell thickness of 14 nm are shown. Also in this case, the background presents some lighter area, which are ITO glass not covered by PVP and nanoshells appear darker.

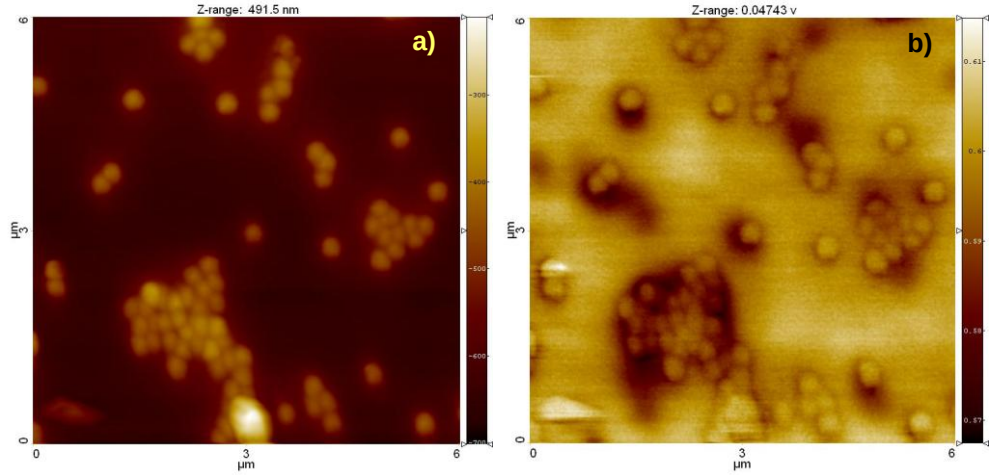

Figure 7.9: SKPM measurement of NSs (R_1 = 95 nm, R_2 = 109 nm) deposited on ITO glass: a) topography, b) Kelvin signal.

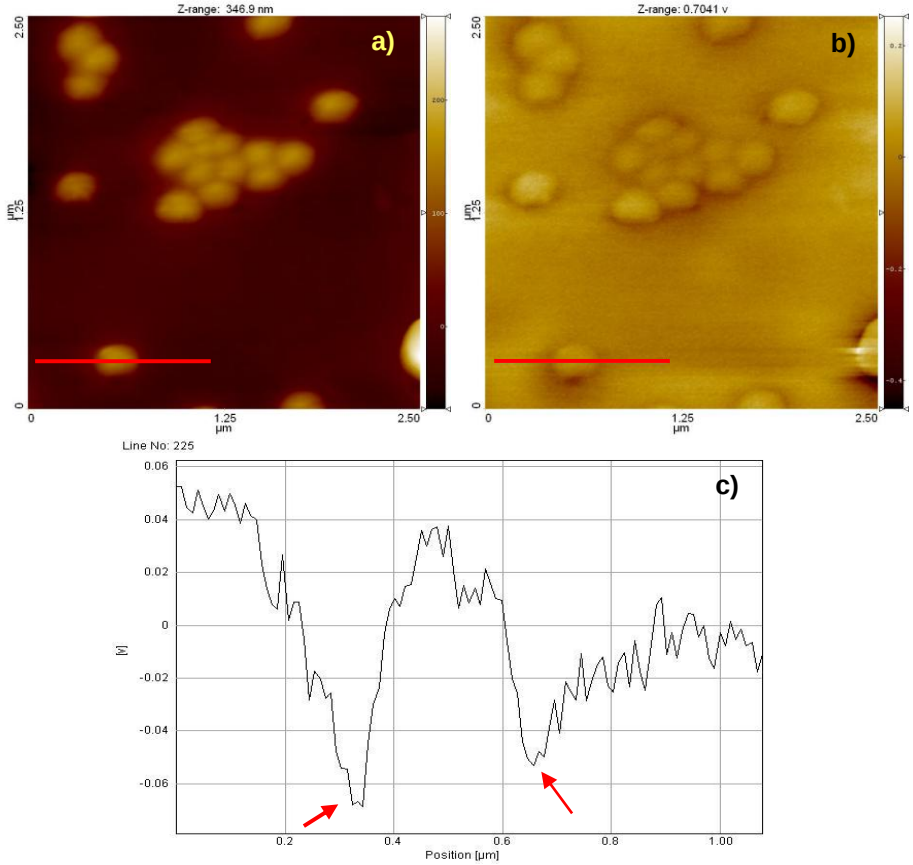

Figure 7.10: SKPM measurement of NSs (R_1 = 95 nm, R_2 = 109 nm) deposited on ITO glass: a) topography, b) Kelvin signal, c) profile taken at the red line in images a) and b).

In these images and in the following (Figure 7.10), some topographical artifacts are more evident. In fact nanoshells edges are darker, as if the potential in this zone was lower. In addition to the stray capacitances, which yield wrong values of the measured work function also faulty contrast especially at steps should contribute. These artifacts are due to the gradient of the tip contribution. The tip does not only "see" the flat surface but also the sides of the protrusions and creates some contrasts that are not due to difference in potential. If we consider the profile in Figure 7.10c, clearly a potential drop is visible at the base of the nanoshell (put in evidence by red arrows). The potential drop is due to a topography artifact, the sharp difference in Z between the substrate and the nanoshell. The scan direction goes from the left to the right and so the dip on the left of nanoshell is more pronounced than the one on the right.

Depending on the tip/cantilever used even an inversion of the potential contrast was observed. In Figure 7.11, SKPM measurements on NSs with a core radius of 158 nm and a shell thickness of 40 nm are shown. In this case, we can still observed some topography artifacts but NSs appear brighter than the substrate, indicating a higher potential than the ITO slide. This is in contrast with the KPM results, in which NSs provoke a decreasing in the WF of ITO glasses.

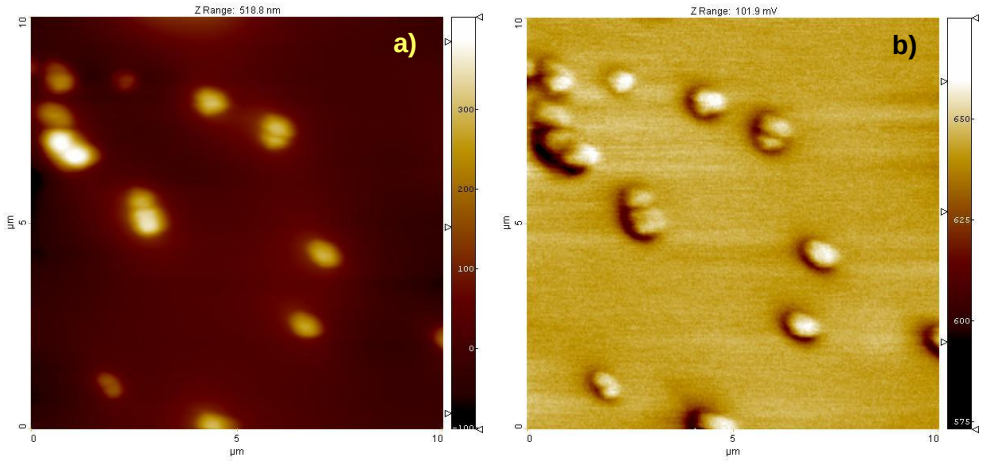

Figure 7.11: SKPM measurement of NSs (R_1 = 158 nm, R_2 = 198 nm) deposited on ITO glass: a) topography, b) Kelvin signal.

The effect is more pronounced in Figure 7.12, in which the scan size is reduced to 2 µm × 2 µm. The NS presents a surface potential higher than the background. The potential dips on the left and on the right of nanoshell are still presented.

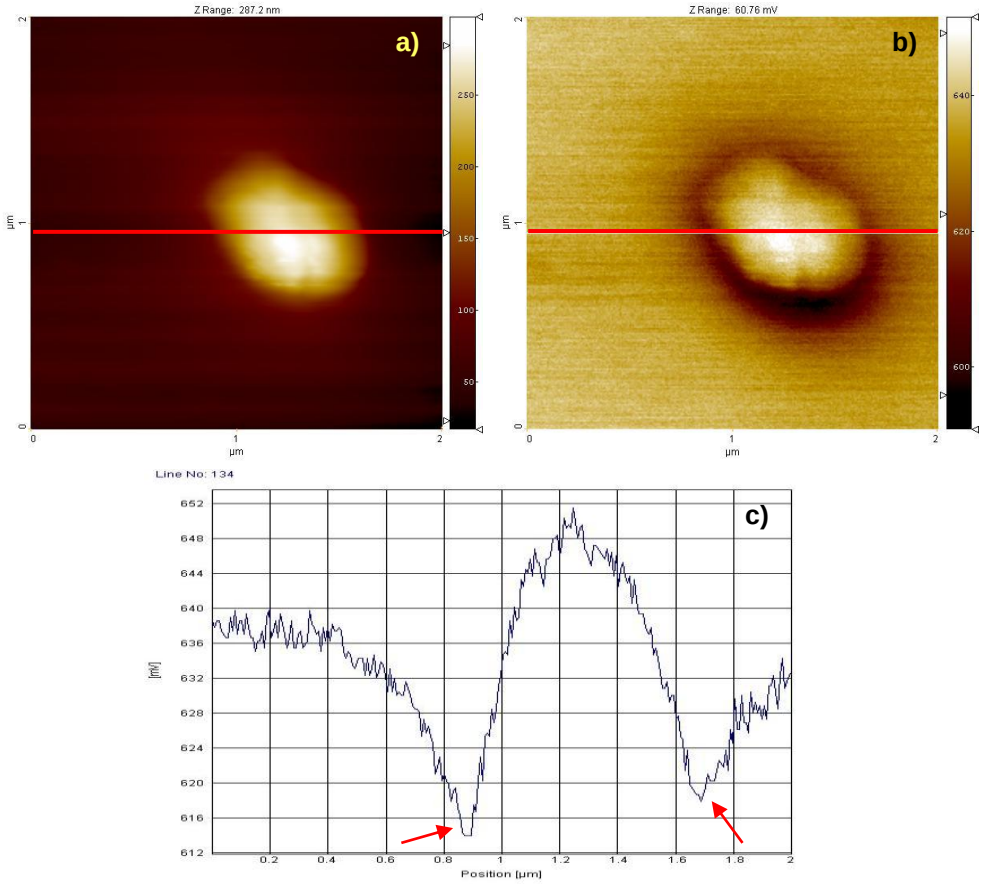

Figure 7.12: SKPM measurement of NSs (R_1 = 95 nm, R_2 = 109 nm) deposited on ITO glass: a) topography, b) Kelvin signal, c) profile taken at the red line in images a) and b).

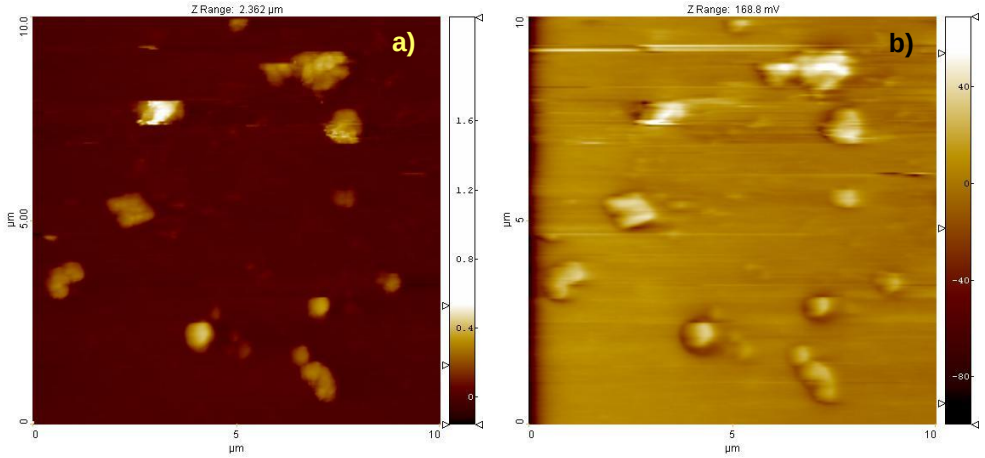

Figure 7.13: SKPM measurement of NSs (R_1 = 95 nm, R_2 = 138 nm) deposited on ITO glass: a) topography, b) Kelvin signal.

To simplify SKPM images analysis, some experiments on NSs not covered by PVP and deposited on ITO substrates are performed (Figure 7.13). The problem of NSs not covered

by PVP is that they move during the scan and so some defects are present on the images. As described previously, an inversion of the potential contrast was observed due to the tip/cantilever used. But in the absence of PVP, the background potential is more homogeneously distributed. So it is possible to confirm that the shadows in the surface potential images of ITO substrates are due to the reduction of WF caused by PVP deposited with NSs on ITO glasses.

References

(1) Stenzel, O.; Wilbrandt, S.; Stendal, A.; Beckers, U.; Voigtsberger, K.; Von Borczyskowski, C. *J. Phys. D: Appl. Phys.* **1995**, *28*, 2154-2162.

(2) Westphalen, M.; Kreibig, U.; Rostalski, J.; Lüth, H.; Meissner, D. *Sol. Energy Mater. Sol. Cells* **2000**, *61*, 97-105.

(3) Schaadt, D. M.; Feng, B.; Yu, E. T. *Appl. Phys. Lett.* **2005**, *86*, 063106.

(4) Derkacs, D.; Lim, S. H.; Matheu, P.; Mar, W.; Yu, E. T. *Appl. Phys. Lett.* **2006**, *89*, 093103.

(5) Cole, J. R.; Halas, N. J. *Appl. Phys. Lett.* **2006**, *89*, 153120.

(6) Sundararajan, S. P.; Grady, N. K.; Mirin, N.; Halas, N. J. *Nano Lett.* **2008**, *8*, 624-630.

(7) Brown, T. M.; Cacialli, F. *J. Polymer Science: Part B* **2003**, *41*, 2649-2664.

(8) Kim, J. S.; Cacialli, F.; Friend, R. H. *Thin Solid Films* **2003**, *445*, 358-366.

(9) Hopper, H.; Sariciftci, N. S. *J. Mater. Chem.* **2006**, *16*, 45-61.

(10) O'Regan, B.; Grätzel, M. *Nature* **1991**, *353*, 737-740.

(11) Kim, J. S.; Granström, M.; Friend, R. H.; Johansson, N.; Salaneck, W. R.; Daik, R.; Feast, W. J.; Cacialli, F. *J. Appl. Phys.* **1998**, *84*, 6859-6870.

(12) Koh, S. E.; McDonald, K. D.; Holt, D. H.; Dulcey, C. S.; Chaney, G. A.; Pehrsson, P. E. *Langmuir* **2006**, *22*, 6249-6255.

(13) Karsi, N.; Lang, P.; Chehimi, M.; Delamar, M.; Horowitz, G. *Langmuir* **2006**, *22*, 3118-3124.

(14) Morgado, J.; Barbagallo, N.; Charas, A.; Matos, M.; Alcacer, L.; Cacialli, F. *J. Phys. D: Appl. Phys.* **2003**, *36*, 434-438.

(15) Latini, G.; Wykes, M.; Schlapak, R.; Howorka, S.; Cacialli, F. *Appl. Phys. Lett.* **2007**, *92*, 013511-1-013511-3.

(16) Schlapak, R.; Armitage, D.; Saucedo-Zeni, N.; Latini, G.; Gruber, H. J.; Mesquida, P.; Samotskaya, Y.; Hohage, M.; Cacialli, F.; Howorka, S. *Langmuir* **2007**, *23*, 8916-8924.

(17) Rohwerder, M.; Turcu, F. *Electrochimica Acta* **2007**, *53*, 290-299.

(18) Hansen, W. N.; Hansen, G. J. *Surf. Sci.* **2001**, *481*, 172-184.

(19) Chung, Y. S.; Evans, K.; Glaunsinger, W. *Applied Surface Science* **1998**, *125*, 65-72.

(20) Carrara, M.; Kakkassery, J. J.; Abid, J.; Ferm$ìn, D. J. *ChemPhysChem* **2004**, *5*, 571-575.

(21) Schnippering, M.; Carrara, M.; Foelske, A.; Kotz, R.; Fermìn, D. J. *Phys. Chem. Chem. Phys.* **2007**, *9*, 725-730.

(22) Turkevich, J.; Stevenson, P. C.; Hillier, J. J. *Discuss. Faraday Soc.* **1951**, *11*, 55-75.

(23) Hansen, W. N.; Johnson, K. B. *Surf. Sci.* **1994**, *316*, 373-382.

(24) Park, S. E.; Park, M. Y.; Han, P. K.; Lee, S. W. *Bull. Korean Chem. Soc.* **2006**, *27*, 1341-1345.

(25) Rohwerder, M.; Hornung, E.; Stratmann, M. *Electrochimica Acta* **2003**, *48*, 1235-1243.

(26) Mironov, V. L. In *Fundamentals of Scanning Probe Microscopy;* Nizhniy Novgorod: 2004; .

(27) Lodge, R. A.; Bhushan, B. *Journal of Colloid and Interface Science* **2007**, *310*, 321-330.

(28) Stiller, B.; Karageorgiev, P.; Perez-Enciso, E.; Velez, M.; Vieira, S.; Reiche, J.; Knochenhauer, G.; Prescher, D.; Brehmer, L. *Surf. Interface Anal.* **2000**, *30*, 549-551.

(29) Bengtsson Blucher, D.; Svensson, J. E.; Johansson, L. G.; Rohwerder, M.; Stratmann, M. *ECS* **2004**, *151*, 621-626.

(30) Barth, C.; Henry, C. R. *J. Phys. Chem. C* **2009**, *113*, 247-253.

CHAPTER 8

Conclusions

The work presented in this thesis focuses on the investigation of the interaction between gold nanostructures and molecules.

Different shape nanoparticles synthesis have been described: spherical particles in water and in toluene, rod like particles in water and their transfer in organic solvents, gold nanoshells in water. The interest was mainly directed to the preparation of nanoparticles with a tunable plasmon band in the visible and near infrared regions, such as nanorods (NRs) and nanoshells (NSs), capable to enhance linear and non linear optical properties of molecules and polymers through the strong electromagnetic field developed on the particle surface, in resonance conditions. Although gold spherical nanoparticles (NPs) present a plasmon resonance which is not widely tunable, we decided to start with their synthesis in order to use them as a model for the functionalization.

We functionalized gold nanostructures with spiropyran, PEP-C3-SH and PEP-C12-SH, Rhodamine B.

NRs with an aspect ratio of 2.7 were synthesized in water and transferred in toluene, which causes NRs aggregation. NRs were characterized by two plasmon resonances, the transverse mode at 520 nm and the longitudinal one at 720 nm.

NRs in water were functionalized with PEP-C3-SH and PEP-C12-SH, whereas NR protected by dodecanethiol in toluene were functionalized with spiropyran. Especially with PEP-C3-SH, functionalization provoked some morphological changes and the loss of the rod-like shape due to etching of the surface of gold nanoparticles by thiol group, which is stronger for short chains. Also redox PEP moiety was responsible of the morphology changes as a result of surface charging effects. Morphological changes were not evident for NRs covered by spiropyran because this group is less redox active than PEP moiety.

Fluorescence decay times for PEP-C3-SH and PEP-C12-SH free and bound to NRs were measured to study the interaction between the dye and the nanostructure and to evaluate the effects of the chain length. As expected, the two dyes presented the same dynamics, with two characteristic times: a short one of 6.2 ± 0.5 ns and a long one of 61 ± 2 ns. When the dye is bound to NRs, the interaction between the molecules and the nanoparticles provoked a change in the PEP dynamics. Both PEP-C3 and PEP-C12 bound to NRs, decay faster, with τ = 4.0 ± 0.5 ns and τ = 5.2 ± 0.5 ns, indicating quenching of fluorescence. An aliphatic chain composed of 12 carbon atom (about 1.6 nm) is not long enough to prevent quenching of fluorescence.

NSs with a silica core R_1 of 50 ± 10 nm, 95 ± 15 nm and 158 ± 30 nm and a gold shell thickness varied between 10 and 50 nm were synthesized in water. This synthesis was quite complicated and allowed us to obtain nanoshells with a not complete shell, characterized by the presence of several apexes on the surface. The complex morphology is due to the mechanism of nucleation and growth of the shell and to the core size dispersion and influences the optical properties. In fact a broad plasmon peak with a long shoulder at longer wavelength characterized all the extinction spectra.

NSs were functionalized with PEP-C3, PEP-C12 and Rhodamine B. After anchoring of PEP moieties, NSs became instable. The same effect was not observed with Rhodamine B. To study the interaction between NSs and Rhodamine B, Pump and Probe measurements were performed. The dye clearly modified the dynamics of naked NSs and shortened the electron-phonon time decay from 4.9 ps (naked NSs) to 3.7 ps (RhB-NSs) introducing an additional channel by which hot electrons can decay.

SERS measurements of NSs, deposited on glass substrates, covered by benzenethiol were performed. Incomplete shells with sharp tips may turn out to be quite interesting for SERS analysis due to the strong local field developed that take place at tip apexes. In fact,

enhancement of the Raman signal was clearly observed because the concentration of benzenethiol is too low to give Raman signal except in case of strong enhancement field effects. We were not able to calculate the enhancement factor because we could not estimate precisely the amount of NSs under illumination nor the number of molecules for covered a single NSs but further measurements are planned to evaluate the enhancement factors.

Z-scan measurements, with fs laser pulses, were performed at 20 and 200 Hz and at different energy to study the nonlinear response of naked NRs and NSs. Both nanostructures behaved like saturable absorber and reshaped during laser pulse illumination. NRs reshaping process was more accentuated and the z-scan traces was strongly asymmetric. This phenomenon prevented the use of the Sheik-Bahae model to obtain the nonlinear absorption coefficient.

Instead, NSs z-scan traces are more symmetric, although the reshaping effect, and data, fitted with Sheik-Bahae model, yielded an effective value of the non linear absorption coefficient $\beta = (-1.1 \div -9.6)\times10^{-11}$ cmW^{-1} dependent on the pulse energy and repetition rate. The absolute value of the nonlinear absorption coefficient increased both with energy and pulse repetition rate. The effect of increasing the repetition rate is likely related to thermal effects, also confirmed by an increase of the beam waist radius used for fitting the z-scan data. The dependence on the energy, instead, indicated that the process is not a third order phenomenon, but higher order contributions should be taken into account.

Work function measurements on NSs deposited ITO substrates showed that by selectively choosing the shell thickness, ITO pre-functionalization and NP coverage, it is possible to fine-tune the WF of the transparent electrode within the range of 3.9 – 4.4 eV. Together with the plasmonic effects, the NSs deposition onto a transparent electrode potentially allows for improved efficiency both for light collection and charge collection.

RINGRAZIAMENTI…

Scrivere una tesi è sempre una sorta di bilancio su quello che si è fatto in un arco di tempo definito. Si riflette sul lavoro fatto, sui risultati ottenuti, forse non si è fatto abbastanza e si sarebbe potuto fare di più… ma alla fine di questo enorme lavoro (o almeno io lo ritengo tale) quello che di sicuro ho guadagnato è stata un'esperienza impagabile e la possibilità di collaborare con persone brillanti e con un "valore umano" ancora maggiore.

Vorrei ringraziare, in primis, il mio supervisore Renato Bozio per aver incoraggiato ogni mia idea e sostenuto il mio ruolo di rappresentante dei dottorandi (nonostante sapesse che mi avrebbe tolto del tempo alla ricerca), per tutta la libertà che mi ha dato e soprattutto per avermi sopportato in questi ultimi mesi in cui sono sicura di essere stata pressante e invasiva (in poche parole un incubo)!

Un ringraziamento speciale va anche al mio supervisore londinese, Franco Cacialli, che mi ha accolta nel suo laboratorio a braccia aperte. Non posso dimenticare Gustaf, Francesco, Penglei, Sergio, Yong, Martin, Michele e Olly…i vari caffè e muffin e il fish and chips del venerdì…CHEERS!

Ringrazio la Prof.ssa Angela Agostiano e il Prof. Baglioni per avermi ospitato rispettivamente all'Università di Bari e di Firenze e in particolare Roberto e Tiziana per le divertenti ed estenuanti giornate baresi e Debora, Francesca e Costanza per il breve flash fiorentino… mi hanno dimostrato come i rapporti umani possano andare ben oltre la "banale" collaborazione scientifica!

Un grazie speciale anche a Luca (e con lui al Dott. Mancin) per avermi permesso di usare il DLS e per le lunghe chiacchierate su quanto possa essere deprimente la vita del dottorando…
Non posso poi dimenticare i ricercatori di NanoFab e in particolare Piero e Francesco che hanno reso tragicomiche le mie giornate all'AFM, tornerò presto a rallegrarvi (o tormentarvi…dipende dai punti di vista…).

Un pensiero speciale va poi a tutto il gruppo di ricerca.
A Camilla e Raffaella per l'incoraggiamento quando mi sono sentita sola, triste e arrabbiata!
A Simone e Gabriele senza il quale non saprei proprio cosa fare!
Ad Ilaria e Eleonora perché più che colleghe sono amiche!
A Samuele, Elisabetta (a cui ho promesso un Science…), Tode, Nicola…per il giovedì kebab, le cene etniche, la cheese cake, la birra, lo spritz, il cibo, il caffè, le torte, le brioche…che ci aiutano ad affrontare ogni giorno le gioie e i dolori della ricerca.
Tutti voi rendete questo lavoro un piacere, sono fortunata!

Grazie anche a chi mi ha "distratto" dalla ricerca…l'ADI, Enrico, Saverio (e Angela), Enzo, Dario, Mario, Mauro ma soprattutto Gianni…insieme abbiamo fatto cose che non pensavo si potessero fare, se il dottorato e il post-doc a Padova sono migliori è anche un po' merito nostro!

Per finire ringrazio chi dice, più o meno scherzando, che dovrei andare a lavorare…
Mamma e papà che mi hanno accompagnato a prendere una marea di aerei in questi ultimi anni e mi hanno sempre appoggiato in tutto…
Vale…che continua a prendersi cura di me…e speriamo recuperi qualcosa per me dal campionario, in bocca al lupo per la tua nuova avventura!
A zia Sonia, zio Guido e Matteo, che iniziano a chiedersi quando metterò la testa a posto…e a Riccardo che si chiede cosa voglia dire "cugino di secondo grado"!
A Barbara e Rani…perché restiamo paperelle…ma allarghiamo la famiglia!
A Luana, che c'è sempre!
Ai miei amici che dicono che mi si vede sempre troppo poco in giro…
A Omar…che è da poco tempo parte della mia vita, ma è sicuramente quella più importante!